Christoph Szasz

Air Gap Insulated Exhaust Manifold

Simulation Methodology & Design Criterions

Diploma thesis
submitted for the degree of
Diplom-Ingenieur

AVL List GmbH

submitted to the Faculty of
Mechanical Engineering and Economic Sciences
at the Graz University of Technology

Ao.Univ.-Prof. Dipl.-Ing. Dr.techn. Raimund Almbauer
Institute of Internal Combustion Engines & Thermodynamics
Graz University of Technology

March 2011

Christoph Szasz

Luftspaltisolierter Abgaskrümmer

Berechnungsmethodik & Auslegungskriterien

Diplomarbeit
zur Erlangung des akademischen Grades
Diplom-Ingenieur

AVL List GmbH

eingereicht an der Technischen Universität Graz
Fakultät für Maschinenbau und Wirtschaftswissenschaften

Ao.Univ.-Prof. Dipl.-Ing. Dr.techn. Raimund Almbauer
Institut für Verbrennungskraftmaschinen u. Thermodynamik
der Technischen Universität Graz

Graz, im März 2011

Abstract

The present thesis presents a numerical simulation methodology for air gap insulated exhaust manifolds. These have, compared to cast iron manifolds which are most commonly used in the automobile industry, a major passive contribution to the reduction of air pollutants.

Based on analytical investigations on heat transfer due to conduction, convection and radiation three different three dimensional, steady state finite element heat transfer models are developed and presented, that fulfill the specific requirements of describing the energy transfer through the air gap. In the following these models are compared in respect to physical correctness, accuracy and cost issues, such as analysis time and required computational resources. From this follows the decision for the usage of a heat transfer model that represents the energy transfer due to radiation in a simplified way. With this approach analysis time can be reduced significantly in comparison to a model that works with an exact radiation law. At the same time it is shown that the selected approach delivers sufficient accuracy and that these analysis results defer only marginally from an exact solution.

To determine time dependent effects of heat transfer a transient heat transfer analysis is performed the results of which serve as thermal load input for the strength analysis that is also part of the methodology development process.

Within a strength analysis the global deformation behavior and specific characteristics of air gap insulated exhaust manifolds are presented. Thereby the better part of the simulation methodology is based on AVL List GmbH’s standard methodology for cast iron exhaust manifolds, hence only small amendments are made. The usability of the existing methodology is presented by the exemplary evaluation of highly loaded areas.

Furthermore a methodology for modeling weld joints with finite elements is introduced, as their usage in dual-walled exhaust manifolds is inevitable due to the way of assembling.

In the final chapter of the present thesis design criterions for air gap insulated exhaust manifolds are developed and summarized. They should ease the process of first constructional layout in subsequent customer projects.

Kurzfassung

Die vorgelegte Arbeit beschäftigt sich mit der Entwicklung einer numerischen Simulationsmethodik für luftspaltisolierte Abgaskrümmer. Diese weisen gegenüber Gusskrümmern, welche in der Automobilindustrie am häufigsten eingesetzt werden, entscheidende Vorteile auf – insbesondere was den passiven Beitrag zur Reduktion von umweltschädlichen Abgasen betrifft.

Ausgehend von analytischen Überlegungen zur Wärmeübertragung durch Wärmeleitung, Konvektion und Strahlung werden drei dreidimensionale, stationäre Finite Elemente Wärmeübertragungsmodelle erarbeitet, welche die besonderen Anforderungen an die Abbildung der Energieübertragung im Luftspalt erfüllen und diese korrekt abbilden. Außerdem werden sie in Bezug auf physikalische Richtigkeit, Exaktheit und Kostenaspekte, wie Rechenzeit und benötigte Computer Hardware-Ressourcen verglichen. Aus dem Vergleich folgt die Entscheidung zur Verwendung eines Wärmeübertragungsmodells, welches den Energietransfer durch Strahlung in einer vereinfachten Form berücksichtigt und dadurch deutlich kürzere Analysezeiten ermöglicht als ein vergleichbares Modell, welches mit einem exakten Strahlungsgesetz arbeitet. Gleichzeitig wird gezeigt, dass das ausgewählte Modell in Bezug auf Rechenergebnisse lediglich marginal vom exakten Pendant abweicht.

In weiterer Folge wird, um die zeitabhängigen Effekte der Wärmeübertragung darzustellen, eine transiente, zeitabhängige Wärmeübertragungsberechnung durchgeführt. Diese dient im weiteren Verlauf der Methodenentwicklung als thermische Belastungsgröße in der anschließenden Festigkeitsberechnung.

Im Rahmen der Festigkeitsanalyse werden das globale Deformationsverhalten und spezifische Eigenschaften von luftspaltisolierten Abgaskrümmern aufgezeigt. Hierbei wird auf die für Gusskrümmer bestehende Simulationsmethodik der AVL List GmbH zurückgegriffen, und es werden lediglich Ergänzungen vorgenommen. Exemplarische Auswertungen von hoch belasteten Zonen untermauern die Verwendbarkeit der vorhandenen Methodik.

Weiters wird ein Verfahren zur Finiten Elemente Modellierung von Schweißnähten, deren Verwendung bei luftspaltisolierten Abgaskrümmern unumgänglich ist, gemacht.

Im abschließenden Kapitel dieser Arbeit werden Auslegungskriterien für luftspaltisolierte Abgaskrümmer erarbeitet und zusammengefasst, welche die Basisauslegung in zukünftigen Kundenprojekten erleichtern sollen.

Acknowledgement

The present work was carried out at the Department of Simulation and Mechanical development at AVL List GmbH (AVL).

I am deeply indebted to my supervisor DI (FH) Mario Brunner for giving me the opportunity not only to do my diploma thesis in his skill team but for the priceless opportunity to gain working experience during the years of my academic studies. His support and guidance significantly contributed to this thesis.

My gratitude also belongs to Ao.Univ.-Prof. Dipl.-Ing. Dr.techn. Raimund Almbauer for accepting the supervision. His advice and perspective are very much appreciated. I also thank him for the countless discussions and his experienced, invaluable advice.

I would also express my thanks to all my colleagues at AVL. Their support, guidance and patience had large influence on the present work.

Finally I want to express my gratitude to my parents for their unlimited support and for enabling me an academic education.

Contents

Table of figures

List of tables

List of abbreviations

ASS	assembly
AVL	Anstalt für Verbrennungskraftmaschinen List GmbH
BC	boundary condition
CAD	computer aided design
CFD	computational fluid dynamics
CO	carbon monoxide
CPU	central processing unit
DAC	computational fluid dynamics skill team at AVL List GmbH
FE	finite element
FEA	finite element analysis
FEM	finite element method
FI	fully implicit
FTP	federal test procedure
FVM	finite volume method
HC	hydro carbon
HT	heat transfer
HTC	heat transfer coefficient
I4	four cylinders in-line
I6	six cylinders in-line
LC	load case
NEDC	new European driving cycle
NO_x	nitrogen oxide
NVH	noise, vibration, harshness
PEEQ	equivalent plastic strain
SN	surface normal
ST	strength
THC	total hydro carbon

V6…12	six…twelve cylinders in V configuration
1D	one dimensional
3D	three dimensional

Symbols

A	area, m^2
C	gap radiation constant; reflection matrix
c_p	specific heat at constant pressure, $J/kg \cdot K$
D	diameter, m
d	gap-clearance, m
E	emissive power, W/m^2; Young’s modulus
F	view factor
G	irradiation, W/m^2
Gr	Grashof number
g	gravitational acceleration, m/s^2
h	convection heat transfer coefficient, $W/m^2 \cdot K$
k	thermal conductivity, $W/m \cdot K$
L	characteristic length, m
N	number of surfaces in an enclosure
Nu	Nusselt number
Pr	Prandtl number
Q	heat transfer rate, W
q	heat transfer rate, W
q'	heat transfer rate per unit length, W/m
q''	heat flux, W/m^2
r	radius, m
R	cylinder radius, m; distance between two points, m
Ra	Rayleigh number

Re	Reynolds number
T	temperature, K
u	mass average fluid velocity component, m/s
x, y, z	rectangular coordinates, m

Greek Letters

α	absorptivity; thermal diffusivity, m^2/s; linear thermal expansion coefficient, $1/K$
β	volumetric thermal expansion coefficient, $1/K$
δ	hydrodynamic boundary layer thickness, m; gap size, m; Kronecker delta
ε	emissivity; strain
$\dot{\varepsilon}$	rate of equivalent plastic strain
θ	zenith angle, rad; temperature, K
μ	viscosity, $kg/s \cdot m$
ν	kinematic viscosity, m^2/s
ρ	mass density, kg/m^3
σ	Stefan-Boltzmann constant; stress, N/m^2

Subscripts

A, B	species in a binary mixture
a	ambient
abs	absorbed
amb	ambient
AVG	average

b	blackbody
c	cross-sectional
$conv$	convective
eff	effective
g	gas
i	general species designation inner
ip	inner pipe
ist	current temperature
L	based on characteristic length
$\max$	maximum temperature
o	outer
op	outer pipe
rad	radiation
s	surface condition
$total$	total
x	local conditions on a surface
δ	local conditions in boundary layer local conditions in air gap
∞	free stream condition
0	initial condition

Superscripts

pl	plastic
$*$	dimensionless quantity

Overbar

$\bar{}$	surface average condition

1 Introduction and theory

As an introduction a general overview of exhaust manifold design concepts is presented which is subsequently followed by a summary of designs for air gap insulated exhaust manifolds commonly used nowadays. The illustration of AVL's present finite element simulation methodology for cast iron exhaust manifolds and the presentation of an analytic approach for air gap insulated exhaust manifold analysis proposed by Kyu-Hyun et al. [2000] complete this chapter. Closing the motivation for the present work is explained.

1.1 Introduction to exhaust manifolds

An exhaust manifold is the part of the engine that collects exhaust gases from multiple cylinder head ports into a single pipe.

For a long period inexpensive and easy to manufacture casted exhaust manifolds were used in the automotive industry. Headers – also known as extractors – made of stainless steel or ceramics were only used in racing application because of the demand for torque and power optimized engine design.

The passing of the first European emission bills in the 1980s forced the automotive industry to integrate a catalytic converter into every new car. Over the years as the legislation became stricter new technologies had to be developed to meet the requirements of these regulations. It turned out that a key factor in the effective reduction of emissions is to reach the light-off temperature of the catalytic converter as fast as possible after the cold start of the engine to guarantee an effective conversion of exhaust gases [van Basshuysen and Schäfer (ed) 2005, p. 301].

Due to the fact that cast iron exhaust manifolds have a high thermal capacity that absorbs large amounts of heat from the exhaust gas flow during the engine warming-up phase new exhaust manifold concepts have been developed to avoid cooling of catalytic converter inlet gas temperatures.

Based on van Basshuysen and Schäfer (ed) [2005, pp. 304] the different exhaust manifold concepts, that can be commonly found in the market, can be summed up as follows:

- Cast iron exhaust manifolds
- Single walled tubular exhaust manifolds – also known as extractors or headers

- Single walled half-shell exhaust manifolds
- Air gap insulated exhaust manifolds
- Hybrid types (combination of cast iron and tubular sheet metal)

The most common design concepts are presented in the following chapters. Thereby only those concepts are considered which disregard any exhaust after treatment systems or turbochargers.

The following descriptions are based on [van Basshuysen and Schäfer (ed) 2005, pp. 301], [Nording 1991], [Santanam et al. 1998], [Jean 2006] and [Nording et al. 2009].

1.1.1 Cast iron exhaust manifold

Exhaust manifolds made of cast iron usually have a wall thickness of $7-8\ mm$ when made of grey cast iron and $2.25-4\ mm$ when chill casted. The most common materials used are grey cast iron and grey cast iron with silicon and molybdenum added.

The biggest advantage of a cast iron manifold is its design potential, hence a very compact design can be achieved. Also it has a good acoustic performance because of the high damping ability of the material.

On the other hand cast iron manifolds have several disadvantages and that is why often alternative design concepts are used. The biggest one is the high thermal capacity of cast iron manifolds due to their high wall thickness. The material absorbs large amounts of heat from the exhaust gas and therefore extracts thermal energy from the catalytic converter that makes it impossible to reach the light-off temperature short after the cold engine start.

Another weakness of cast iron is its thermal stability. Exhaust gas temperatures increased significantly since the early ‘80s where they were around $850\ °C$ in Otto and $650\ °C$ in Diesel engines. Due to the increase of engine power and stoichiometric combustion exhaust gas temperatures are around $1000\ °C$ in Otto and $850\ °C$ in Diesel engines nowadays. Because of the low heat capacity of cast iron plastic material deformation occurs at these temperatures and leads to the formation of micro cracks and further to malfunction of the manifold.

Another effect that needs to be mentioned is the so called engine soaking. Soaking in this context means how the temperature of the manifold behaves after the engine has been stopped. Cast iron manifolds tend to have high temperatures for a long period of time because of the high thermal capacity of the construction.

The necessity for heat shielding is generally determined by surface temperatures, soaking and neighboring components. Because the heat energy transferred through radiation increases with the 4th power of the emitting surfaces temperature heat shields are recommended for exhaust manifold surfaces where temperatures can reach $800\ °C$.

Ever since there is an effort to minimize the vehicles overall weight. Cast iron manifolds are massy parts and therefore have a high potential for weight reduction.

1.1.2 Single walled tubular exhaust manifold

Singe walled tubular exhaust manifolds are made of thin walled $(0.8-1.8\ mm)$ austenitic or ferritic steel tubes connected to one another by welds.

The biggest advantage of this thin walled, light weight design is its low thermal capacity, hence because of the low mass little thermal energy from the exhaust gas is absorbed and the catalyst receives more enthalpy and therefore reaches its light off temperature soon after cold start of the engine.

Due to its design tubular exhaust manifolds made of steel are considered to be fatigue endurable even under high temperature loading.

Disadvantages of a single walled design are high surface temperatures that require heat shielding, a critical acoustic behavior due to the materials low damping ability and higher manufacturing costs than cast iron manifolds.

1.1.3 Single walled half-shell exhaust manifold

This design concept is similar to the tubular one explained before hence its pros and contras. The only difference is that non tubular parts are used as well. Usually the manifold consists of several thin walled, either hydro formed or drawn parts that are joined with welds.

1.1.4 Air gap insulated exhaust manifold

The air gap insulated exhaust manifold is a dual walled concept. It consists of an inner and an outer thin walled steel pipe that are arranged concentrically. For being able to fit the pipes together they have to be built of several parts usually half shells joined with welds. The inner pipe is in contact with exhaust gas and has no carrying function, hence very thin steel can be used. The outer pipe has two functions.

1. Carrying the manifolds self weight and the weight of all adjacent parts such as the catalytic converter and turbo charger.
2. Sealing the manifold towards the ambience.

Between the two pipes there is an air gap that acts as insulator and on one hand keeps the exhaust gas from energy losses and on the other hand avoids the heat transfer to the outer pipe. Therefore it lowers surface temperatures significantly thus no additional heat shielding is required.

Due to the higher thermal loading of the inner pipe a mechanism has to be provided to absorb thermal deformations that occur because of the diverse thermal expansion of the cylinder head and the exhaust manifold. To avoid thermal stresses usually a sliding contact mechanism is applied that enables relative movement between the individual parts of the inner gas guiding pipe. Similar mechanisms can also be used for the outer pipe to prevent it from getting in contact with the inner pipe.

Another possibility for the reduction of thermal deformations is the usage of ferritic steel instead of austenitic. Because of the lower thermal expansion coefficient of ferritic steal which is $10\times10^{-6}\,1/K$ at $100\,°C$ and $10.5\times10^{-6}\,1/K$ at $400\,°C$ compared to austenitic steel where the thermal expansion is $16\times10^{-6}\,1/K$ at $100\,°C$ and $17.5\times10^{-6}\,1/K$ at $400\,°C$ [AVL Material Database 2010] deformations and therefore thermal stresses can be reduced significantly as presented in Figure 1.

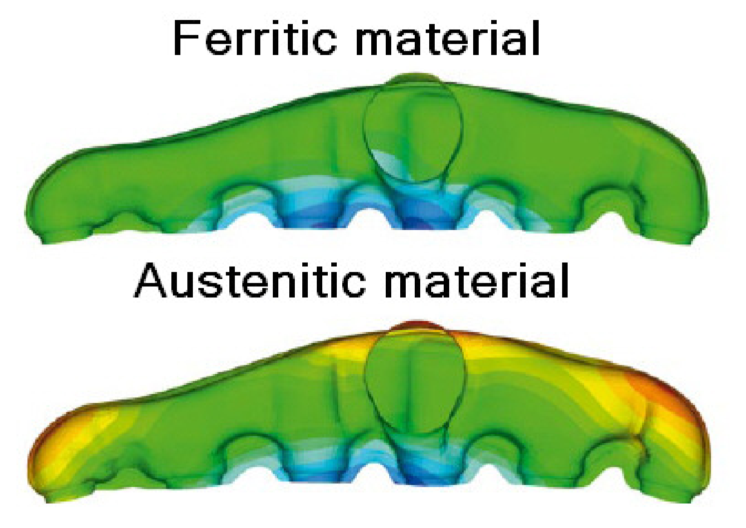

Figure 1: Deformation of the outer shell of an air gap insulated exhaust manifold [Nording et al. 2009]

Because of the thin walled design a low thermal capacity can be achieved. A reduction of 75 % is possible compared to a cast iron manifold and 30 – 40 % compared to a single walled tubular design [Nording 1991]. This results in higher exhaust gas temperatures as can be seen in Figure 2.

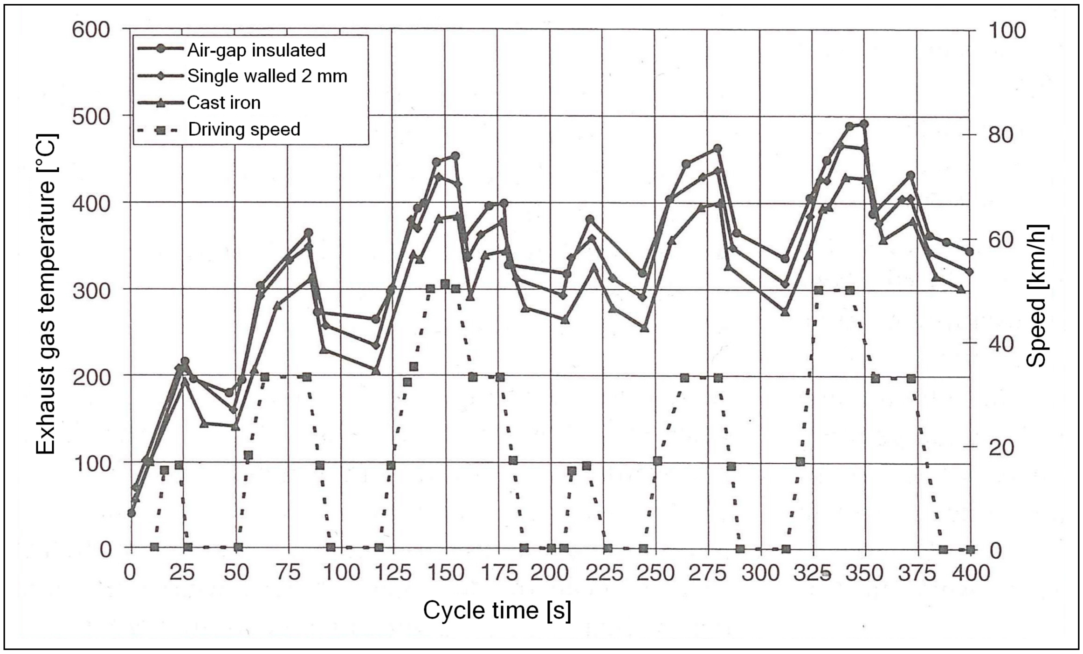

Figure 2: Influence of manifold design on exhaust gas temperature before catalytic converter [van Basshuysen and Schäfer (ed) 2005, p. 301]

The effect of higher exhaust gas temperatures is an earlier light-off of the catalytic converter. The converter light-off is defined as the temperature measured in the center of the converter brick, one inch from the front face of the brick, that corresponds to 50 % converter efficiency (for HC) [Santanam et al. 1998]. This contributes significantly to the reduction of pollutant emissions such as hydrocarbons (HC), carbon monoxide (CO) and nitrogen oxides (NO_x). Figure 3, Figure 4 and Figure 5 impressively show the reductions that can be achieved during the FTP-75 test cycle by using air gap insulation. It can be seen that the overall emissions of air pollutants significantly decrease immediately after the cold start if a dual-walled exhaust pipe is used as the catalytic converter reaches its light-off temperature earlier in comparison to the single pipe. According to Kyu-Hyun et al. [2000] within 100 seconds after the cold engine start total hydrocarbons (THC) can be reduced by 42 %, NO_x by 37.5 % and CO by 48 % by using a dual-walled system instead of a single walled.

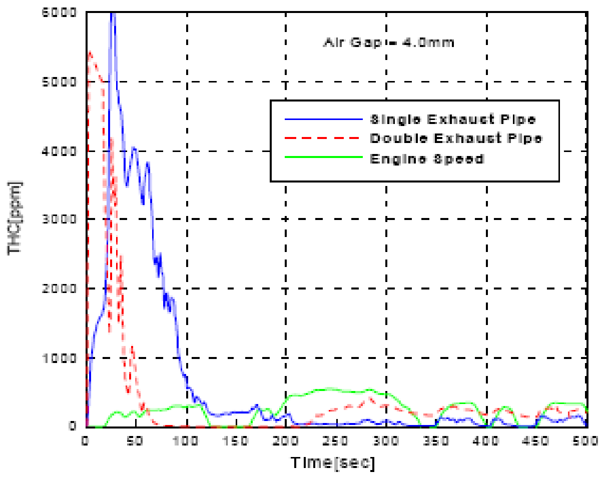

Figure 3: Comparison of THC emissions between single and dual-wall exhaust system [Kyu-Hyun et al. 2000]

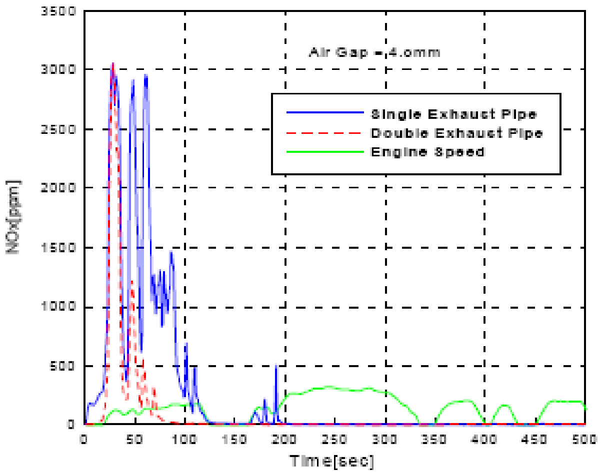

Figure 4: Comparison of NO_x emissions between single and dual-wall exhaust system [Kyu-Hyun et al. 2000]

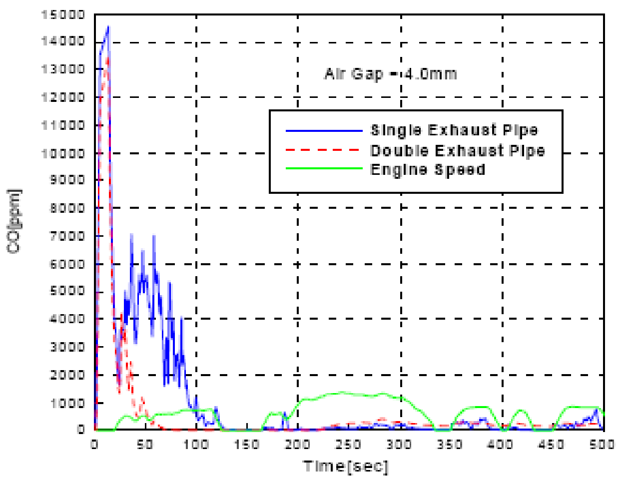

Figure 5: Comparison of CO emissions between single and dual-wall exhaust system [Kyu-Hyun et al. 2000]

With the fortified application of synthetic materials increasing underhood temperatures due to increasing engine power and therefore higher exhaust gas flow are more and more a concern especially in the development of engines with large displacements as V8 and V12 engines. The heat energy transferred through radiation increases with the 4th power of the emitting surfaces temperature. Figure 6 shows that the emitted energy at $800\ °C$, that is typical for cast iron manifolds is approximately seven times higher than the emitted energy at $400\ °C$ that can be reached with the usage of air gap insulation [Nording 1991].

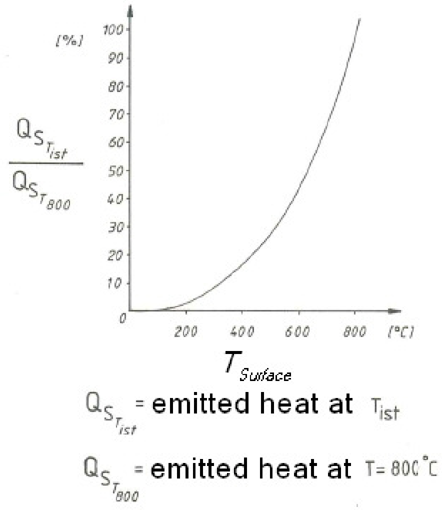

Figure 6: Radiation energy ratio vs. wall temperature with $800\ °C$ as reference temperature [Nording 1991]

An overview of skin temperatures during the NEDC cycle for different manifold concepts is presented in Figure 7.

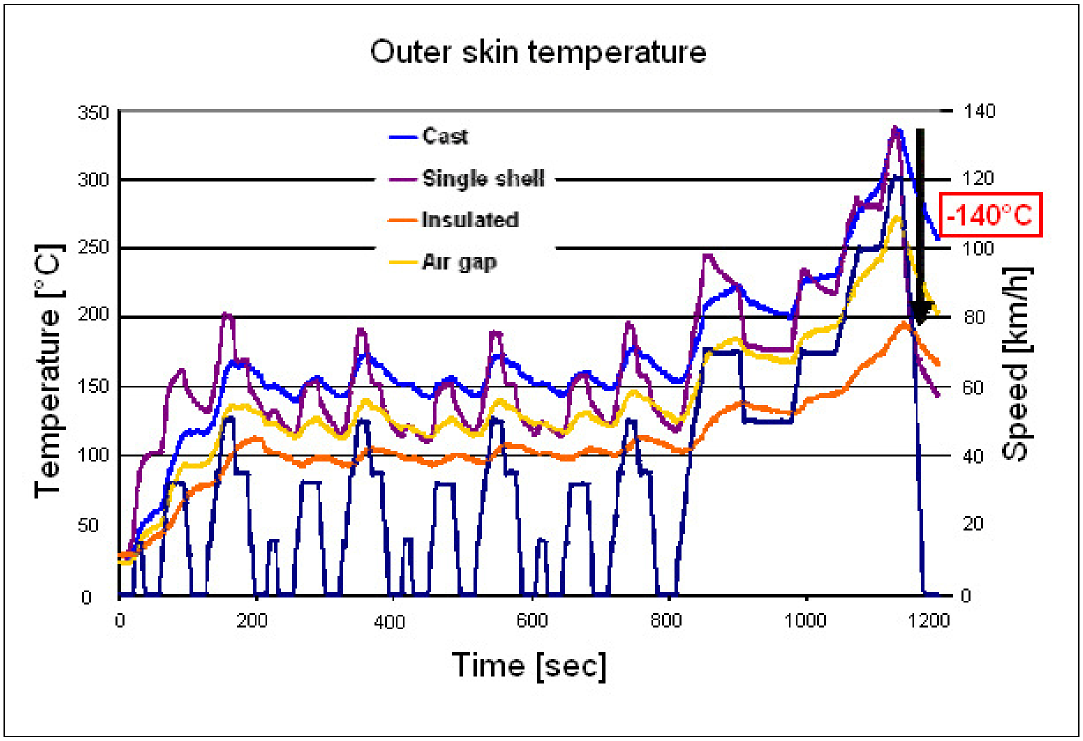

Figure 7: Manifold skin temperature for different manifold concepts during the NEDC cycle [Jean 2006]

At the end of the test cycle a difference of $140\ °C$ can be observed between an insulated manifold and the cast iron reference. Under full load condition the difference can be even higher up to $200\ °C$. Since the air gap insulation is not as effective as any solid insulant the skin temperature of the air gap insulated manifold is higher than the insulated ones. Nevertheless a temperature difference of $70\ °C$ can be observed in comparison to the cast iron manifold [Jean 2006].

1.1.5 Concept comparison

To give a better overview of the strengths and weaknesses of the different exhaust manifold concepts a rating matrix (Table 1) was developed. Thereby the manifold design concepts discussed in chapters 1.1.1 to 1.1.4 were compared and rated in matters of manufacturing costs, assembly weight, acoustic performance and thermal characteristics. The comparison is based on [van Basshuysen and Schäfer (ed) 2005, pp. 301].

Table 1: Rating matrix of exhaust manifold concepts

	Cast iron	Single walled	Single walled half-shell	Air gap insulated
Weight	--	++	++	+
Acoustic performance	++	--	--	○
Costs	++	○	+	--
Radiation towards environment	-	--	--	++
Thermal capacity	--	-	-	++

1.2 Scope of present air gap insulated exhaust manifold concepts

A fair amount of different air gap insulated exhaust manifold designs can be found on the market. Besides the materials and the manufacturing process used they usually differ in

1. the mechanism used for the compensation of thermal deformation and stresses
2. the air gap design
3. additional insulation arrangements within the air gap
4. the mechanism to prevent the inner pipe from getting in contact with the outer pipe and therefore from creating local temperature hot-spots
5. materials used for the exhaust manifold (hybrid types)

Based on patent research the most common concepts will be presented and discussed at this point.

1.2.1 Concepts for compensation of thermal deformation and stresses

The most common design concept used for the compensation of thermal stresses that occur because of different elongations of the cylinder head and exhaust manifold due to a high temperature difference between the two parts is to use a plurality of exhaust gas guides plugged into one another with a sliding fit. Among others such mechanisms are described in DE 19628797 C1 [1996] and DE 10346552 A1 [2005] (Figure 8).

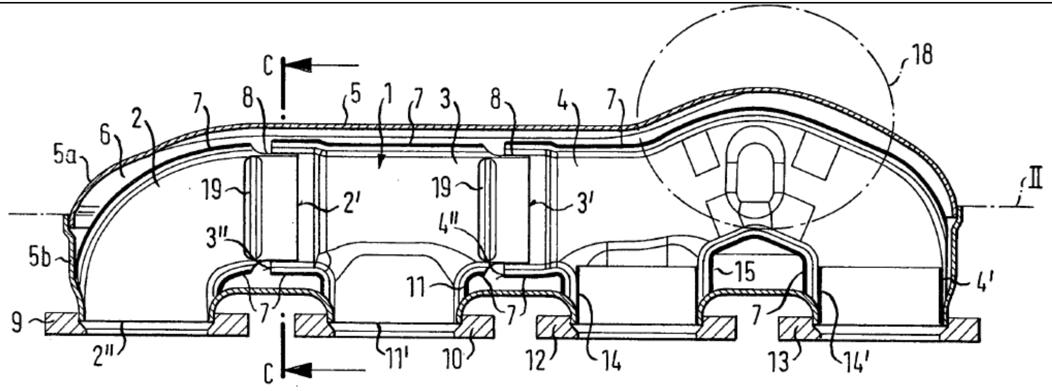

Figure 8: Air gap insulated exhaust manifold with sliding fit [DE 10346552 A1 2005]

DE 10102637 A1 [2002] (Figure 9) describes an additional design feature to minimize thermal deformation and therefore to avoid failures due to crack formation for I4 and I6 engines. The problem is solved through the connection of the two inlet flanges of the two middle cylinders by a web. The web is formed of a material having higher thermal expansion than the material constituting the remaining components of the exhaust manifold and a passage bore between the flanges so that the web can be heated by hot exhaust gases.

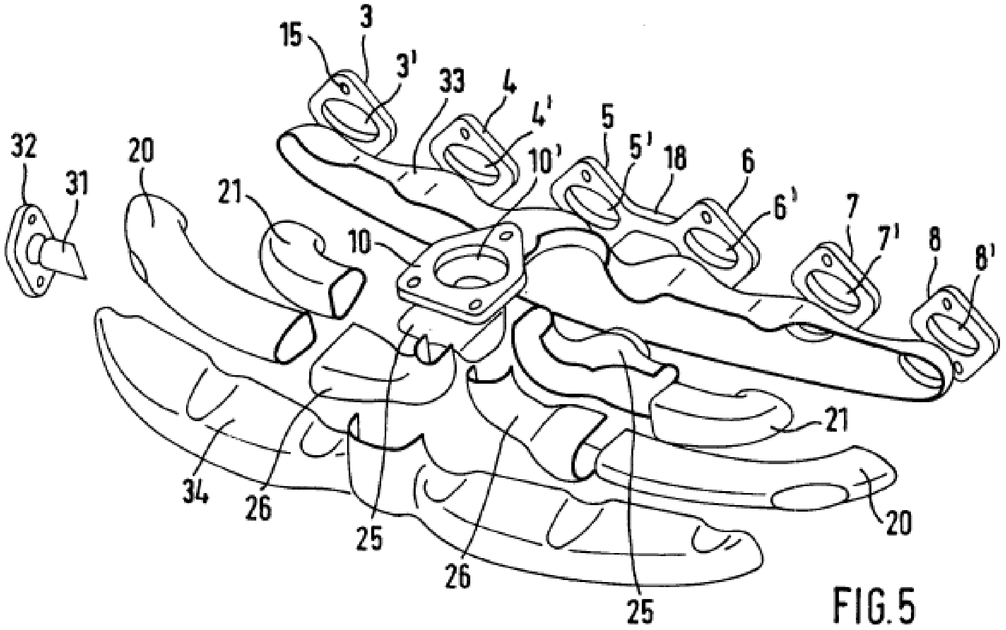

FIG.5

Figure 9: Air gap insulated exhaust manifold with connected inlet flanges [DE 10102637 A1 2002]

Another design concept is described in DE 102004021196 A1 [2005] (Figure 10) where the inner pipe is mounted on the outer pipe only in the area of highest thermal expansion which is located centrally between the outlet and inlet openings of the manifold the latter of which is at the greatest distance from the outlet opening. To ensure the relative movement between inner and outer pipes a sliding fit is also provided in the area of at least one inlet opening.

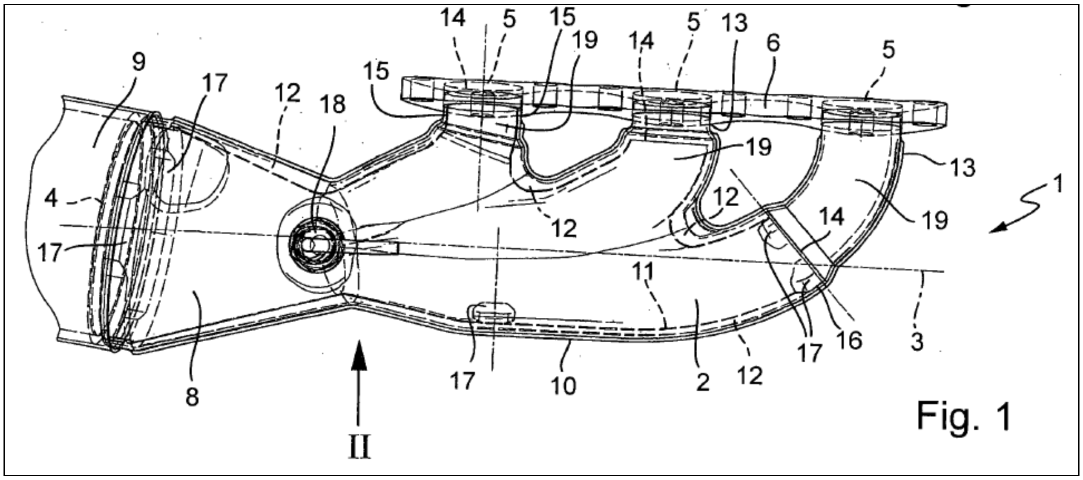

Figure 10: Air gap insulated exhaust manifold with centrally arranged connection between the inner and the outer pipe [DE 102004021196 A1 2005]

1.2.2 Possibilities for designing the air gap

Usually, two air gap design concepts can be found within the industry. Most common in use are fully insulated manifolds. This means that the inner gas guiding pipes are surrounded completely by an insulating air gap and therefore by an outer pipe. Among others US 5,768,890 [1998] (Figure 11) and DE 19952648 A1 [2000] describe such concepts.

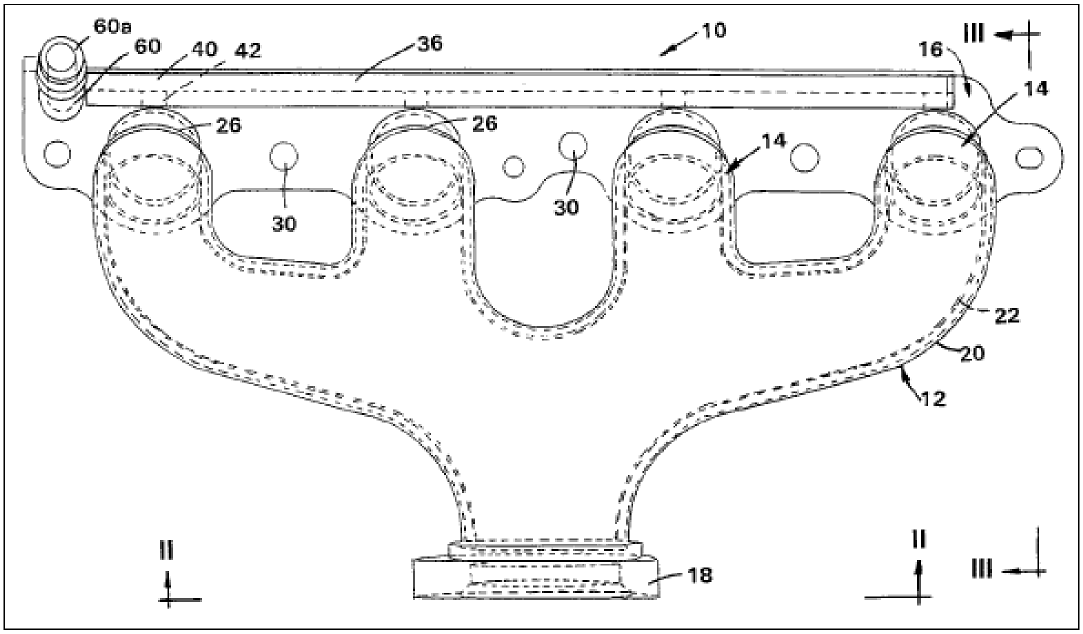

Figure 11: Entirely air gap insulated exhaust manifold [US 5,768,890 1998]

The second concept for air gap design is to only provide air gap insulation in certain areas where the thermal loading of the manifold is especially high. The zones typically affected by the highest thermal load are the spots located opposite the lateral inlet openings and the collector pipe of the exhaust manifold. Therefore US 6,247,552 B1 [2001] (Figure 12) describes an exhaust manifold where a double walled air gap insulated design is provided only in the area of the collector pipe whilst all other pipes are single walled half-shell pipes. This design results in the saving of considerable amounts of material.

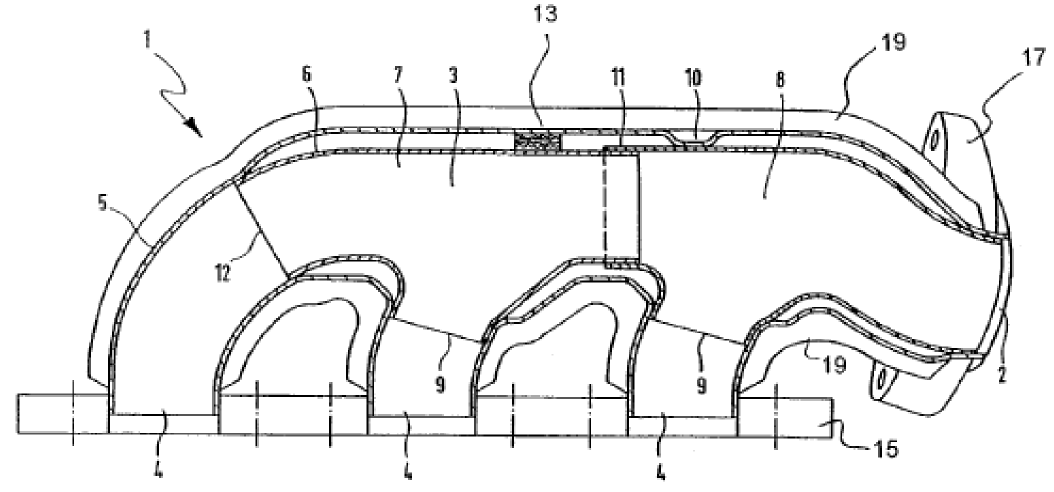

Figure 12: Partly air gap insulated exhaust manifold [US 6,247,552 B1 2001]

1.2.3 Concepts with additional insulation arrangements within the air gap

The parts of the inner gas guiding tubes are usually not designed to be gas tight because of the sliding fits that have to be installed to ensure relative movement between the parts. The outer surface of the collecting pipe can be impinged by hot unavoidable leakage flow that leads to local temperature hot-spots in punctual areas. To prevent the outer pipe from being hit directly by any leakage flow US 2009/0139220 A1 [2009] (Figure 13) describes the usage of at least one intermediate plate being installed in the air gap. Even a very thin design with a plate thickness of $0.15-0.3\ mm$ is sufficient to avoid hot spots and to additionally reduce the surface temperature of the manifolds outer pipe and therefore the energy is being transferred to neighboring engine components by radiation.

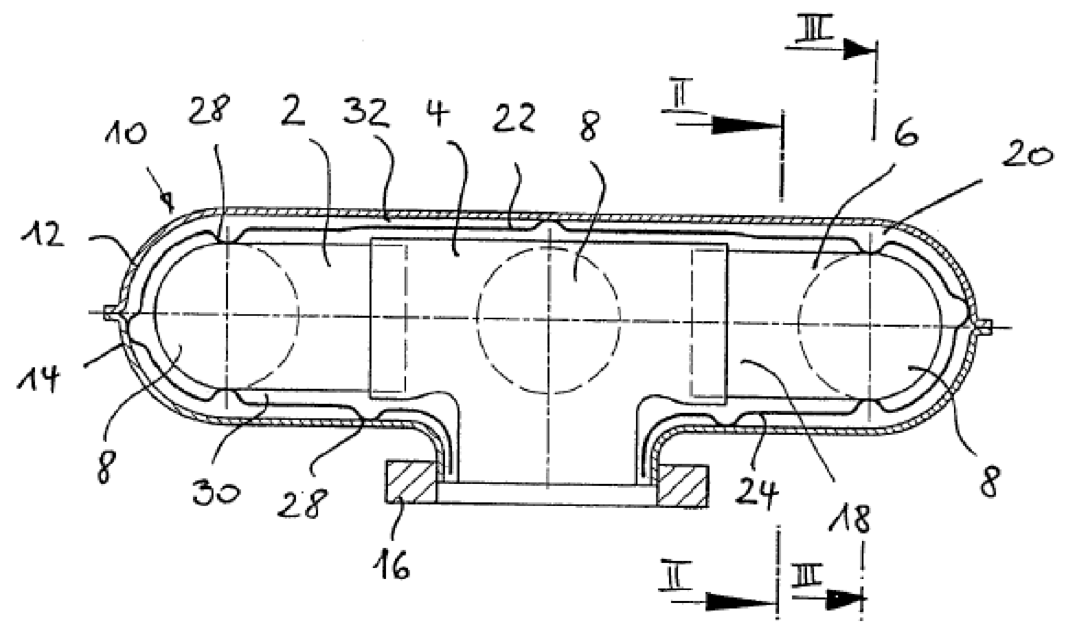

Figure 13: Air gap insulated exhaust manifold with intermediate plate [US 2009/0139220 A1 2009]

1.2.4 Mechanisms to avoid thermal bridges between inner and outer pipes

Exhaust manifolds are exposed to high gas temperatures and permanent heating-up and cooling-down cycles. Over the years of operation such a loading can change original clearances significantly. Usually this leads to undesirable vibration and acoustic performance. DE 102008019999 A1 [2009] describes an exhaust manifold design with an additional insulting pipe within the air gap that guarantees the exact positioning of the inner gas guiding pipes towards the outer carrying pipes over the lifetime of the manifold. The following three designs are described:

1. A rigid connection through spacers between all the pipes (Figure 14).
2. A press fit connection with wire frames between the additional insulting pipe and the outer pipe.
3. A design where the middle pipe is manufactured of several small pipes that are connected to the inner gas guiding pipe over wireframes.

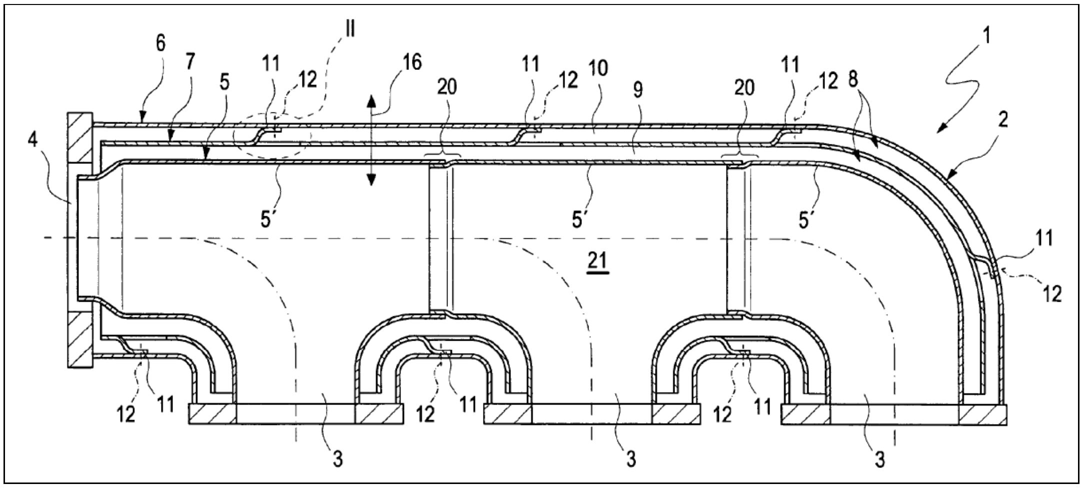

Figure 14: Air gap insulated exhaust manifold with rigid connection between all pipes [DE 102008019999 A1 2009]

Besides avoiding the hot inner pipe from getting in contact with the outer pipe these design proposals significantly contribute to the overall stiffness of the exhaust manifolds structure and therefore drastically increases its acoustic performance.

1.2.5 Hybrid type exhaust manifold

Usually dual-walled air gap insulated exhaust manifolds are made of either austenitic or ferritic sheet metal. As previously discussed the material used determines the manifolds thermal properties such as heat capacity and thermal expansion.

Because the carrying capacity of sheet metal exhaust manifolds is lower than the ones made of cast iron sometimes hybrid type manifolds are used. DE 202006015883 U1 [2008] (Figure 15) describes an exhaust manifold where the middle of the exhaust manifold is made of cast iron and the outer collecting pipes are made of sheet metal tubes with air gap insulation. While the cast iron part in the middle provides high carrying abilities that are sometimes required for close coupled catalytic converters and turbo chargers the sheet metal pipes provide sufficient flexibility for the compensation of thermal deformations.

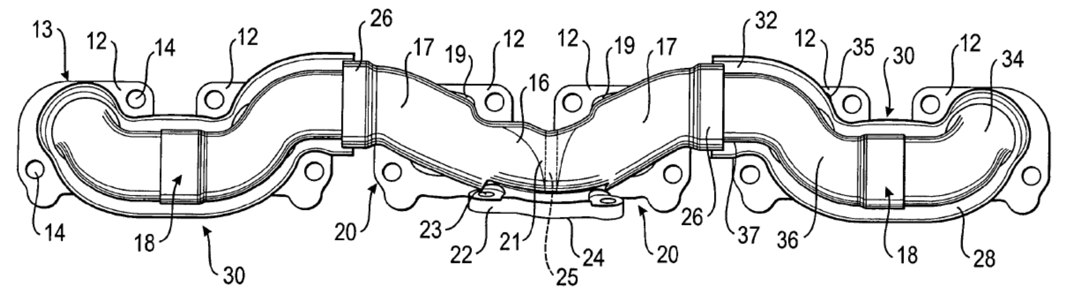

Figure 15: Hybrid type exhaust manifold [DE 202006015883 U1 2008]

1.3 Outline of present simulation methodology

In the late 1960s numerical methods such as the finite element method (FEM) and the finite volume method (FVM) were developed for the simulation of complex structural and fluid mechanical problems. Thereby partial differential equations are solved in order to find an approximate solution of a discrete problem. Nowadays the FEM and FVM are integral parts of many engineering disciplines.

The standard methodology used today for the simulation of exhaust manifolds is also based upon these numerical methods. The simulation process is a complex chain of events and usually contains different tasks starting with a one dimensional (1D) engine process simulation where the global heat balance and the gas exchange cycle are represented. The output of this first task is a temporal resolution of all relevant physical values such as gas flow rates, cylinder pressures and gas temperatures. As these values are only time dependent and not dependent on a certain position within the manifold, hence in 1D simulation reduced geometry is used, a three dimensional (3D) computational fluid dynamics (CFD) analysis has to be performed [Petutschnig et al. 2002]. Among others fluid temperatures and flow velocities for every discrete surface can be obtained as a result. From these the heat transfer coefficients can be mapped that serve besides gas temperatures as input for the 3D finite element analysis (FEA). Because of the unsteady gas flow and temperature characteristics that dominate in exhaust manifolds a transient heat transfer (HT) analysis has to be performed to identify time-dependent effects. The last step of the simulation procedure is the strength (ST) analysis where the temperature field obtained in the HT analysis serves as input. Besides that bolt connections, pressure distribution and gasket behavior are considered for the analysis. Furthermore a fatigue analysis can be performed with these results. These techniques are not going to be further discussed.

1.4 Scope of present work

Kyu-Hyun et al. [2000] describe the development of dual-wall air gap exhaust systems with a special focus on heat transfer analysis. A computer program for wall temperature prediction based on analytic dissolving of heat transfer equations is introduced. Thereby the heat flow is assumed as two dimensional. Furthermore the validation of the computational model with test bed measurements is presented.

For modeling the exhaust system a three zone model (Figure 16) was chosen as representative where the zones are connected in series.

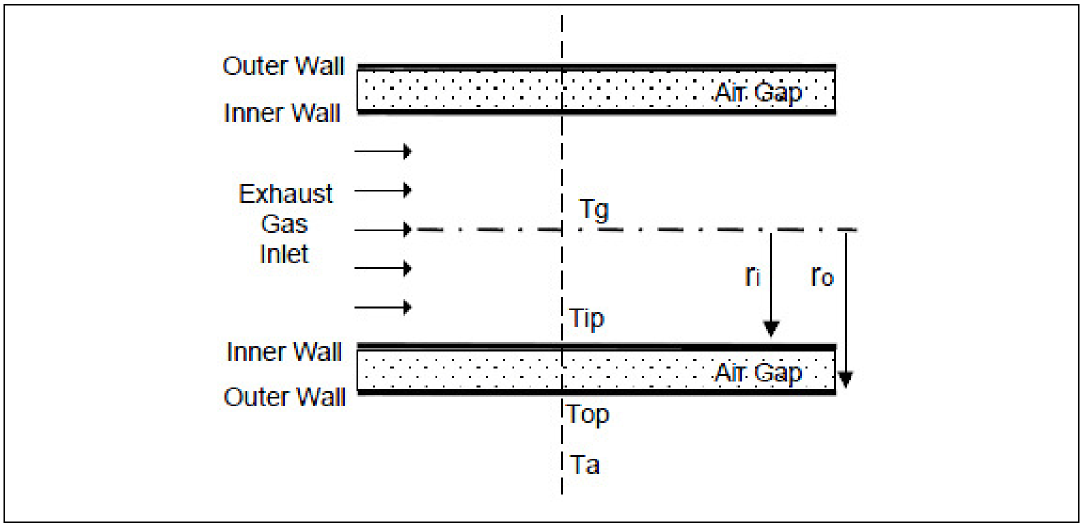

Figure 16: Analytical model of gas flow in exhaust system [Kyu-Hyun et al. 2000]

The first zone represents the heat transfer initiated by forced convection between the exhaust gas and the inner pipe wall. The second zone incorporates the heat conduction through the air gap. The third zone is a combination of the mechanisms of free convection and radiation heat transfer towards the ambient.

The equations used for the analysis model are well known and can be found in [VDI-Wärmeatlas 2002] and [Rohsenow and Hartnett 1973].

As previously mentioned this computer program delivers only an analytic solution that is not acceptable for the accurate prediction of wall temperatures. To obtain a result that is as accurate as possible a numeric approach needs to be chosen. The development of a numeric approach will be presented and discussed in the following chapters.

1.5 Motivation

Nowadays as described before a well developed simulation methodology exists for numerical heat transfer and strength analysis. At AVL this methodology is most commonly used for cast iron exhaust manifolds. With the increase of specific engine power and therefore exhaust gas temperatures and the tightening of legislation concerning air pollution air gap insulated manifolds are more and more appreciated throughout the industry because of their capability to enable a faster light-off of the catalytic converter.

As previously discussed air gap insulation has a strong effect on the temperature distribution of the exhaust manifold – also known as temperature field – that again among other effects determines the components deformation and stress distribution. AVL's present simulation methodology described in Chapter 1.3 does not cover the heat transfer effects in the insulating air gap, thus it can not be used for this type of manifolds. As the aim of numerical simulation is a reliable lifetime prediction such a determinant effect can not be neglected.

The purpose of this diploma thesis is to develop a simulation methodology for air gap insulated dual-walled exhaust manifolds which features a heat transfer analysis technique that represents the heat transfer process through the air gap and can be implemented into the overall finite element simulation process used currently. Thereby AVL's strength analysis simulation process for cast iron manifolds is considered as reference and will be adapted to the usage with dual-walled manifolds. Furthermore design criterions should be defined to ease the time and efforts of the first constructional layout in future customer projects.

2 Fundamentals of heat transfer

From the discipline of thermodynamics it is well known that energy can be transferred through the interaction of a system with its surroundings. However thermodynamics only describes the end state of the energy transport process and provides no information about the transfer mechanism and the time characteristics of the energy exchange.

In the following chapter the fundamentals of heat transfer will be explained based on [Incropera and DeWitt 2002], [Baehr and Stephan 2008] and [Holman 2010].

2.1 What is heat transfer?

Heat transfer (or heat) is thermal energy in transit due to a temperature difference.

Transportation of heat occurs whenever a temperature difference exists between two positions. These can be either within the same medium or belong to different mediums. Thus heat transfer is the transport of energy due to a temperature gradient. Three types of heat transfer can be differentiated:

1. Conduction
2. Convection
3. Radiation

2.1.1 Conduction heat transfer

Conduction is the transport of energy between neighboring molecules due to an existing temperature gradient. This sort of energy transport occurs in both solid and fluid mediums and is mainly dependent on material properties. The heat transfer process can be quantified by the equation

$$q''_x = -k\frac{dT}{dx} \tag{2.1}$$

that is also known as Fourier's law where q''_x $[W/m^2]$ is the heat flux – the heat transfer rate in the direction of the heat flow per unit area. The proportionality constant k is called thermal conductivity $[W/m \cdot K]$ and is a characteristic of the medium. The minus sign is inserted to satisfy the second principle of thermodynamics that says that heat is transferred in the direction of decreasing temperature. If we assume steady-state conditions as shown in Figure 17 and a constant thermal conductivity the temperature distribution is linear and the heat flux is then

$$q_x'' = k\frac{T_1 - T_2}{L} = k\frac{\Delta T}{L} \tag{2.2}$$

For obtaining the heat transfer rate by conduction, q_x $[W]$, equation (2.2) has to be multiplied with the area A $[m^2]$ of the plane wall.

$$q_x = q_x'' \cdot A \tag{2.3}$$

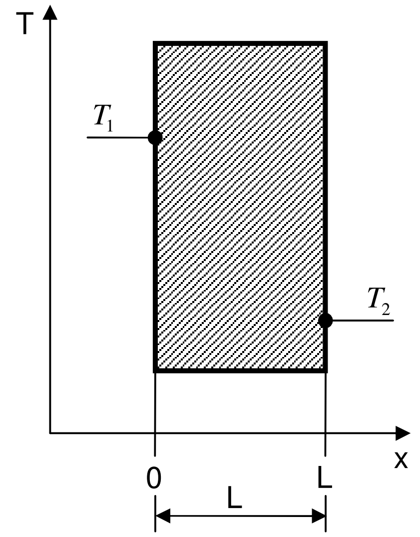

Figure 17: Steady-state heat transfer through a plane wall

2.1.1.1 Thermal conductivity

As mentioned before thermal conductivity is a material characteristic that indicates the materials ability to conduct heat.

The mechanism responsible for thermal conduction in gases is the movement of molecules. The higher the energy level of a molecule – the energy level corresponds with the mediums temperature – the higher its velocity is. When a molecule moves from a high-temperature region to a region of lower temperature it transports kinetic energy to the lower-temperature part of the system and gives up this energy through collisions with lower-energy molecules. As the velocity of a molecule depends on the temperature of the medium it can be said that heat transfer at high temperatures is better than at low temperatures. Figure 18 illustrates the temperature dependence of the thermal conductivity of selected gases at normal pressure. It can be observed that thermal conductivity increases with temperature for all materials.

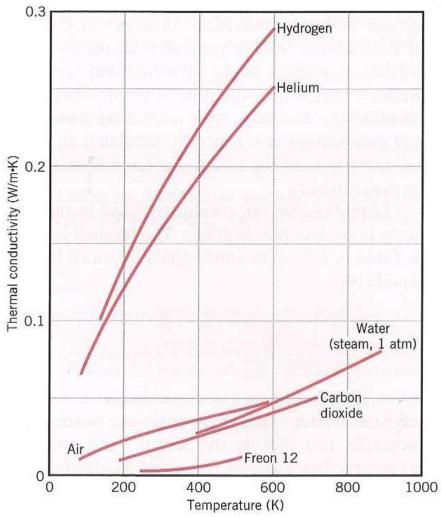

Figure 18: The temperature dependence of the thermal conductivity of selected gases at normal pressure [Incropera and DeWitt 2002, p. 57]

As solids usually comprise of free electrons and periodically arranged atom bounds called the lattice the transport of thermal energy is due to two effects:

1. Lattice vibrations and
2. transport by free electrons.

Good thermal conductors usually have large amounts of free electrons while the thermal conduction in metallic materials usually happens due to lattice vibration. Like the thermal conductivity of gases the one of solids is also temperature dependent. Figure 19 shows the temperature dependence of the thermal conductivity of selected solids. In contrast to gases no clear relations between conductivity and temperature can be observed for solids.

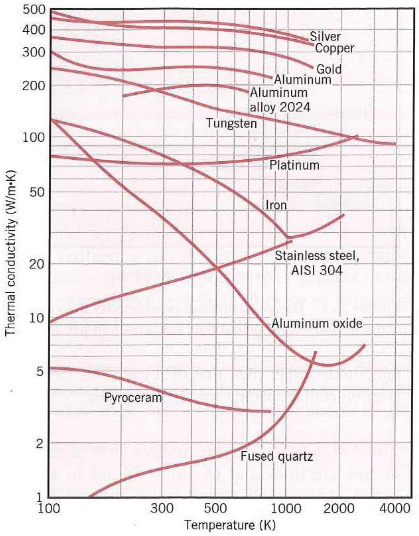

Figure 19: The temperature dependence of the thermal conductivity of selected solids [Incropera and DeWitt 2002, p. 56]

2.1.2 Convection heat transfer

Convection describes the heat transfer caused by motion of a fluid. Thereby energy is transferred both by molecular motion – also known as diffusion – and by macroscopic or bulk motion of the fluid. Whenever a temperature gradient exists large bulks of molecules that are moving collectively transfer heat.

An interesting convective heat transfer phenomenon is the one that occurs between a fluid in motion and a bounding surface (Figure 20). Therefore the so called boundary layer – a region that develops because of the fluid-surface interaction where the fluid velocity varies from zero at the surface to a finite value u_∞ associated with the flow – has a determinant relevance. This principle can be transferred to thermal phenomena. If the surface and flow temperatures differ a thermal boundary layer exists through which the temperature varies from T_s at $y = 0$ to T_∞ in the area of the flow. If $T_s > T_\infty$ heat transfer due to convection can be observed. Right next to the surface where $y = 0$ and therefore the flow velocity is also zero heat can only be transferred by molecular motion, thus conduction only. Towards the outer flow bulk fluid motion contributes significantly to the convective heat transfer.

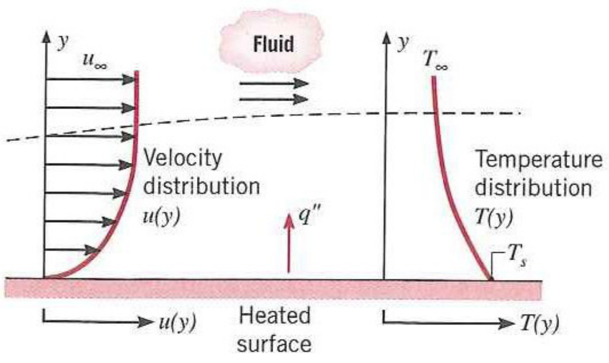

Figure 20: Boundary layer development in convection heat transfer [Incropera and DeWitt 2002, p. 6]

There are two types of convective heat transfer. We speak of forced convection if a surface is exposed to a flow that is caused by external means, such as winds, a fan or a pump. Contrary if a surface is only exposed to ambient room air, thus the flow is only influenced by buoyancy forces that are caused by density differences that occur because of temperature differences within the flow we speak of free convection.

The convective heat flux q'' $[W/m^2]$ is described by Newton's law of cooling

$$q'' = h(T_s - T_\infty) \tag{2.4}$$

The proportionality constant h $[W/m^2 \cdot K]$ is called convection heat transfer coefficient. It is determined by the flow conditions in the boundary layer that again is influenced by the surface geometry. For some problems an analytic calculation of h can be performed but usually it has to be determined experimentally.

2.1.3 Radiation heat transfer

Whereas conduction and convection mechanism require a medium to transfer energy heat transfer by radiation happens without any transporting medium (Figure 21). Responsible therefore is electromagnetic radiation that occurs whenever a temperature difference between two surfaces exits.

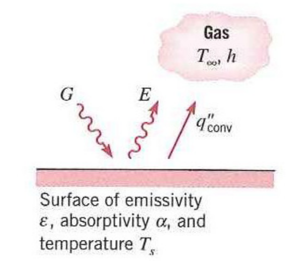

Figure 21: Radiation exchange at a surface [Incropera and DeWitt 2002, p. 9]

Thermal radiation that is emitted by a surface is related to its thermal energy. The energy emitted – also called emissive power E – is prescribed by the Stephan-Boltzmann law

$$E_b = \sigma T_s^4 \tag{2.5}$$

that describes emissive power of an ideal thermal radiator – also known as blackbody. Thereby T_s is the absolute Temperature $[K]$ of the surface and σ the so called Stephan-Boltzmann constant with the value of $5.669 \times 10^{-8}\, W/m^2 \cdot K^4$.

E_b is considered to be the maximum energy that can be emitted by an ideal radiator surface. Since real surfaces have less emissive power they can be described by

$$E = \varepsilon \sigma T_s^4 \tag{2.6}$$

where ε describes a surface property termed the emissivity. It describes how much energy a surface emits compared to a blackbody, hence $0 \le \varepsilon \le 1$ applies. These surfaces are called “grey”. A value of $\varepsilon = 0$ corresponds to all radiation being reflected by the surface. A value of $\varepsilon = 1$ corresponds to black body radiation where all energy is absorbed by the surface.

Equation (2.5) describes only the emissive power of a blackbody. The net radiant exchange q_{rad} $[W]$ between two parallel surfaces can be calculated with

$$q_{rad} = \varepsilon \sigma A (T_1^4 - T_2^4) \tag{2.7}$$

Another effect that needs to be considered is that in a real geometry not all the radiation leaving one surface will reach the other one. This is because electromagnetic waves are emitted in all directions and therefore only a certain amount of radiation is interacting with the opposite surface. The rest of the rays will be lost to the surroundings. The so called “view factor” function F_{ij} takes this effect into account. Thus the heat exchange between two arbitrary surfaces is

$$q_{rad} = F_{ij}\,\varepsilon\,\sigma\,A(T_1^4 - T_2^4) \tag{2.8}$$

The “view factor” function will be explained in detail in Chapter 3.5.1.

If radiation is incident on a surface from its surroundings we speak about irradiation G $[W/m^2]$. Thereby the radiation may be absorbed by the surface partly or totally increasing its thermal energy. The rate of incident radiation absorbed is determined by the absorptivity α. We get

$$G_{abs} = \alpha G \tag{2.9}$$

where $0 \leq \alpha \leq 1$. If the surface is opaque and $\alpha < 1$ the irradiation is reflected partly.

3 Development of heat transfer simulation methodology

Based on the previously discussed theory a heat transfer simulation methodology was developed. The development process and the achieved findings thereby will be presented in the following chapters.

3.1 Development process

To give an overview on the development process the work flow for the development of the heat transfer methodology is shown in Figure 22.

After the theoretical considerations about the heat transfer phenomena that occur in a dual-wall air gap insulated exhaust manifold a 3D Computer Aided Design (CAD) model was created with the thermal input from the exhaust manifold flow simulation that was carried out at the CFD skill team (DAC) of AVL. The next step was the generation of three different models, one for each radiation method available in ABAQUS/Standard. For each model a steady-state heat transfer was carried out. Afterwards the analysis results were compared and a first assortment was made. With the remaining models a transient heat transfer analysis was carried out to determine the necessary input for the following strength analysis. Finally a recommendation for future customer projects was made based on the results of the transient analysis.

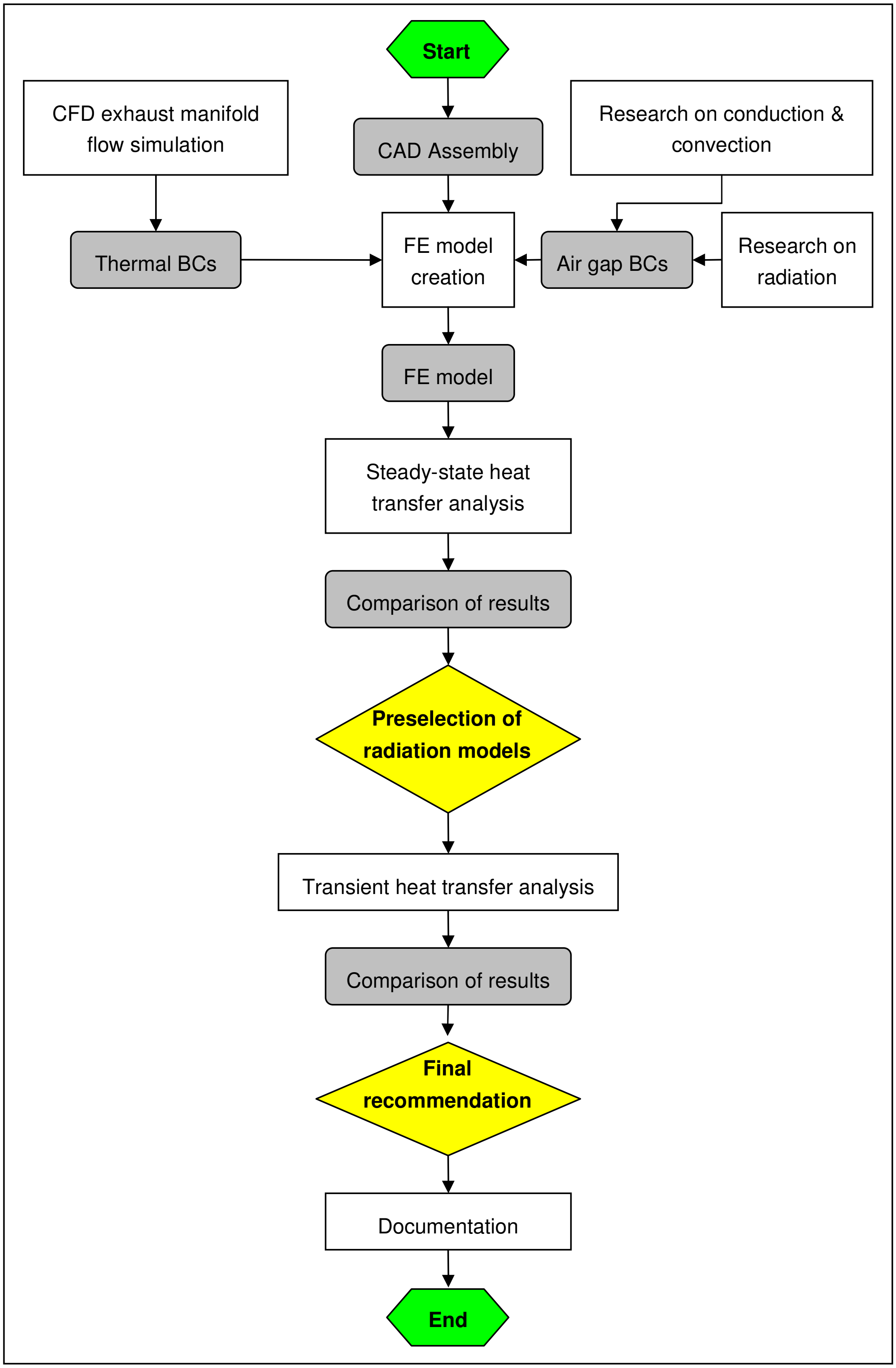

Figure 22: Work flow for heat transfer simulation methodology development

3.2 Heat transfer model of an air gap insulated exhaust manifold

An air gap insulated exhaust system can be described approximatively as shown in Figure 23 as an annular gap between two concentric cylinders. The inner wall is streamed through by hot exhaust gas that serves as inner boundary condition for the analysis. The outer wall is exposed to underhood flow that is influenced by the radiator, the fan and the movement of the vehicle itself. Furthermore radiation towards ambience has to be considered.

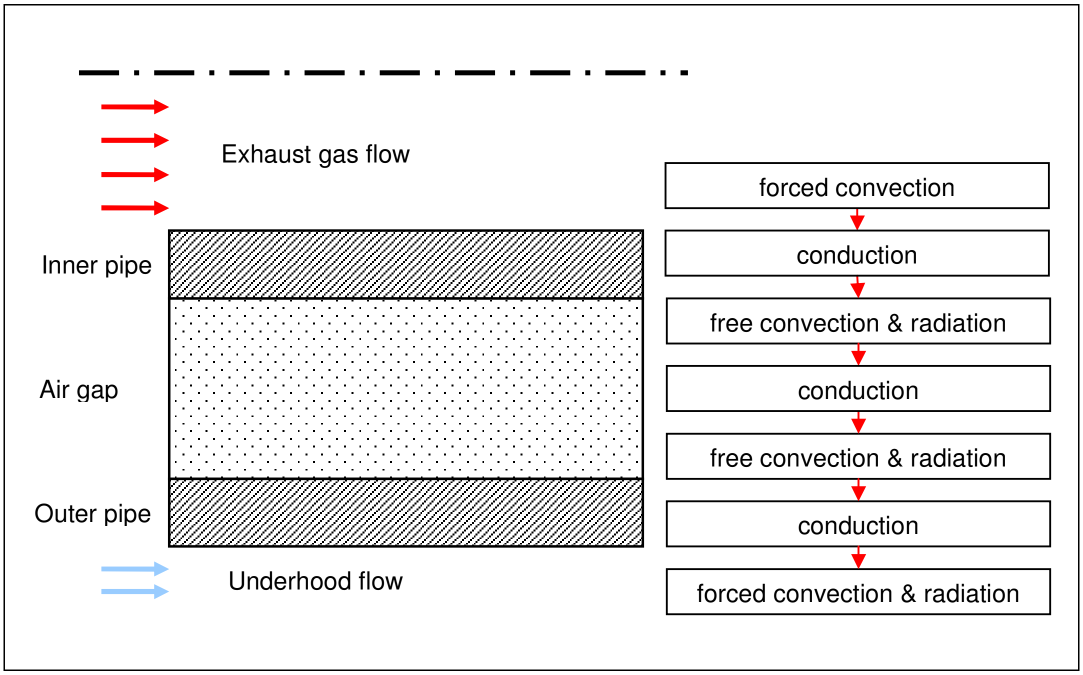

Figure 23: Analytical heat transfer path in air gap insulated exhaust systems

Responsible for the heat transfer in radial direction are the mechanisms described in chapters 2.1.1 to 2.1.3. The heat transfer from the exhaust gas to the inner wall happens due to forced convection as exhaust gas flow velocities up to $150\ m/s$ [AVL iCAE 2010] can be observed. Then heat is transferred through the solid inner wall due to conduction. As flow velocities are small within the air gap heat is transferred from the inner wall to the air gap due to free convection. In parallel heat is also transferred from the inner to the outer wall through radiation. Nevertheless the heat transfer through the air gap happens also due to conduction identical to the transfer through solid walls. Then again free convective heat transfer can be found from the air gap to the outer wall. In the following heat is conducted through the solid wall and finally released to the ambient through forced convection and radiation.

In axial direction heat is mainly transferred by conduction. But also the mechanism of radiation heat transfer is involved as electromagnetic waves are emitted in all directions.

3.3 Challenges in air gap heat transfer simulation

An air gap insulated exhaust manifold can be described in a simplified way as shown in Figure 23 where the heat flow proceeds from the hot exhaust gas outwards. The heat transfer happens because of the mechanisms described in chapters 2.1.1 to 2.1.3. Thereby the mechanisms of heat transfer in the annular enclosure between two cylinders play a fundamental role. The simulation of the temperature field in ABAQUS/Standard without a 3D CFD flow field analysis of the air gap implicates restrictions that need to be pointed out at this point.

The heat transfer in the air gap happens due to free convection, conduction and radiation. The heat flux due to convection and radiation is dependent on the temperatures of the mediums involved. For convective heat transfer described in equation (2.4) the surface temperature and the temperature of the fluid that exchange heat need to be known. The same applies for radiation where the temperatures of the heat exchanging surfaces need to be known for the calculation of the heat flux as described in equation (2.7).

The temperature dependence of the heat flux due to free convection leads to the following problems:

In a 3D ABAQUS/Standard heat transfer model there is no solid connection between the surfaces of the inner and outer pipes, hence heat cannot be transported to the outer pipe through the air gap. Nevertheless the temperature and the heat flux through the outer pipe need to be calculated. Convective boundary conditions cannot be set on the involved surfaces of the inner and outer pipe to describe the heat flux because the free convection heat transfer coefficient (HTC) depends on the surface and fluid temperatures that are unknown at the beginning of the analysis.

This problem is one of the biggest challenges in numerical heat transfer analysis of an air gap as an analytic calculation of the free convection HTCs is incorrect. To obtain a solution that is as exact as possible the convective heat transfer has to be substituted and described in an alternative way.

3.4 Modeling of free convection

Because of the non negligible influence of free convection on heat transfer within the air gap and the restriction that free convection cannot be respected with convective boundary conditions (for explanation see Chapter 3.3) heat transfer due to free convection has to be considered in the 3D ABAQUS/Standard model in an alternative way.

Throughout the literature several methods for the consideration of free convection can be found. The most common approach is to express the free convective heat transfer as conduction through the air gap. In other words the air gap is regarded to be a non moving solid layer with a conductivity that respects the heat transfer due to both free convection and conduction.

3.4.1 The approach of Raithby and Hollands

According to MacGregor and Emery [1969, pp. 391] the heat transfer in a fluid between two vertical plates with temperatures T_1 and T_2 within the distance δ can be estimated in dependency of the Grashof number Gr that is calculated as

$$Gr_\delta = \frac{g\beta(T_1 - T_2)\delta^3}{\nu^2} \tag{3.1}$$

The Grashof number is a dimensionless parameter that represents the natural convection effects and is a measure of the relative magnitude of the buoyancy force and the opposing viscous force acting on the fluid (Figure 24) [Çengel 2003, p. 465].

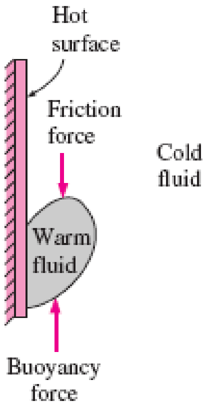

Figure 24: The Grashof number Gr [Çengel 2003, p. 465]

The meaning of the Grashof number in terms of free convective currents can be compared with the one of the Reynolds number Re for forced convection. Thus the Grashof number is an indicator for the flow state – laminar or turbulent – of free convective currents.

MacGregor and Emery [1969, pp. 391] state that if the Grashof number is low only small convective currents will occur and the heat transfer through the fluid layer will happen mainly due to conduction. Figure 25 underlines this statement by displaying the Nusselt number Nu

$$Nu_{\delta} = \frac{h\delta}{k} \tag{3.2}$$

which is a dimensionless measure for the intensity of energy transferred due to convection comparing the convective heat transfer coefficient h with the conductive one k versus the Rayleigh number Ra_L which is commonly used to express free convective correlations and can be written with the Prandtl number Pr

$$\mathrm{Pr} = \frac{\nu}{\alpha} \tag{3.3}$$

as

$$Ra_L = Gr\,\mathrm{Pr} \tag{3.4}$$

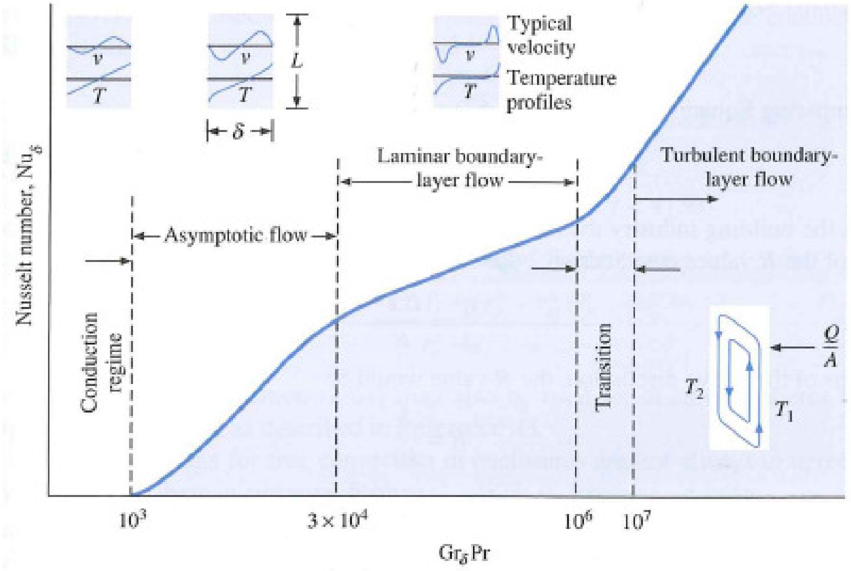

Figure 25: Schematic diagram and flow regimes for the vertical convection layer [Holman 2010, p. 347 cited after MacGregor and Emery 1969, pp. 391]

As increasing Grashof numbers indicate a turbulent flow which again implicates an energy transfer by convection this heat transfer phenomena cannot be neglected.

Based on the previous explanations the convective heat flux is calculated as

$$\frac{q}{A} = q'' = h(T_1 - T_2) = Nu_\delta \frac{k}{\delta}(T_1 - T_2) \tag{3.5}$$

With

$$Nu_\delta = \frac{k_{eff}}{k} \tag{3.6}$$

where k_{eff} is the effective thermal conductivity which is the thermal conductivity that a stationary fluid should have to transfer the same amount of heat as the moving fluid [Incropera and DeWitt 2002, p. 565]. Equation (3.5) can be also written as

$$\frac{q}{A} = k_{eff} \frac{(T_1 - T_2)}{\delta} \tag{3.7}$$

For the heat transfer due to free convection in an annular gap between two long, horizontal concentric cylinders Raithby and Hollands [1976, pp. 281] suggested the following correlation for k_{eff}

$$\frac{k_{eff}}{k} = 0.386 \left(\frac{\Pr}{0.861 + \Pr} \right)^{0.25} (Ra_c^*)^{0.25} \tag{3.8}$$

where the dimensionless Rayleigh number Ra_c^* can be written with the Rayleigh number Ra_L described in equation (3.4)

$$Ra_L = Gr \Pr = \frac{g\beta(T_i - T_o)\delta^3}{\nu\alpha} \tag{3.9}$$

as

$$Ra_c^* = \frac{\left[\ln(D_o/D_i)\right]^4}{\delta^3 (D_i^{-3/5} + D_o^{-3/5})^5} Ra_L \tag{3.10}$$

According to Raithby and Hollands [1976, pp. 281] equation (3.10) can be used for the range $10^2 \le Ra_c^* \le 10^7$. They state that for $Ra_c^* < 100$ the influence of convection can be neglected and $k_{eff} \approx k$.

In the case of the air gap insulated exhaust manifolds where the inner pipe is heated by hot exhaust gas and the outer is cooled by underhood flow ($T_i > T_o$), fluid ascends along the hot inner pipe and descends along the outer pipe because of its increasing density as it is cooled down, compare Figure 26. With equation (3.8) the heat transfer rate per unit length of cylinder q' $[W/m]$ due to free convection can be described as

$$q' = \frac{2\pi k_{eff}}{\ln(D_o/D_i)}(T_i - T_o) \tag{3.11}$$

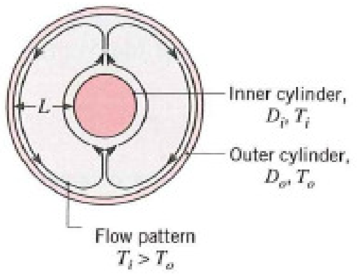

Figure 26: Free convection flow in the annular space between long, horizontal, concentric cylinders or concentric spheres [Incropera and DeWitt 2002, p. 565]

3.4.2 Effects of air gap size on convection heat transfer

If we calculate the dimensionless Rayleigh number Ra_C^* in dependency of the air gap temperature for two typical ratios – 1.1 and 1.3 – of D_o and D_i applying equations (3.10) and (3.9) which is relevant for the calculation of k_{eff} we get the results shown in Figure 28 for $D_o/D_i = 1.1$ and in Figure 29 for $D_o/D_i = 1.3$. For the creation of Figure 28 and Figure 29 temperature dependent material data (Appendix A.1) was used based on Incropera and DeWitt [2002, p.917] and the outer walls temperature was assumed to be half of the inner wall temperature, e.g. $T_o = 500\ °C$ for $T_i = 1000$.

According to the AVL iCAE [2010] benchmark shown in Figure 27 wall temperatures in operating conditions are in the range of $600\ °C$ to $1000\ °C$. From the results it can be said that for this temperature range $Ra_c^* < 100$ for typical pipe dimensions of air gap insulated exhaust manifolds.

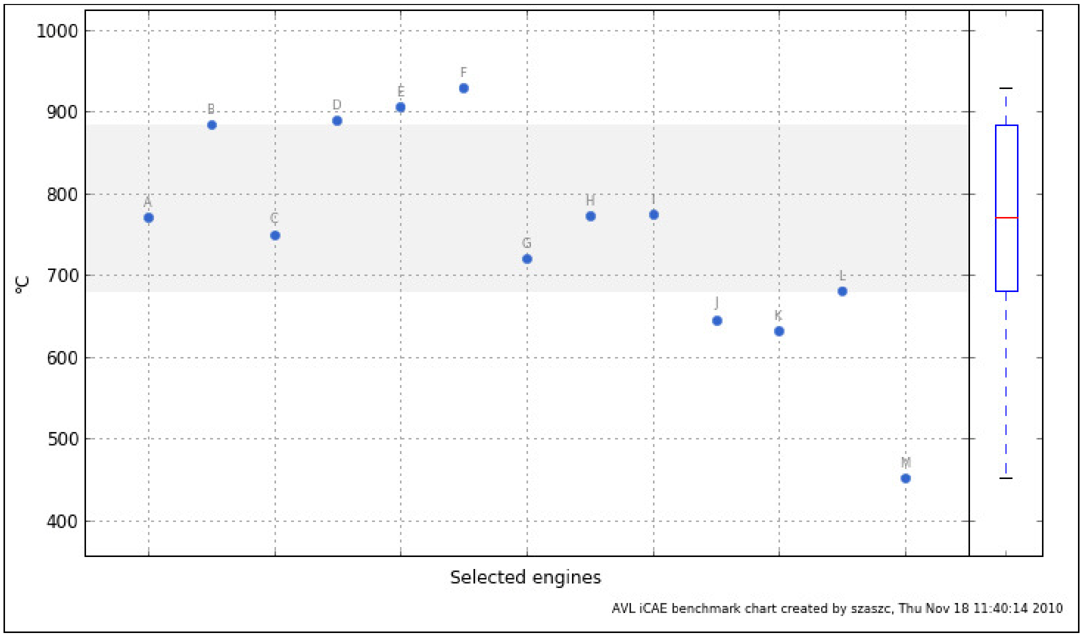

Figure 27: Wall temperature of exhaust manifolds [AVL iCAE 2010]

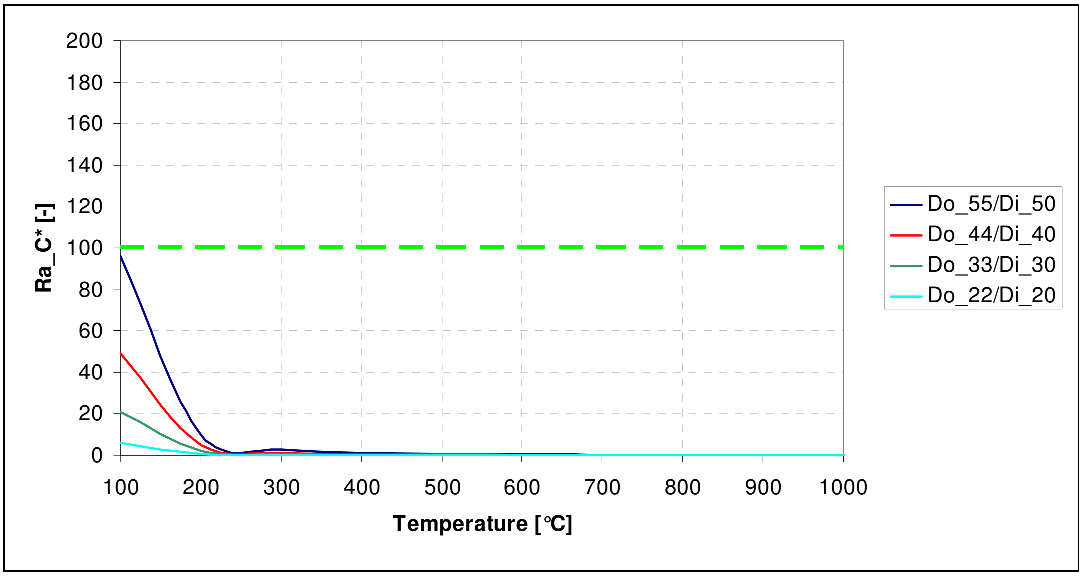

Figure 28: Correlation of Rayleigh number and air gap temperature for $D_o / D_i = 1.1$

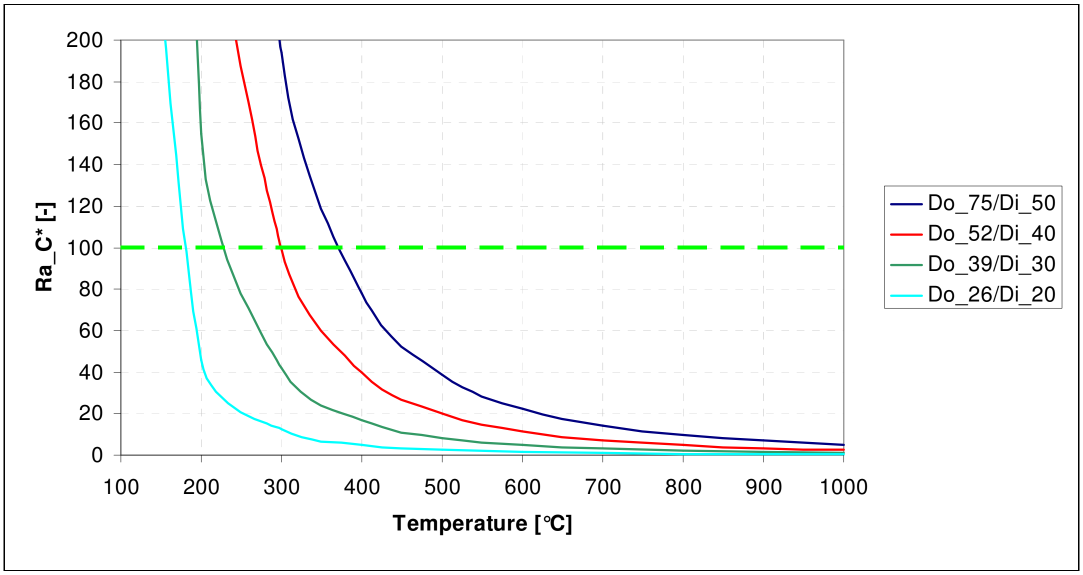

Figure 29: Correlation of Rayleigh number and air gap temperature for $D_o/D_i = 1.3$

Thereby it can be observed that the Rayleigh number Ra_L described in equation (3.9) decreases where temperature difference $\Delta T = T_i - T_o$ increases. As the Rayleigh number Ra_L is determined by the Prandtl number $\Pr$ and the Grashof number Gr which is the indicator for the free convective flow state it can be said that with the temperature difference ΔT increasing the flow state tends to be laminar.

Another clear statement can be made by looking at equation (3.10). As the ratio D_o/D_i is kept constant for all diameters used for the calculations in Figure 28 and Figure 29 it can be also said that the absolute diameters of the pipes influence the Rayleigh number Ra_C^*. Furthermore by comparing the results for $D_o/D_i = 1.1$ and $D_o/D_i = 1.3$ it can be seen that with increasing gap-sizes the dimensionless Rayleigh number Ra_C^* also increases.

From these observations it can be concluded that the heat transfer mechanisms in the annular space between long, horizontal, concentric cylinders are mainly determined by the temperature difference ΔT between the surfaces of the inner and outer pipes. The geometric circumstances such as the diameter of the pipes and the size of the air gap only shift the overall level of the curves displayed in Figure 28 and Figure 29.

According to Raithby and Hollands [1975, pp. 281] it can be concluded that the effects of free convection on heat transfer through the air gap are very low and can be neglected, see Chapter 3.4. For the warming up phase where wall temperatures are under $400\ °C$ free convection needs to be considered according to the results presented in Figure 28 and Figure 29. Due to the short duration of this process and as the convective heat transfer rate is very low compared to conduction and radiation it can be said that the effects of free convection can be also neglected for this operating condition. With $k_{eff} \approx k$ the effects of conduction and radiation represent the heat transfer over the air gap sufficiently.

3.5 Modeling of radiation heat transfer

Radiation heat transfer is one of the biggest issues in terms of heat transfer over an air gap insulated exhaust pipe. The following chapters give an overview of how radiation is treated by ABAQUS/Standard.

3.5.1 The geometric view factor

Besides temperature differences radiation heat transfer strongly depends on the problems geometric circumstances. The view factor F_{ij} is defined as the fraction of the radiation leaving surface i being intercepted by surface j [Incropera and DeWitt 2002, p. 790].

For the calculation of radiation heat transfer between two surfaces that is shown in Figure 30 ABAQUS/Standard uses

$$F_{ij} = \frac{1}{A_i} \int_{A_i} \int_{A_j} \frac{\cos\theta_i \cos\theta_j}{\pi R^2} dA_i dA_j \tag{3.12}$$

where R is the distance from a point on surface A_j to a point on surface A_i. The angles θ_i and θ_j are measured between the line R and the normals to the surfaces. Generally a view factor can be calculated for any given geometry with equation (3.12). Note that the calculation of view factors becomes more complex when solid bodies are interposed between radiating surfaces blocking some of the possible paths where heat can be exchanged.

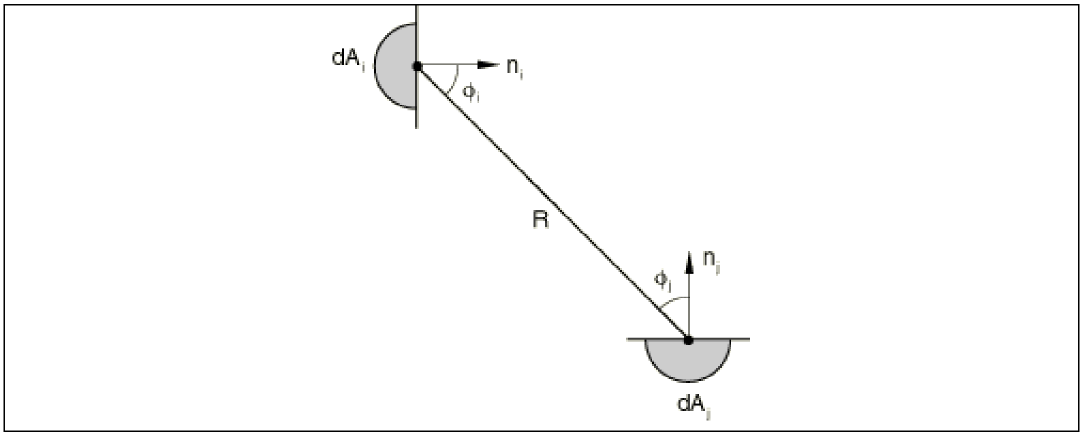

Figure 30: Nomenclature for enclosed radiation [Simulia Inc. 2010]

An important property of the view factor in an enclosed cavity, that allows to check the accuracy of the calculation is

$$\sum_{j=1}^{N} F_{ij} = 1 \tag{3.13}$$

The result of this sum is equal one as a result of that all the rays leaving surface i must strike some other surface j in a closed cavity. In open cavities this sum is always less than one.

To calculate radiation exchange in an enclosure of N surfaces a total of N^2 view factors is required that becomes evident when the view factors are arranged in the matrix form.

$$\begin{bmatrix} F_{11} & F_{12} & \cdots & F_{1N} \\ F_{21} & F_{22} & \cdots & F_{2N} \\ \vdots & \vdots & & \vdots \\ F_{N1} & F_{N2} & \cdots & F_{NN} \end{bmatrix}$$

Because of the geometrical discretization of numerical problems the number of surfaces (or facets) that exchange heat over radiation is very high. For example for the exhaust manifold geometry model used for the development of the simulation methodology $N \approx 3\times10^4$ that leads to $N^2 = 9\times10^8$ view factors. The calculation of the view factor matrix therefore takes a very long time that makes the numerical analysis of an exhaust manifold unacceptably long.

3.5.2 ABAQUS/Standard modeling approach and simulation technique

In ABAQUS/Standard there are three approaches for modeling radiation heat transfer in a surface enclosure.

1. The fully implicit cavity radiation method
2. The approximate cavity radiation method
3. Gap radiation property in surface-to-surface contact definition (termed surface normal radiation method in the following)

The theory on which cavity radiation in ABAQUS/Standard is based on is well-known and can be found in [Holman 1990] and [Siegel and Howell 1980]. These techniques will be explained in detail in the following chapters based on [Simulia Inc. 2010].

3.5.2.1 The fully implicit radiation method

The fully implicit radiation method considers the angular variation of the heat flux (Figure 31) that results from different view factors, different facet temperatures and different emissivities. The radiation flux per unit area into a facet can be expressed as

$$q_i'' = \sigma \varepsilon_i \sum_{j=1}^{N} \varepsilon_j \sum_{k=1}^{N} F_{ik} C_{kj}^{-1} \left(\theta_j^{\,4} - \theta_i^{\,4} \right) \tag{3.14}$$

where θ_i and θ_j are the temperatures of facets i and j. The matrix $F_{ij} C_{kj}^{-1}$ that consists of the geometrical view factor matrix F_{ij} and the reflection matrix C_{ij}, where

$$C_{ij} = \delta_{ij} - (1 - \varepsilon_i) F_{ij} \tag{3.15}$$

couples the temperatures at all points of the surface to each other is non symmetric and fully populated. Therefore calculations with the fully implicit method are computationally very expensive. To avoid excessive computation time and memory usage fully implicit cavity radiation problems are limited to 16000 nodes in ABAQUS/Standard version 6.10. For future releases higher limits are promised by the software’s manufacturer Simulia Inc [Simulia Inc. 2010].

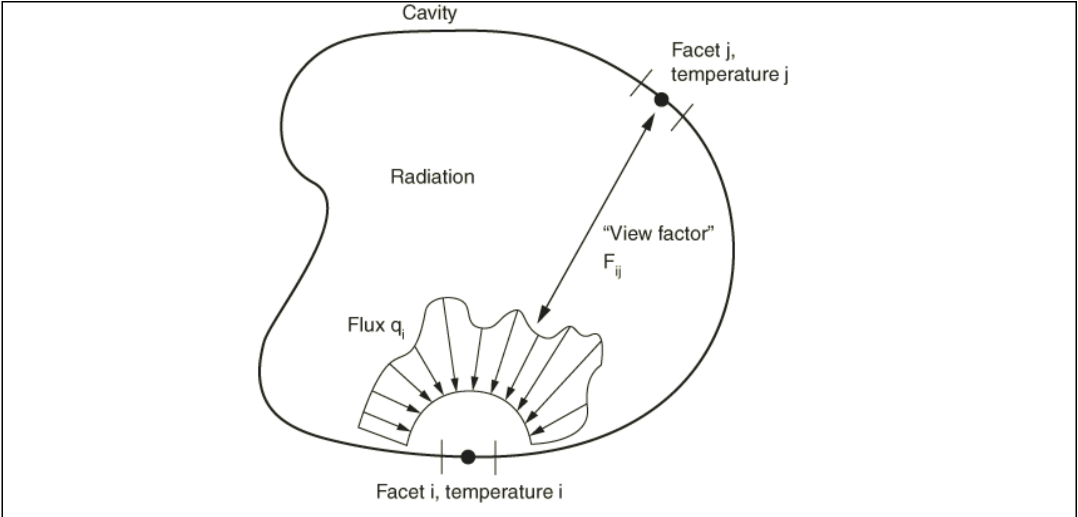

Figure 31: Radiation flux in the fully implicit radiation method [Simulia Inc., 2010]

3.5.2.2 The approximate radiation method

The approximate radiation model (Figure 32) is a simplified numerical model based on physical and geometric assumptions. Thereby view factors are regarded as uniform for all facets and blocking effects are neglected. This results in the following approximation

$$F_{ij} = \frac{A_j}{A_{total}} \tag{3.16}$$

where A_j is the area of facet j and

$$A_{total} = \sum_{j=1}^{N} A_j \tag{3.17}$$

The interpretation of this assumption is that each facet has an equal view of every other facet. With the emissivity taken as constant for all surfaces and reflections ignored the radiation flux per unit area over a facet becomes

$$q_i'' = \sigma\varepsilon_i \sum_{j=1}^{N} \frac{A_j}{A_{total}} \left(\theta_j^{\,4} - \theta_i^{\,4}\right) \tag{3.18}$$

With the definition of an average temperature

$$\theta_{AVG}^4 = \frac{1}{A_{total}} \sum_{j=1}^{N} A_j \theta_j^{\,4} \tag{3.19}$$

we get a simple equation for the flux

$$q_i'' = \sigma\,\varepsilon_i \left(\theta_{AVG}^4 - \theta_i^{\,4}\right) \tag{3.20}$$

By considering these simplifications the required memory and time for computation can be reduced significantly.

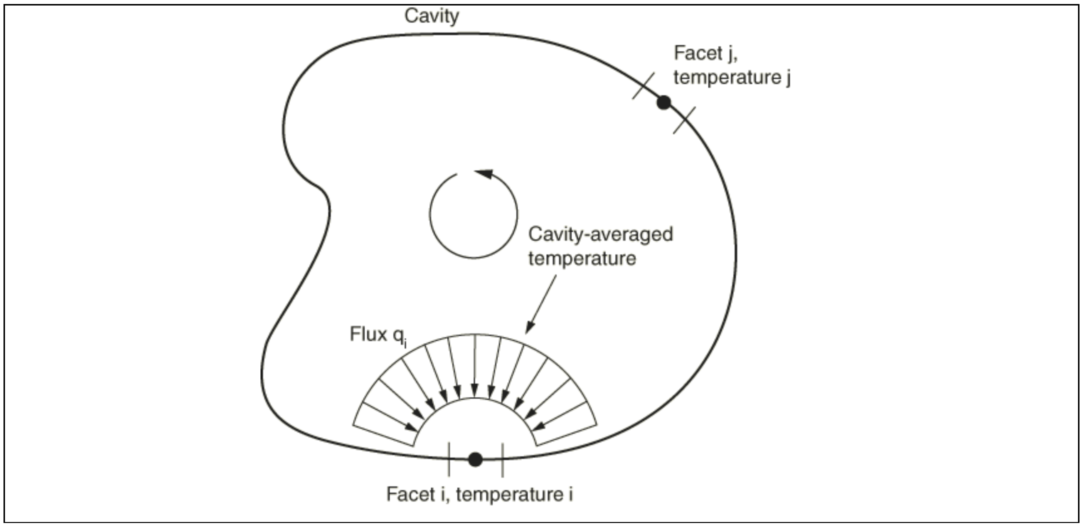

Figure 32: Radiation flux in the approximate radiation method [Simulia Inc. 2010]

3.5.2.3 Gap radiation property in surface-to-surface contact definition

Another possibility for modeling radiation heat transfer in ABAQUS/Standard can be found in the surface-to-surface interaction module. Thereby a property for radiation is defined for a standard surface-to-surface contact. Note that, heat transfer across the interface occurs only in the normal direction with this formulation, see Figure 33.

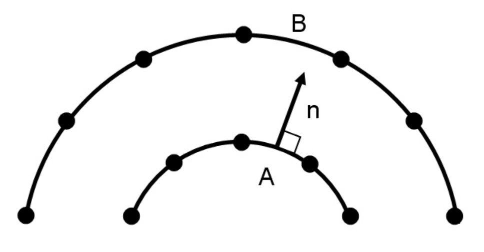

Figure 33: Radiation flux in the surface normal radiation method

The heat flux per unit surface area crossing the gap from surface A to surface B can be described as

$$q'' = C\left(\theta_A{}^4 - \theta_B{}^4\right) \tag{3.21}$$

where C is the gap radiation constant given by

$$C = \frac{F\sigma}{1/\varepsilon_A + 1/\varepsilon_B - 1} \tag{3.22}$$

As this is a surface to surface interaction the view factor F must be defined as a function of the gap clearance d as shown in Figure 34.

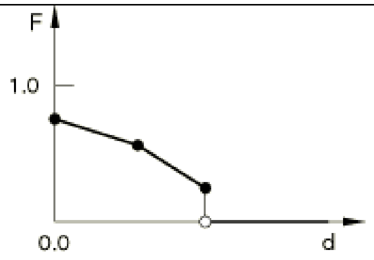

Figure 34: Example of input data to define the view factor as a function of clearance [Simulia Inc. 2010]

As heat transfer within this formulation happens only in normal direction to the respective facet this method will be referred to as “surface normal radiation method” in the following.

3.6 Steady-state heat transfer and radiation method testing

To verify the accuracy and performance of the modeling approaches described in Chapter 3.5.2 a comparative analysis of an existing dual-walled air gap insulated exhaust manifold was performed. Thereby the boundary conditions are the same for all the models. Only the simulation technique for modeling radiation heat transfer from the inner gas guiding pipes to the outer pipes varied. After the introduction of the ABAQUS/Standard simulation model the results obtained with the different radiation methods will be discussed in the following chapters.

3.6.1 The 3D FEM Simulation model

The 3D FEM exhaust manifold simulation model used for the development of the simulation methodology is presented in Figure 35. The exhaust manifold geometry is taken from a turbocharged V6 engine with 2.7 liter displacement that was developed at AVL in the year 2002 within a customer project.

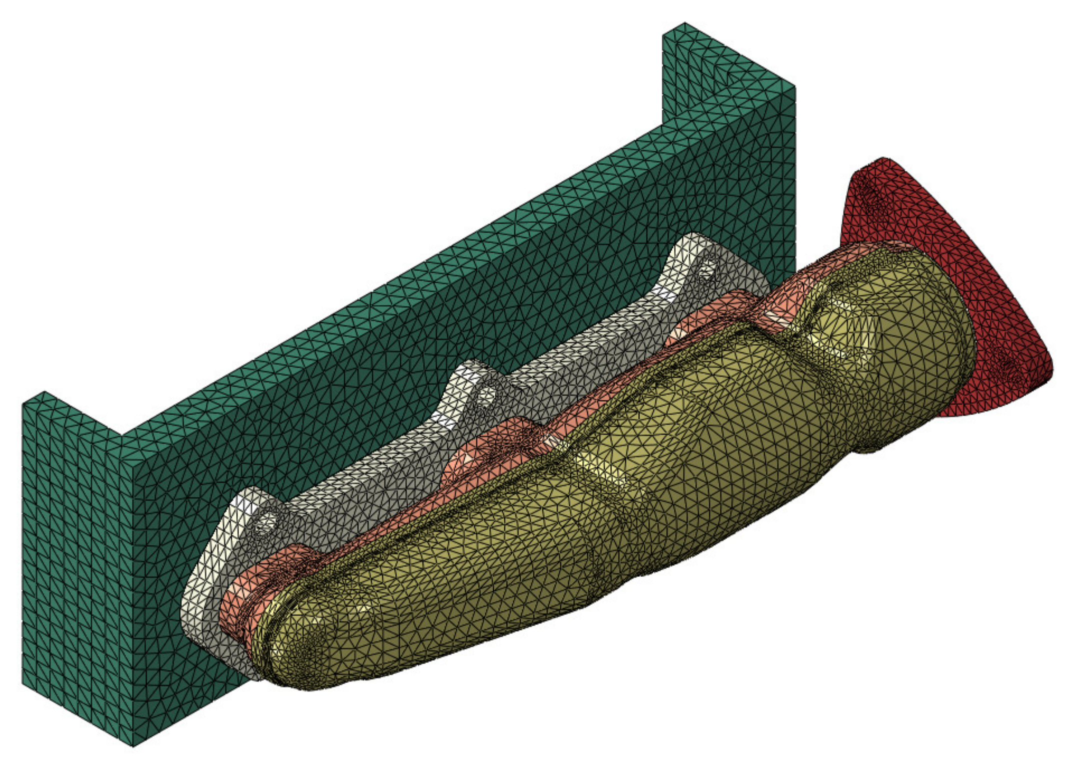

Figure 35: ABAQUS/Standard 3D FEM model

To minimize computational costs linear, tetrahedral elements of type DC3D4 were used for the discretization of all parts. Thereby special attention was given to the meshing of the radiation exchanging surfaces. Because the fully implicit radiation method in ABAQUS/Standard only features up to 16000 facets the mesh of the interacting surfaces of the cavity was chosen in respect to this restriction.

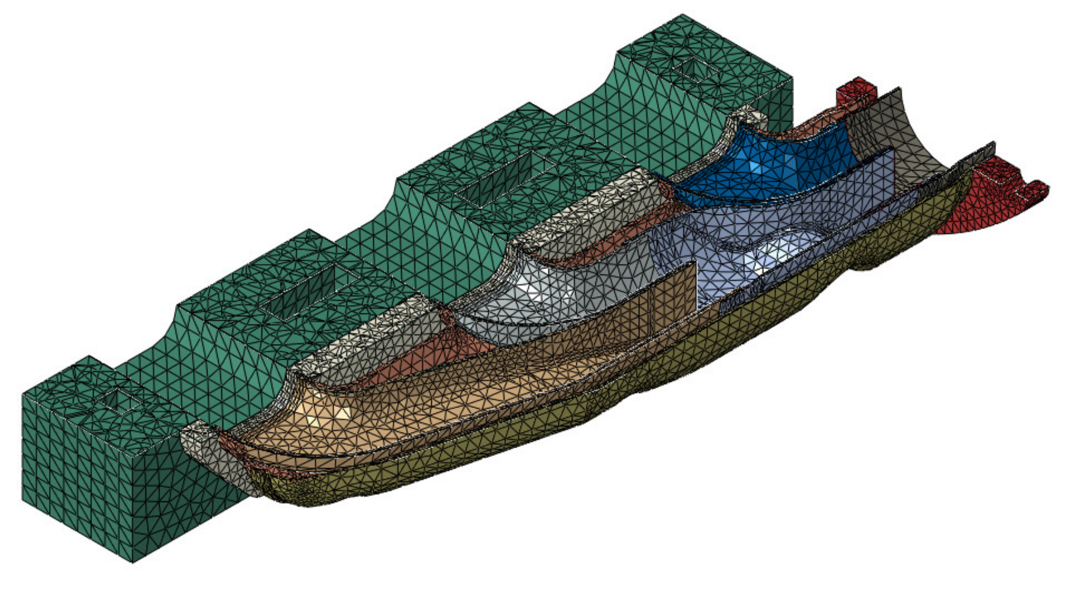

Figure 36: Horizontal cut through the exhaust manifold geometry

3.6.1.1 Material properties

Temperature dependent material data was used for the finite element (FE) analysis of the exhaust manifold. Thereby austenitic steel X15CrNiSi20-12 was used for the flanges and all gas guiding pipes. Taking the findings concerning thermal deformations discussed in Chapter 1.1.4 into consideration ferritic steel X2CrTiNb18 was used for the outer pipes. The material properties were taken from the AVL material database.

3.6.1.2 Mechanical boundary conditions

All parts of the exhaust manifold assembly, that can be seen in Figure 36 are connected with one another in respect to the manufacturing process. Therefore all appropriate contact surfaces are tied together. This boundary definition sufficiently represents the heat transfer due to contact between two parts.

3.6.1.3 Thermal boundary conditions

The thermal boundary condition, which respects the exhaust gas flow, was taken from a CFD analysis of the exhaust manifold flow. The analysis was carried out by AVL's CFD skill team. The distribution of the cycle averaged heat transfer coefficients and fluid temperatures on the gas guiding pipes can be seen in Figure 37 and Figure 38.

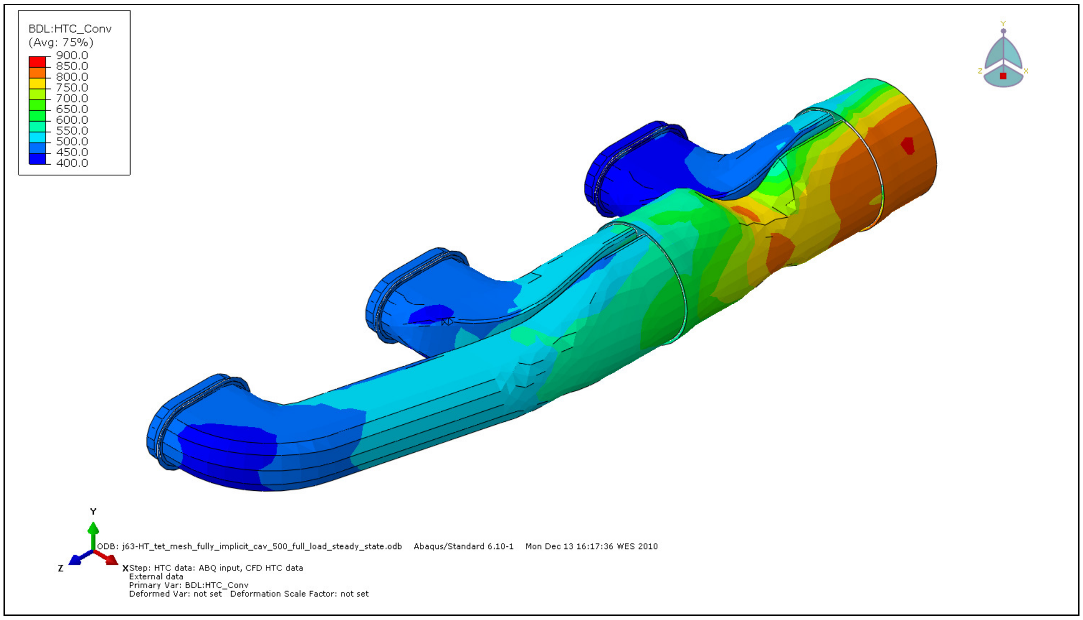

Figure 37: HTC distribution on gas guiding surfaces [AVL DAC 2010]

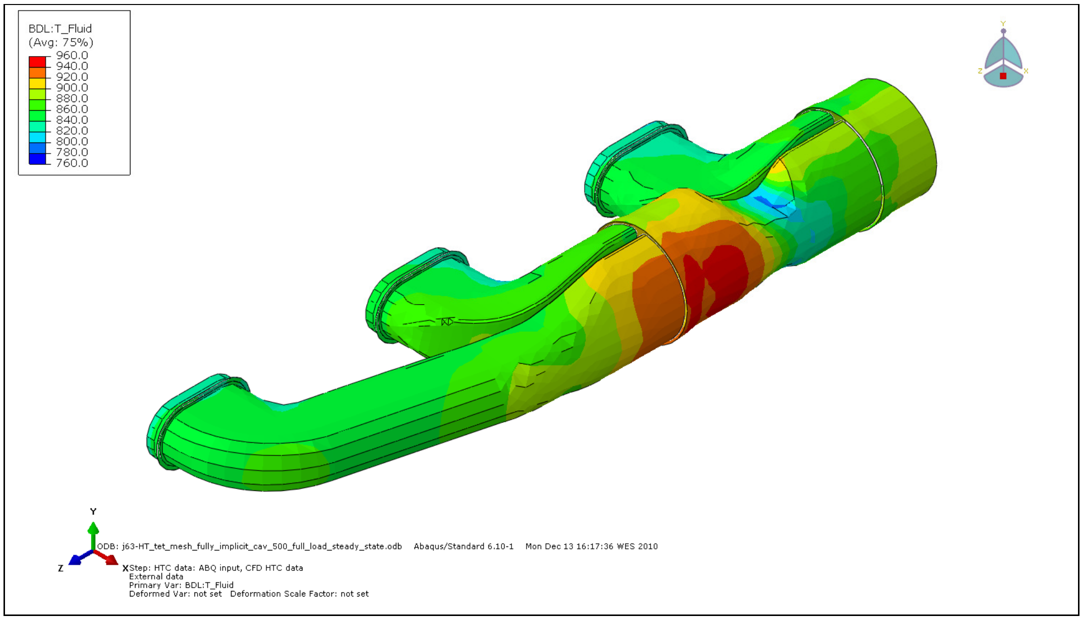

Figure 38: Fluid temperatures on gas guiding surfaces [AVL DAC 2010]

On the surfaces that are in contact with the ambient and are therefore exposed to underhood flow a constant HTC of $15\,W/m^2 \cdot K$ at a temperature of $75\,°C$

and a surface radiation property to ambient with $T_{amb} = 30\ °C$ and $\varepsilon = 0.2$ was defined as boundary condition. For those cylinder head surfaces that are in contact with fluids the thermal boundaries are listed in Table 2.

Table 2: Thermal boundaries on cylinder head

	HTC [$W/m^2 \cdot K$]	T_FLUID [$°C$]
Exhaust ports	450	750 @ Full load; 275 @ Motored
Oil jacket	140	130
Water jacket	10000	90

Note that all boundary conditions are based on AVL experience and were chosen in respect to the engine arrangement.

3.6.1.4 Air gap boundary condition

As described in Chapter 3.4.2 the heat conductance through the air gap has to be considered. In ABAQUS/Standard this can be done with the so called gap-conductance property which can be defined in line with a surface-to-surface contact definition. Thereby heat transfer is assumed only in normal direction to the facet. The heat flux per unit area crossing the gap between points A and B can be written as

$$q'' = h_{\delta}(\theta_A - \theta_B) \tag{3.23}$$

where k is the gap conductance that has to be defined by the user as a function of gap clearance.

From equation (3.23) it can be seen that the heat flux is calculated after Newton's law of cooling (equation (2.4)), hence the gap clearance is not taken into account as required after equation (2.1). For gaps that can be regarded as small in comparison to the surface this approach represents the effect of heat conduction sufficiently. However for gap-sizes that can be found typically in dual-wall exhaust manifolds a simple work-around has to be done. By calculating

$$h_{\delta} = \frac{k}{\delta}$$

where k is the thermal conductivity of air and δ is the air gap size the heat conduction through the air gap is represented correctly.

The values for h_δ that were used in ABAQUS/Standard are listed in Appendix A.3. They are based on thermophysical properties of air at atmospheric pressure (Appendix A.2) that can be found in Baehr and Stephan [2008, p. 723].

3.6.2 Temperature field result of the fully implicit radiation method

The temperature distribution that was calculated with the fully implicit method can be seen in Figure 39 and Figure 40.

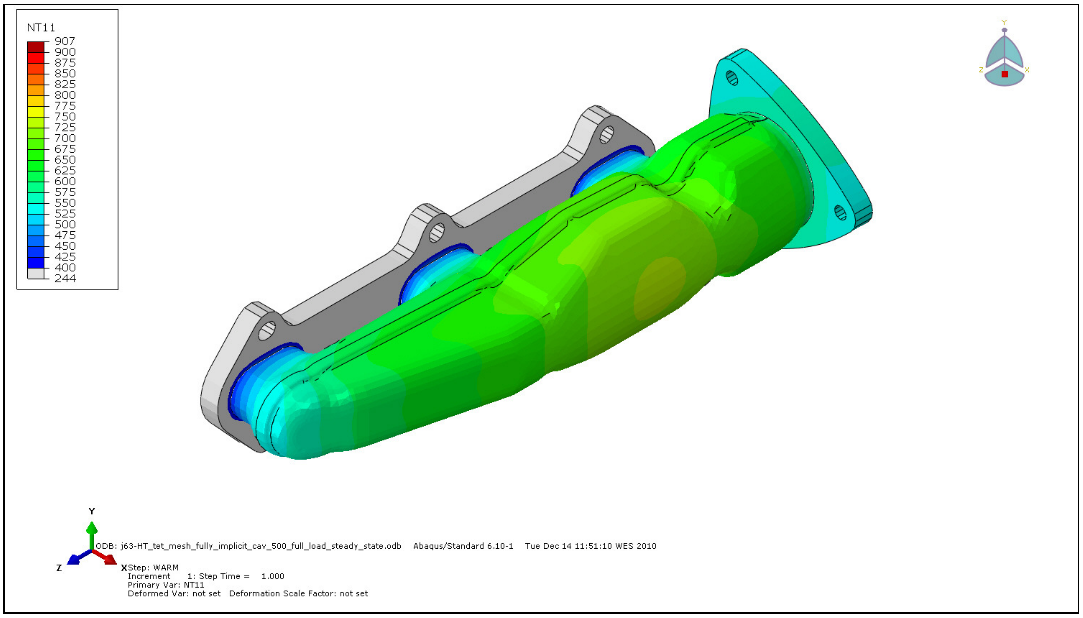

Figure 39: Temperature distribution determined with the fully implicit radiation method

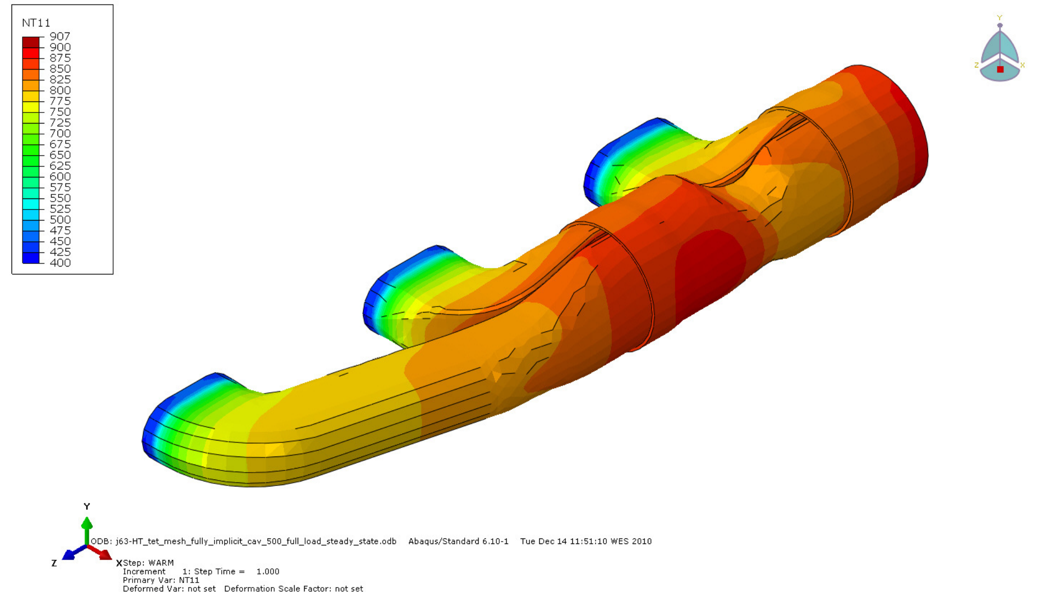

Figure 40: Temperature field of inner piping calculated with the fully implicit method

This method is considered to be the most exact one because the radiation heat flux for every facet is calculated with the respective view factor. Due to this fact the temperature field evaluated with the fully implicit method is regarded as reference in the following discussions. The temperature distributions obtained with the other radiation methods described in Chapter 3.5.2 will be compared to the results delivered by the fully implicit radiation method.

3.6.2.1 Notes to the usage of symmetry definitions

During the procedure of simulation methodology development several attempts were undertaken to minimize the computational costs of the fully implicit radiation method. As ABAQUS/Standard features the definition of radiation symmetries numerous calculations were done with all kinds of symmetry definitions. Unfortunately, all analysis results showed incorrect temperature fields in the area of symmetry planes so it can be said that the usage of symmetry definitions in the fully implicit radiation method is ineligible.

3.6.2.2 Notes to the usage of multiple cavity radiation definitions

Another observation made during the analysis procedure concerns the definition of multiple cavity radiation interactions for one radiation exchanging surface assembly. The motivation therefore is to avoid the modeling limitation of 16000 interacting facets within one cavity definition. Especially for large exhaust manifold models the number of 16000 facets is little, hence only a very coarse mesh can be used. However it could be observed that the definition of two adjacent cavities delivers incorrect temperature field distributions in the transition section between the cavities. This means that only the definition of a single cavity radiation interaction for a radiation exchanging area delivers a correct temperature field.

3.6.3 Temperature field result of the approximate radiation method

The temperature field that was determined with the approximate radiation method is presented in Figure 41 and Figure 42.

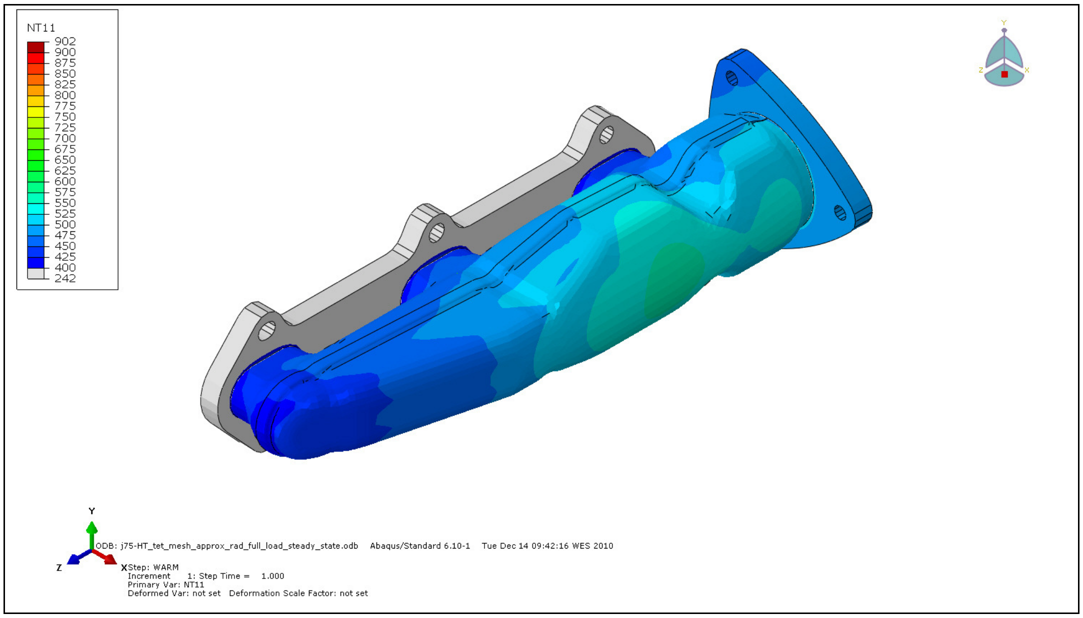

Figure 41: Temperature distribution determined with the approximate radiation method

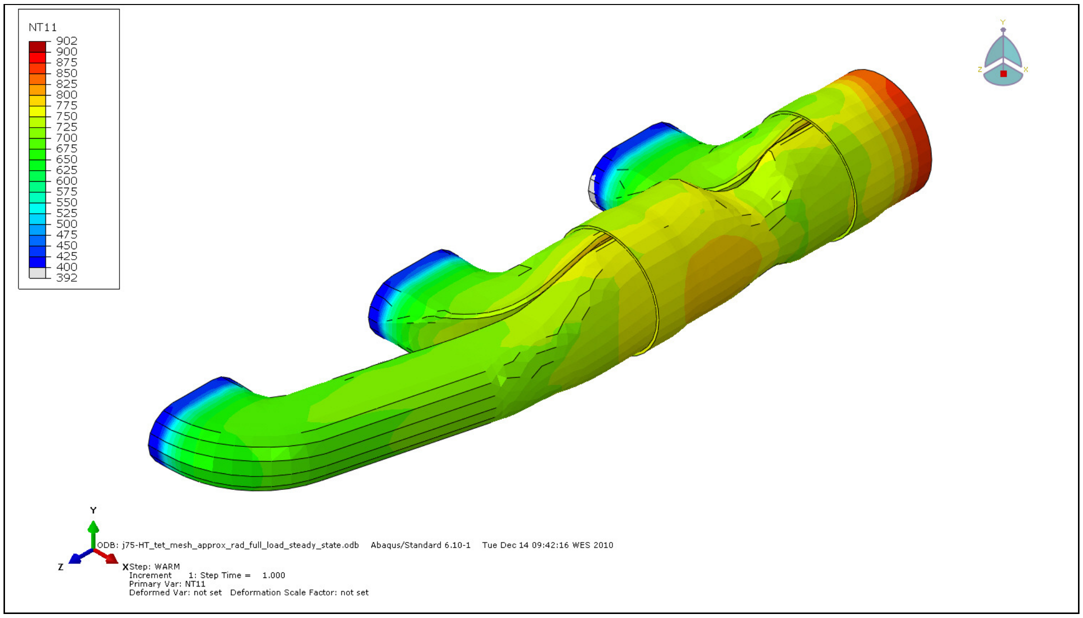

Figure 42: Temperature field of inner piping calculated with the approximate radiation method

It can be seen that both the temperature distribution and the temperature level significantly differ from the ones calculated with the fully implicit radiation method that is considered to be the reference model. The explanation therefore can be found in the treatment of radiation exchanging surfaces and is revealed by the heat balance that is shown in Table 3.

Table 3: Heat balance of approximate radiation method

	Heat flux across surface with approximate radiation method $[W]$
Surfaces to ambient	518
Exhaust pipe (gas side)	-3765
Exhaust ports	-3403
Exhaust pipe inner (air gap side)	3123
Exhaust pipe outer (air gap side)	-648
Oil jacket	756
Water jacket	3356
BALANCE	**-63**

From the thermal balance of the air gap it can be expected that the energy input must be equal to the output, hence the heat flux across the surfaces “Exhaust pipe inner” and “Exhaust pipe outer” should be the same. Because of the fact that the heat flux across the surface “Exhaust pipe inner” is 4.8 times higher than the one across “Exhaust pipe outer” it can be concluded that the radiation exchange between the interacting surfaces is not calculated correctly. According to the definition used in the method no surface blocking is taken into account (for explanation see chapter 3.5.1) for which reason the model does not recognize the defined air gap surfaces as radiation exchanging partners. Hence rays that are emitted by the surfaces of the inner piping are considered to interact with the surfaces on the opposite side of the same part and not with the outer pipes.

Due to this characteristic it can be said that the approximate radiation method cannot be used for problems where radiation energy exchange occurs over an annular gap between two concentric surfaces.

3.6.4 Temperature field result of the surface normal radiation method

Figure 43 and Figure 44 show the temperature field results obtained with the surface normal radiation approach.

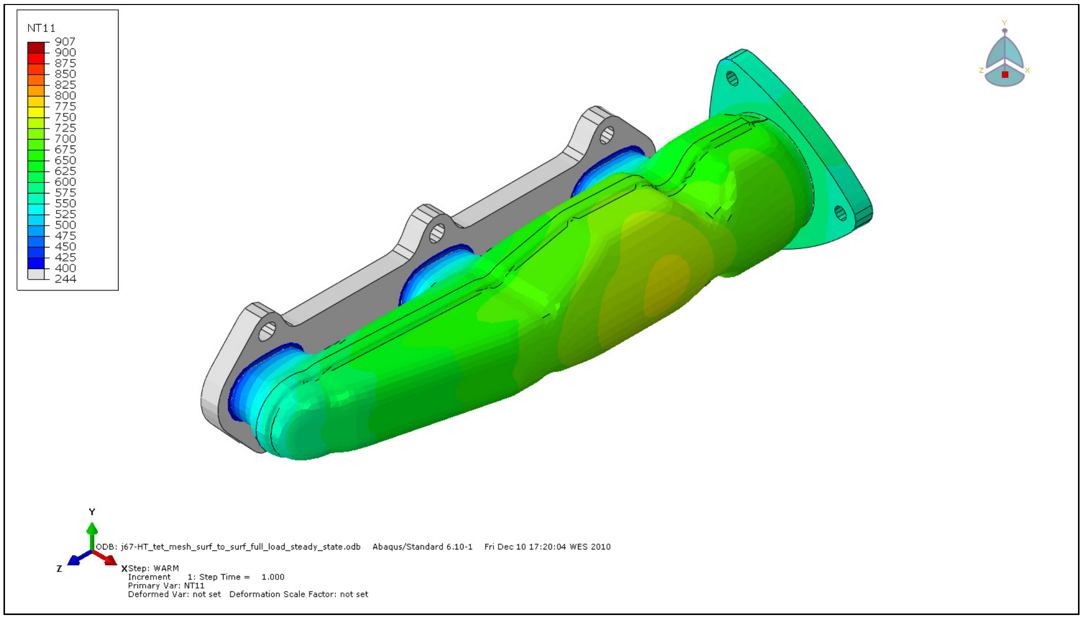

Figure 43: Temperature distribution determined with the surface normal radiation method

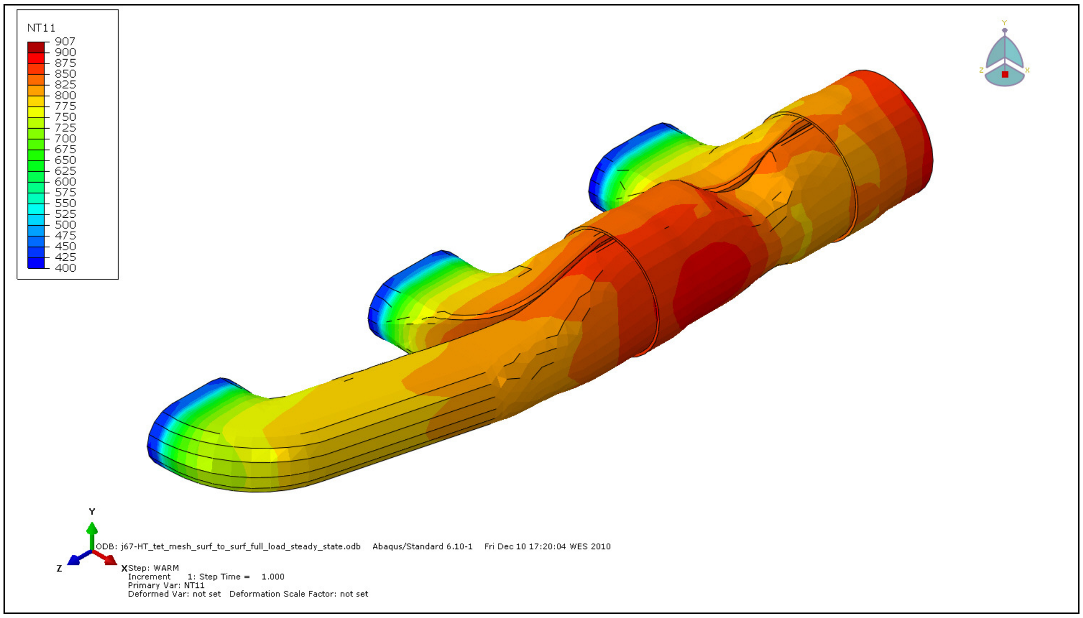

Figure 44: Temperature field of inner piping calculated with the surface normal radiation method

This method delivers a similar temperature field distribution as the fully implicit approach. Significant deviations occur only in regions where the exhaust manifold geometry is strongly differing from the idealized assumption of two concentric cylinders with an annular gap in between. Furthermore a difference in temperature level can be observed. Overall this method delivers higher temperatures than the fully implicit approach. This can be explained by looking at the mathematical definition of this radiation method.

The heat flux due to surface normal radiation is calculated after equation (3.21) as

$$q'' = C\left(\theta_A{}^4 - \theta_B{}^4\right)$$

Thereby the constant C is defined after equation (3.22) as

$$C = \frac{F\sigma}{1/\varepsilon_A + 1/\varepsilon_B - 1}$$

where the view factor F and the emissivities ε_A and ε_B are defined by the user. While ε_A and ε_B are constant values, the view factor can be defined as a function of gap size as described in chapter 3.5.2.3. For the heat transfer analysis described in this chapter a constant view factor of $F = 1$ was set for all gap sizes. Hence the heat flux is only depending on surface temperatures θ_A and θ_B.

If these equations are compared to the ones behind the heat flux calculation of the fully implicit method one significant difference can be noticed. After equation (3.14)

$$q_i'' = \sigma\varepsilon_i \sum_{j=1}^{N} \varepsilon_j \sum_{k=1}^{N} F_{ik} C_{kj}^{-1}\left(\theta_j{}^4 - \theta_i{}^4\right)$$

the heat flux depends on the respective view factors and emissivities that are determined for every facet during the calculation of the radiosity matrix in the beginning of the analysis. In contrast to the surface normal radiation method the view factor and emissivity values are not equal for all facets. This fact can be regarded as one of the reasons for both the differing temperature distribution and the deviation in temperature level. The second one is that in the surface normal radiation method it is assumed that heat transfer happens only in normal direction to the respective facet. This assumption is also responsible for the observed deviations between the fully implicit and the surface normal radiation methods.

3.6.5 Comparing the fully implicit and the surface normal radiation methods

After the findings described in previous chapters two radiation models were considered as suitable for the heat transfer analysis of an air gap insulated exhaust manifold. The fully implicit and the surface normal radiation methods will be compared in detail in the following chapters

3.6.5.1 Comparison of energy balances

From the comparison of energy balances of the fully implicit and the surface normal radiation method it can be seen that the energy input and output for both models are equal, see Table 4.

Table 4: Energy balance of fully implicit and surface normal radiation method

	Heat flux across surface with fully implicit radiation method $[W]$	Heat flux across surface with surface normal radiation method $[W]$	Ratio
Surfaces to ambient	1105	1120	0.99
Exhaust pipe (gas side)	-1910	-1933	0.99
Exhaust ports	-3406	-3406	1.00
Exhaust pipe inner (air gap side)	1293	1316	0.98
Exhaust pipe outer (air gap side)	-1292	-1315	0.98
Oil jacket	769	768	1.00
Water jacket	3397	3395	1.00
BALANCE	**-44**	**-55**	**0.80**

A closer look at the energy balance of the air gap tells that the heat flow is represented correctly in the analysis model as the energy input across surface “Exhaust pipe inner” is equal to the energy output across the surface “Exhaust pipe outer”.

3.6.5.2 Comparison of temperature fields

From the direct comparison of temperature fields that are illustrated in Figure 45 and Figure 46 for the inner gas guiding pipes and in Figure 47 and Figure 48 for the outer pipe it can be seen that the temperature distribution is similar for both radiation methods. Only in regions where the geometry differs considerably from the ideal definition which is an annular gap between two concentric cylinders the temperature field differs slightly. The same can be said for the temperature level.

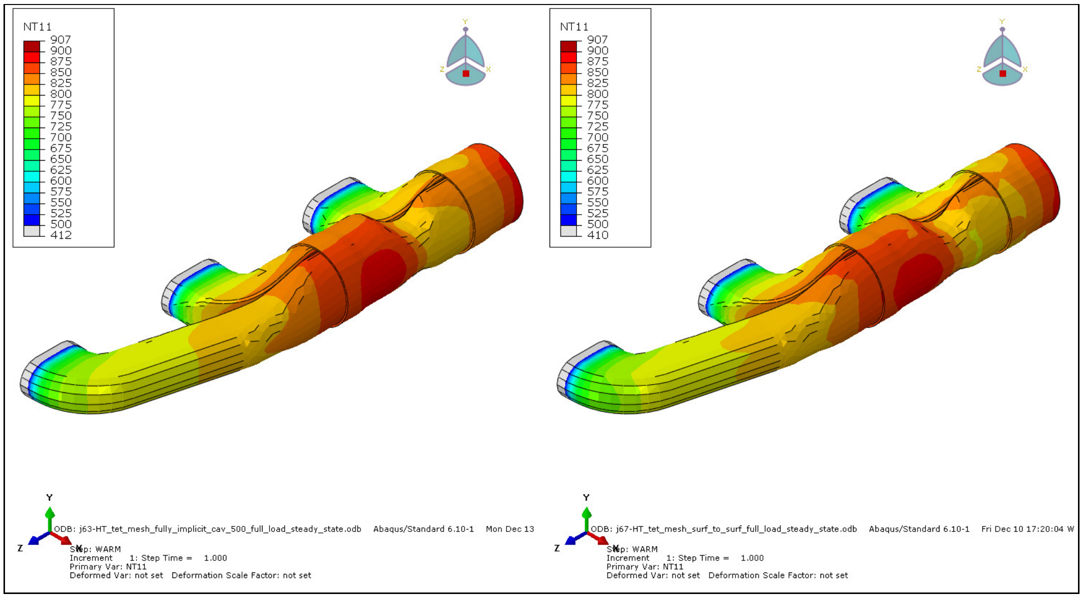

Figure 45: Temperature comparison of inner piping – fully implicit method (left), surface normal radiation method (right) – front view

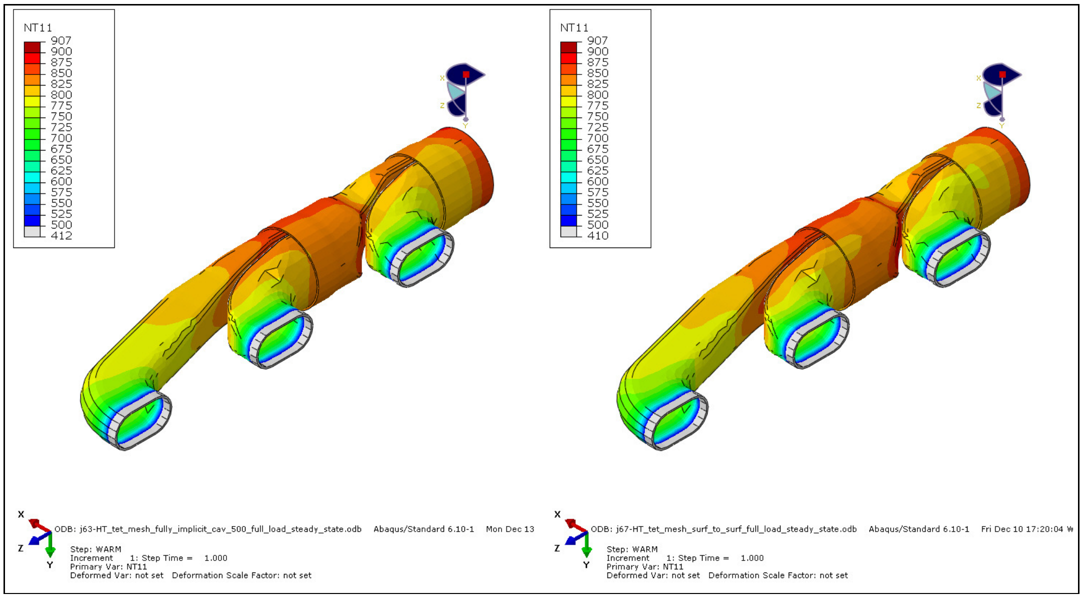

Figure 46: Temperature comparison of inner piping – fully implicit method (left), surface normal radiation method (right) – rear view

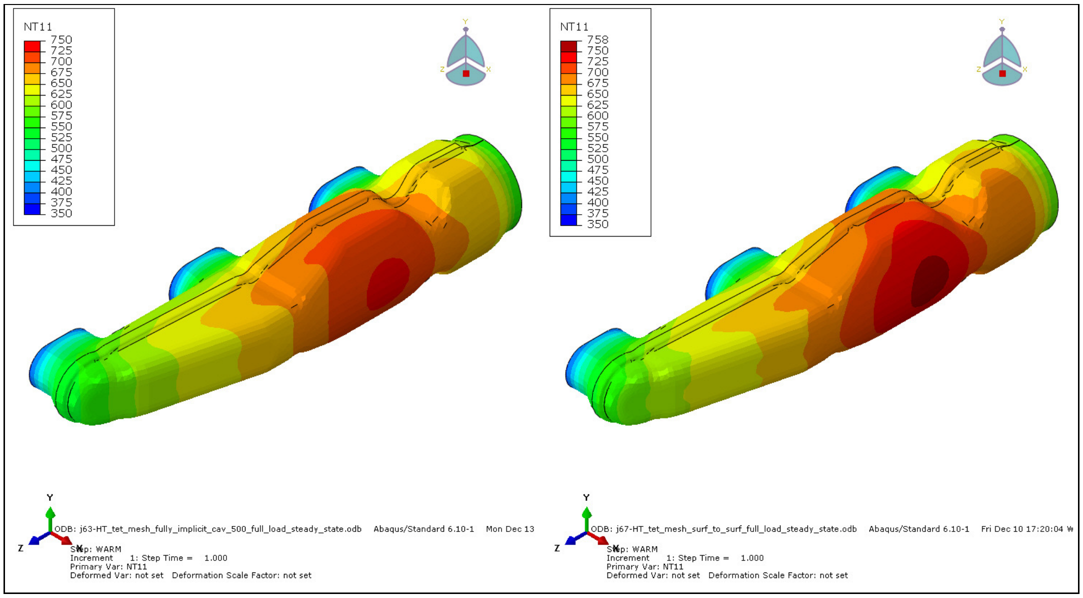

Figure 47: Temperature comparison of outer shell – fully implicit method (left), surface normal radiation method (right) – front view

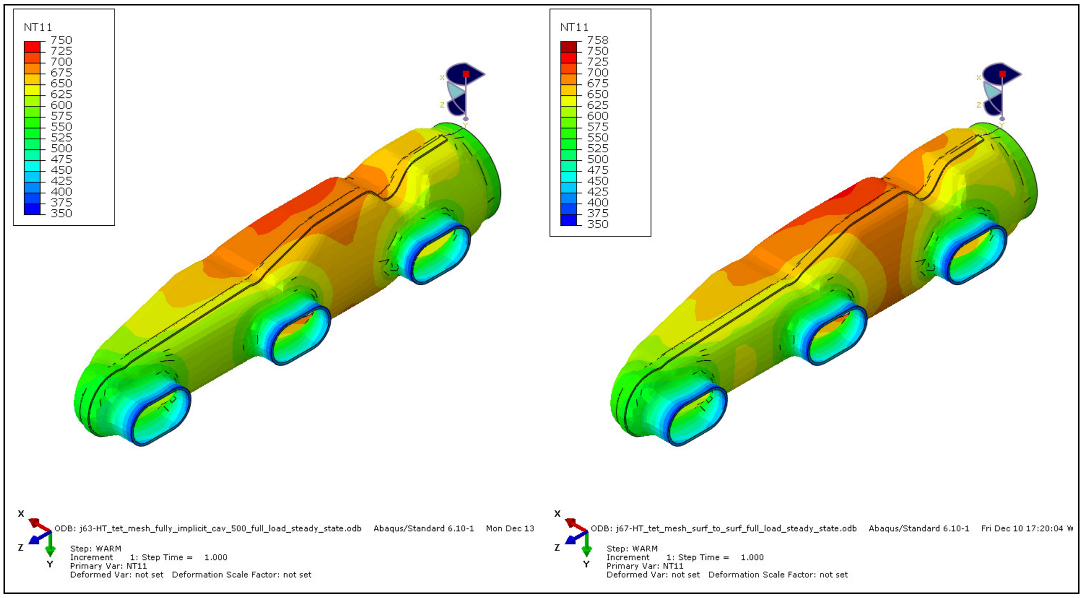

Figure 48: Temperature comparison of outer shell – fully implicit method (left), surface normal radiation method (right) – rear view

For giving a better overview on temperatures Table 5 lists the calculated temperatures for both heat transfer models at characteristic points. These points were chosen in respect to air gap size and can be seen on the piping in Figure 49 and for the cylinder head in Figure 50.

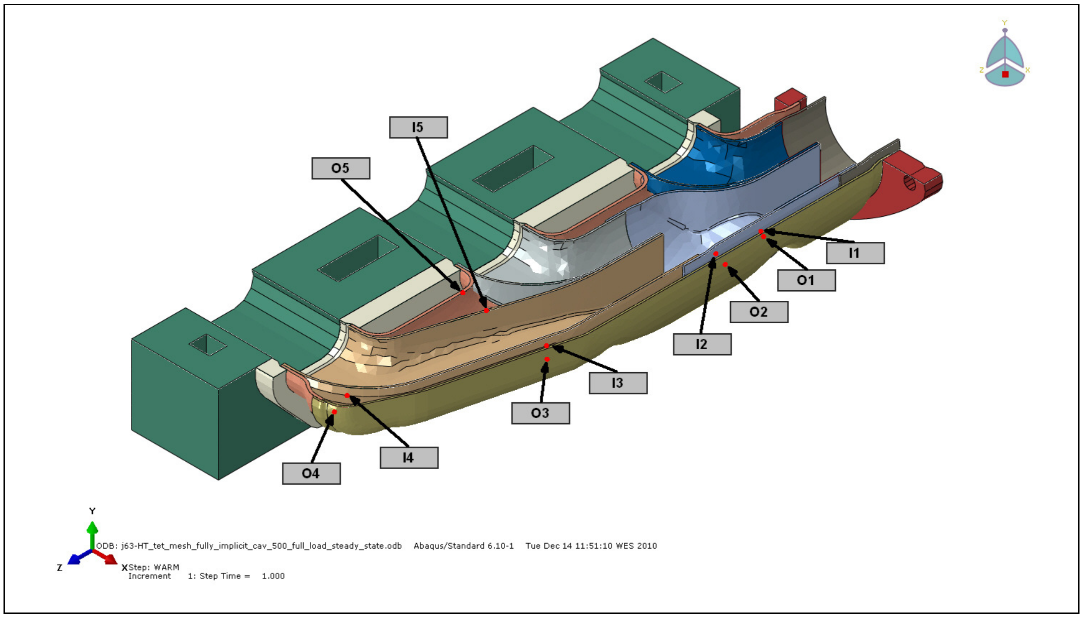

Figure 49: Measurement point overview on piping

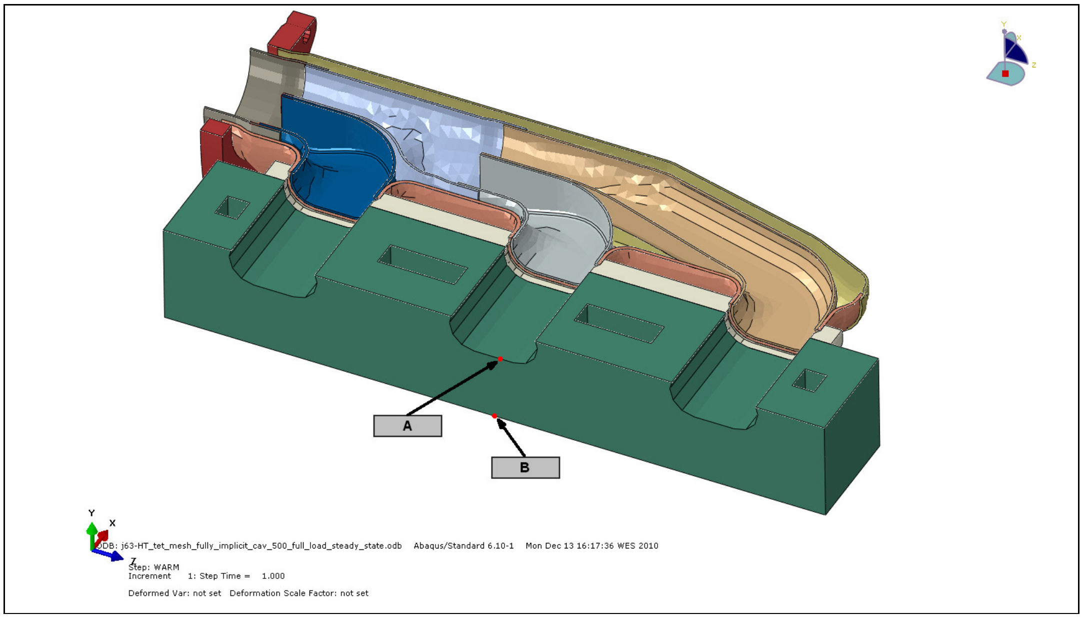

Figure 50: Measurement point overview on dummy cylinder head

Table 5: Comparison of steady-state nodal temperatures

Node	Air gap size $[mm]$	Steady-state nodal temperature with fully implicit radiation method $[°C]$	Steady-state nodal temperature with surface normal radiation method $[°C]$	ΔT
A	-	217.8	217.8	0
B	-	157.9	157.8	-0.1
O1	3.5	694.1	697.2	3.1
O2	6	731.4	757.6	26.2
O3	6	660.5	672.8	12.3
O4	12.5	545.2	568.5	23.3
O5	15	595	602.3	7.3
I1	3.5	815.9	820.3	4.4
I2	6	887.2	887.9	0.7
I3	6	813.7	813.5	-0.2
I4	12.5	767.2	737.3	-29.9
I5	15	800.7	786.1	-14.6

From Figure 51 it can be seen that for points $O1$ to $O5$ which are on the outer pipe the surface normal radiation method always delivers higher temperatures than the fully implicit method. On the inner pipes it can be observed that up to a gap size of $6\ mm$, which can be found at points $I1$ to $I3$, again the surface normal radiation method delivers higher temperatures. For points $I4$ and $I5$ where the air gap is larger than $6\ mm$ the fully implicit model delivers higher values. However no clear tendency can be found for the temperature difference ΔT between the fully implicit and the surface normal radiation method.

Despite the local temperature difference ΔT the global balance which is presented in Chapter 3.6.5.1 is equal. This indicates that the energy transferred is the same for both models. Only the local heat flux differs slightly.

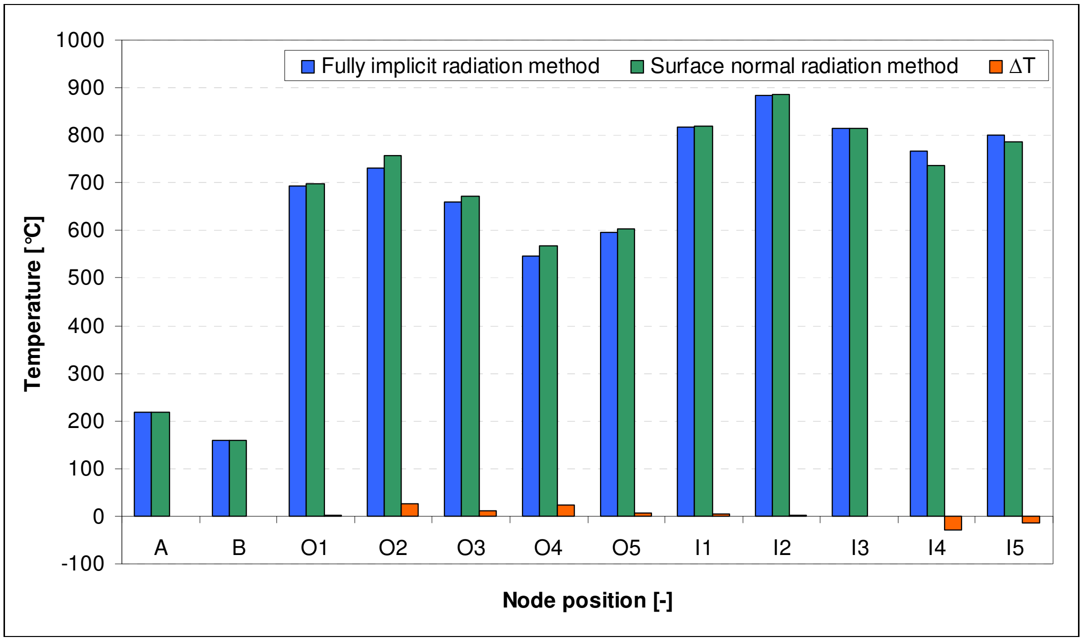

Figure 51: Temperature difference between the radiation methods

If the temperatures of the inner pipe are compared to those of the outer pipe and the temperature difference ΔT is calculated for points 1 to 5 as shown in Figure 52 (FI stands for results obtained with the fully implicit radiation method; SN is the synonym for the surface normal radiation method) it can be seen that independent of the size of the air gap the surface normal radiation method delivers always a minor ΔT. However no clear trend can be found for the gradient of ΔT. This means that no clear statement can be made about the level of ΔT for a certain gap size. Again this proves that the temperature field calculated with both radiation methods highly depends on geometry and that even a slight deviance can lead to different temperature results, hence it is difficult to define exact trends that could describe the behavior of the radiation methods presented.

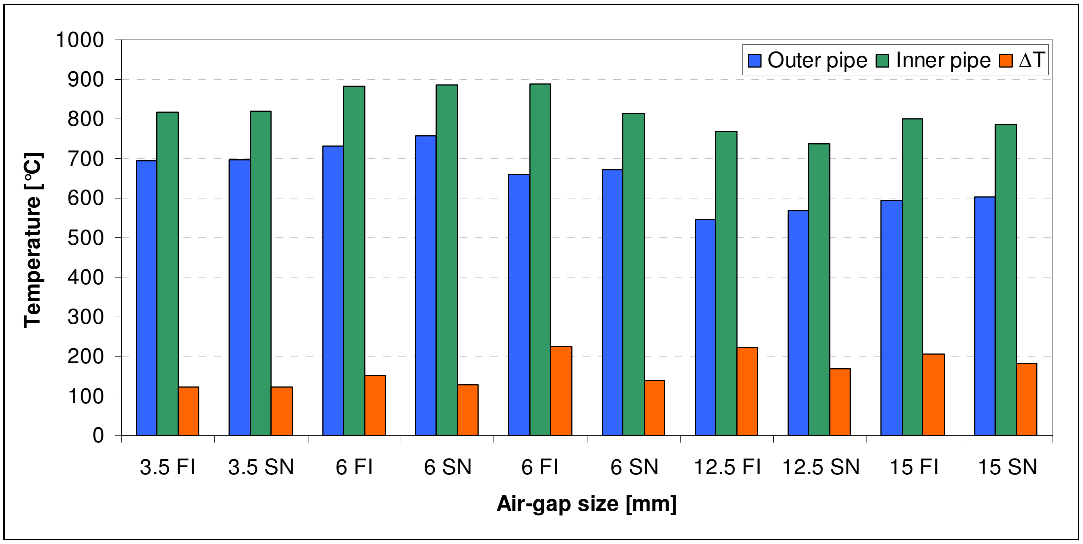

Figure 52: Temperature difference between inner and outer pipe related to air gap size

3.6.5.3 Comparison of computational costs

An important aspect in FE analysis is the computational cost of an analysis. Table 6 shows a comparison of steady-state computational costs between the fully implicit and the surface normal radiation method.

Table 6: Computational costs of steady-state heat transfer analysis

	Fully implicit radiation method; steady-state	Surface normal radiation method; steady-state	Ratio
CPU time $[\sec]$	3266	60	54
Wallclock time $[\sec]$	3268	61	54
Increments	1	1	1
Iterations	5	8	0.6
Wallclock time per iteration $[\sec]$	653.6	7.6	86
Minimum memory required $[MB]$	2311	100	23
Memory to minimize I/O $[MB]$	3520	195	18

It can be seen that the wallclock time, which stands for the effective analysis time is 54 times higher for the fully implicit method. This is because the method requires the time consuming computation of a radiosity matrix as explained in Chapter 3.5.2.1. Therefore it can be said that the required time for a transient heat transfer analysis is expected to be considerably higher. Table 7 exemplary shows a comparison of the computational costs of a transient exhaust manifold analysis.

Table 7: Computational costs of fully implicit and surface normal radiation method – transient (2 cycles)

	Fully implicit radiation method; transient	Surface normal radiation method; transient	Ratio
CPU time [sec]	25200	1533	16
Wallclock time [sec]	25211	1536	16
Increments	75	77	1
Iterations	152	200	0.8
Wallclock time per iteration [sec]	165.9	7.7	22
Minimum memory required [MB]	3069	109	28
Memory to minimize I/O [MB]	4333	195	22

It can be seen that the time needed for an analysis with the fully implicit radiation method is 7 hours compared to 26 minutes with the surface normal radiation method. If the iterative procedure in transient heat transfer analysis, which will be explained in detail in Chapter 3.7.1 is considered, a total processing time of approximately two or three working days can be estimated.

The amount of required memory is another significant factor that should be mentioned. This is because in contrast to the surface normal radiation method the fully implicit method needs to handle the radiosity matrix, which has N^2 entries (see Chapter 3.5.1) and is therefore very large and requires significantly more memory.

3.7 Transient heat transfer analysis

After the inquiry on steady-state heat transfer a transient simulation of the dual-walled exhaust manifold was performed to get the time dependent temperature field that serves as thermal load input in strength analysis.

3.7.1 Definition of transient heat transfer cycle

The transient heat transfer cycle is defined in respect to AVL standard procedure for exhaust manifold analysis. To reduce calculation time the original cycle that consists of multiple cooling phases that can be found in AVL iCAE [2010] was simplified. Note that this has only little effect on the accuracy of the analysis and results can be regarded as comparable to those achieved from the original cycle. Figure 53 shows the simplified thermal load cycle used for the transient heat transfer analysis.

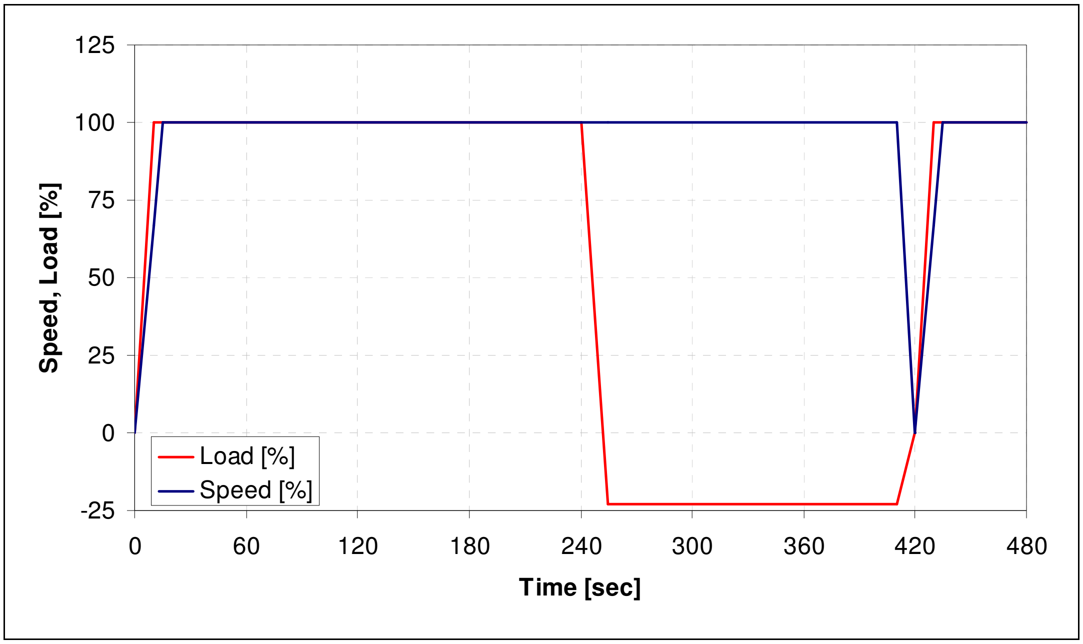

Figure 53: Simplified thermal load cycle

Two load points were taken into account for the cycle. The first one is full load condition where the highest exhaust gas flow rates and temperatures can be observed. The second one represents the coasting mode – also referred to as "motored" load condition – where no fuel injection, thus no combustion takes place but the engine is still running at rated speed. This load point is relevant because of its cooling effect. Since no combustion takes place exhaust gas temperatures are low as the gas is only heated by combustion chamber walls. In combination with a high gas flow rate that occurs at rated speed the exhaust gas provides excellent cooling of the exhaust manifold. The rapid change of temperatures between these two conditions is regarded to be the most critical for exhaust manifolds in terms of durability.

The cycle times are determined iteratively. In the AVL standard methodology holding times are based on the time needed to achieve full stabilization of the metal temperature at the cylinder head exhaust valve bridge. Because the model used for the temperature field analysis does not contain the exhaust valve bridge the exhaust port temperature of the cylinder head is considered as reference. Curve A in Figure 54 and Figure 55 shows the exhaust ports temperature history. Temperature stabilization takes place when the exhaust port temperature reaches $90-95\ \%$ of steady state temperature. This criterion is fulfilled after 240 seconds in the heating up phase and after 180 seconds in the cooling down phase.

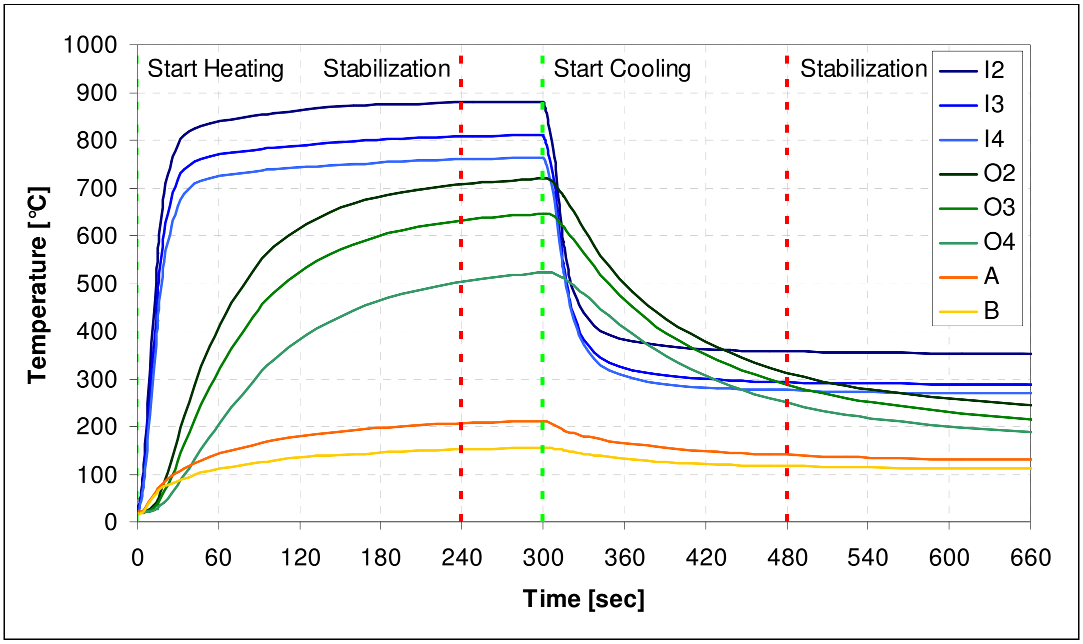

Figure 54: Temperature history obtained with the fully implicit radiation method

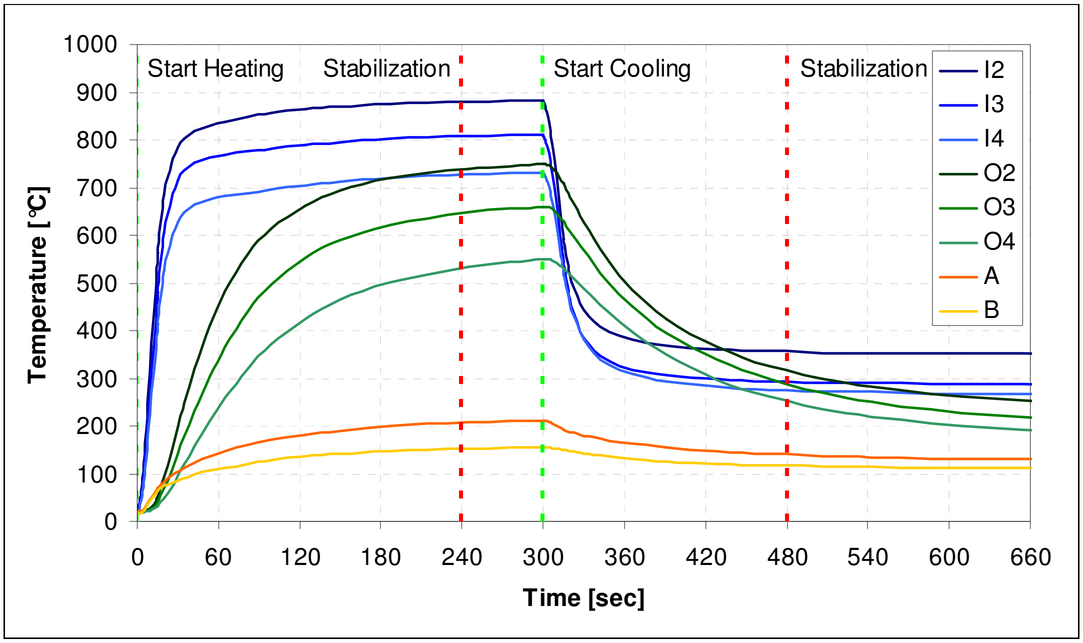

Figure 55: Temperature history obtained with the surface normal radiation method

Additionally Figure 56 shows the direct comparison between the temperature histories of points $I2$, $O2$ and A obtained with the fully implicit and the surface normal radiation method. It can be seen that the temperatures for points $I2$ and A correspond well, hence no remarkable difference can be observed. Curve $O2$ shows a slight difference in temperatures, which is around $3\ \%$. This deviation was already discussed in Chapter 3.6.5 and will not be repeated at this point. Concerning the holding times no differences can be observed as both curves A are identical. Therefore in this case the determined holding times are valid for both heat transfer methods.

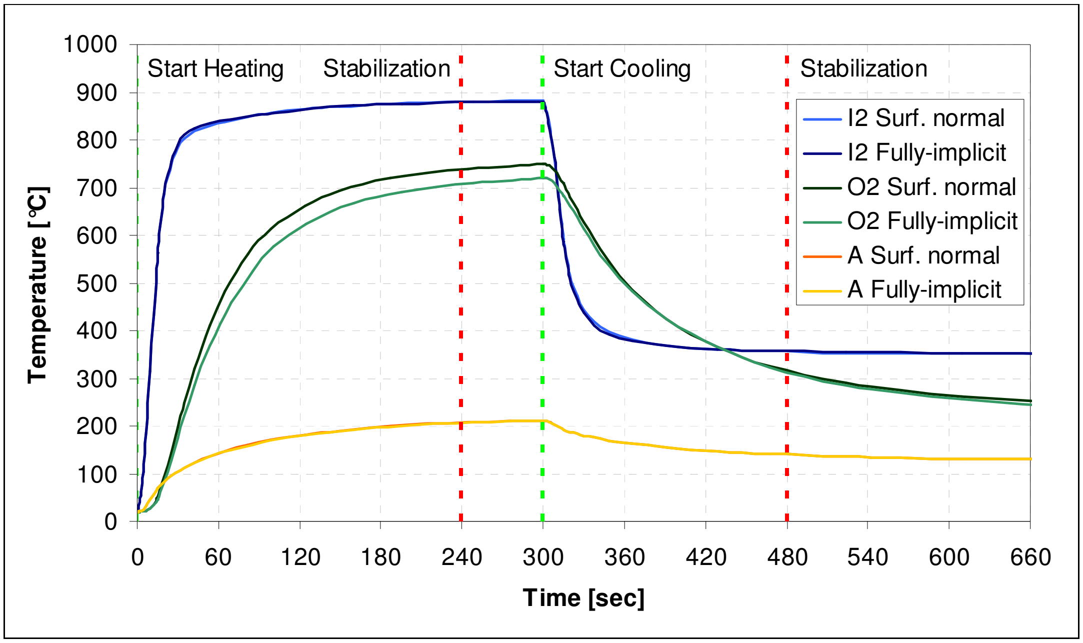

Figure 56: Temperature history comparison

After determining the holding times a second transient heat transfer analysis loop was performed. Thereby two cycles were calculated as only the second cycle is considered to be fully stabilized. The temperature history can be seen in Figure 57 for the fully implicit and in Figure 58 for the surface normal radiation method.

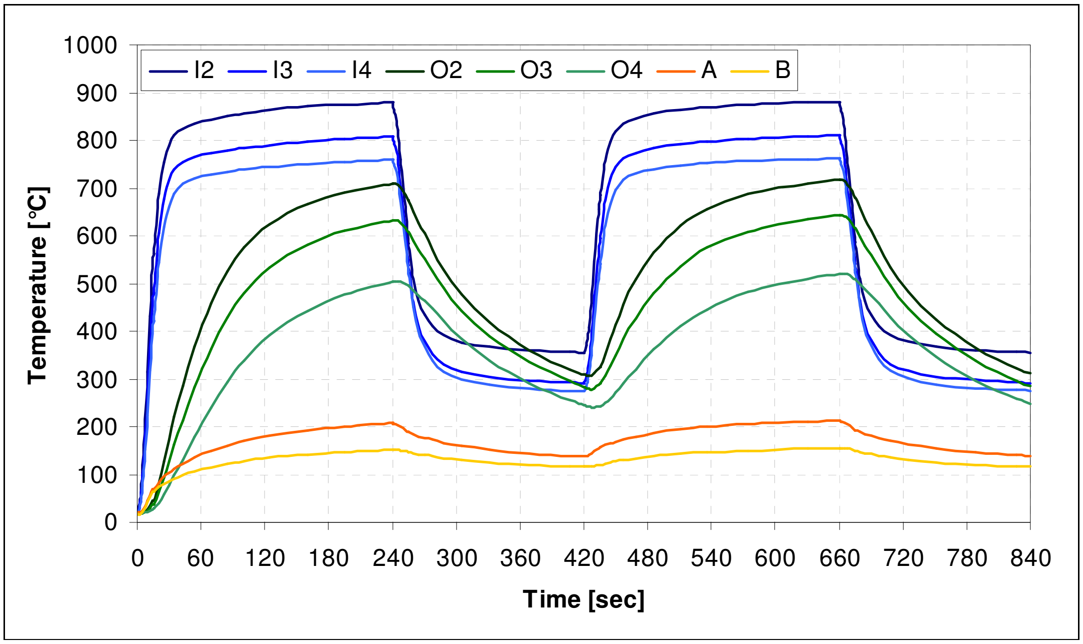

Figure 57: Temperature history determined with the fully implicit radiation method – 2 cycles

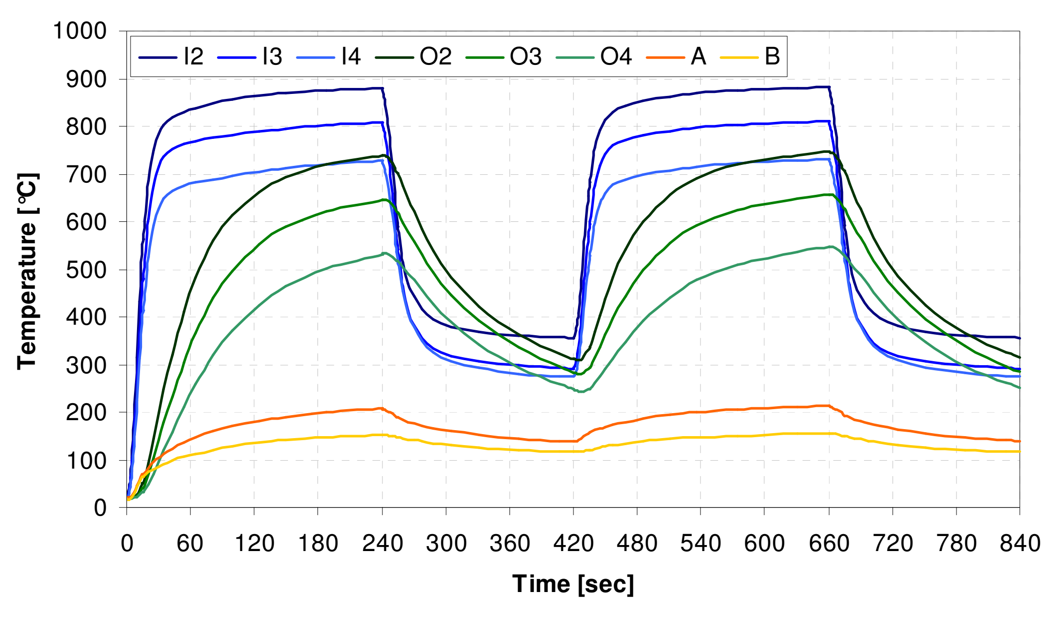

Figure 58: Temperature history determined with the surface normal radiation method – 2 cycles

The temperatures determined hereby will be used for the strength analysis described in Chapter 4.

3.8 Conclusions about heat transfer analysis

During the research on heat transfer phenomena that occur in air gap insulated exhaust manifolds it was proven that only heat transfer due to conduction and radiation have to be considered. In terms of radiation two methods turned out to be suitable for the simulation of heat transfer over an annular gap between concentric cylinders. These are the computation cost intensive fully implicit radiation method and the 54 times faster surface normal radiation method. The parity of these methods was proven with the help of energy balances and the similar temperature fields obtained. Although some trends concerning the temperature behavior over air gap size can be observed no clear tendency could be found for the radiation methods relative behavior. However it can be said that with the surface normal radiation method smaller temperature differences are calculated between the inner and outer pipe at all time. This indicates that a smaller relative deformation between inner and outer pipe can be expected in strength analysis as the temperature difference between the pipes is smaller in the surface normal radiation method.

Based on the observations described in the previous chapters the usage of the surface normal radiation method is recommended for the heat transfer analysis of dual-wall air gap insulated exhaust manifolds. The main criterion therefore is the small difference in temperature field distribution and temperature level, which is up to $5\ \%$ compared to the exact fully implicit radiation method. But the advantage in computational time and the possibility for defining unlimited number of radiation exchanging facets are determining factors as well.

Additionally it has to be said that for very complex shapes the surface normal radiation method might not meet the requirements, hence the fully implicit radiation method has to be used. Since this topic was not investigated in detail further research is required to obtain clear statements.

3.9 Summary of required heat transfer analysis boundary conditions

The following chapter gives a short overview of the boundary conditions to use during the heat transfer simulation process of dual-walled air gap insulated exhaust manifolds.

Table 8 lists the surface-to-surface interaction definitions for gap radiation and gap conductance.

Table 8: Surface-to-surface interaction definitions in ABAQUS/Standard representing gap conduction and gap radiation

Interaction name	Master	Slave	Tang. behav.	Normal behav.	Type	Gap conductance	Gap radiation
airgap-cond	Inner pipes	Outer pipes	-	-	s2s	Appendix A.3	-
airgaprad	Inner pipes	Outer pipes	-	-	s2s	-	Appendix A.4

The interaction properties for convective and radiation heat transfer to ambient are listed in Table 9.

Table 9: Interaction definitions in ABAQUS/Standard representing convection and radiation to ambient

Interaction name	Interaction type	Surface	Properties
conv2amb	Surface film condition	Ambient surfaces	$T = 75\ °C$; $HTC = 15E-06\ W/mm^2 \cdot K$
rad2amb	Surface radiation	Ambient surfaces	To ambient; $T = 30\ °C$; $\varepsilon = 0.2$

All other boundaries and interactions are based on AVL standard methodology and are therefore not explained in further detail.

4 Strength analysis

After gaining the results from the transient heat transfer analysis a non-linear strength analysis was performed to visualize the deformation behavior of the air gap insulated exhaust manifold. The observations made during the analysis should be discussed in the following chapter.

4.1 Analysis model

For the strength analysis a 3D FEM model was used that consists of the same parts as the heat transfer analysis model described in Chapter 3.6.1. Only six M8 bolts were added in order to be able to consider also the stresses and strains that occur because of the bolt tightening procedure during the assembling of the exhaust system. Figure 59 shows the analysis model used for the strength analysis.

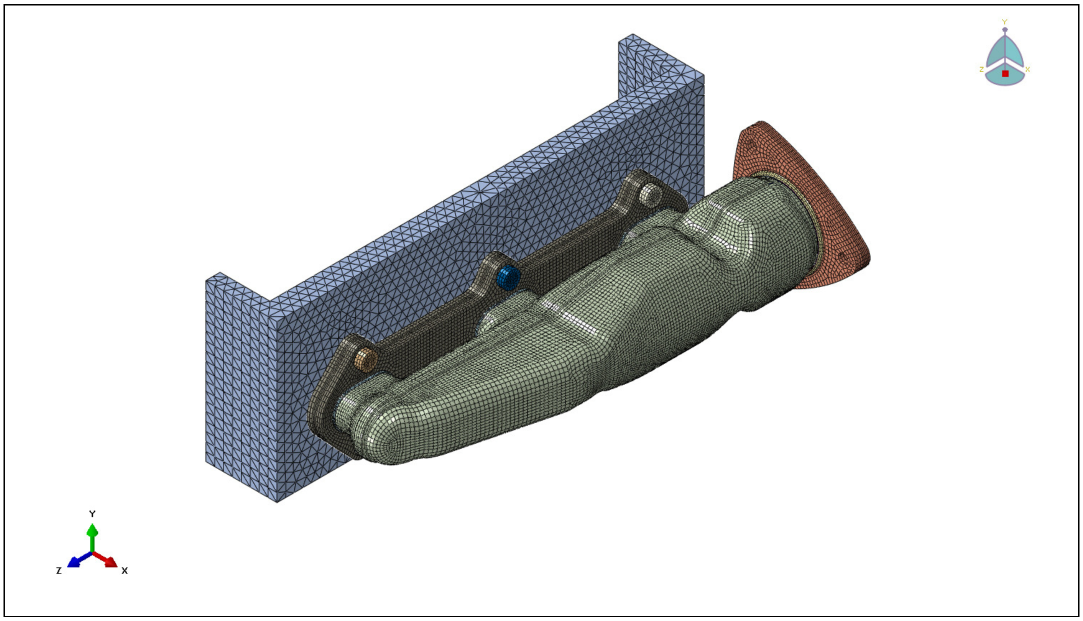

Figure 59: ABAQUS/Standard 3D FEM model for strength analysis

It can be seen that in contrast to the heat transfer model linear hexahedral elements of type C3D8R were used for modeling the flanges, bolts and some parts of the piping and that quadratic quadrilateral elements of type S8R were used for modeling the main parts of the piping. These changes were done primarily to save computational costs.

A further topic of interest was to inquire whether the results of a heat transfer model, where tetrahedral elements were used, can be used as load input in a strength analysis model with quadrilateral elements. During the analysis process this was proven to be possible and can be recommended for prospective customer projects because of the high computational time saving potential of the analysis technique.

4.1.1 Interaction properties and boundary conditions

All contacts were modeled either with friction contacts or tie contacts depending on the way of assembling.

4.1.2 Load definition

The strength analysis starts with the assembly load (bolt pre-load) followed by consecutive transient temperature fields combined with gas pressure loads simulating several thermal loading cycles.

For determining all relevant stress conditions the definitions of the load shown in Figure 60 were chosen from the transient heat transfer analysis as input for the strength analysis.

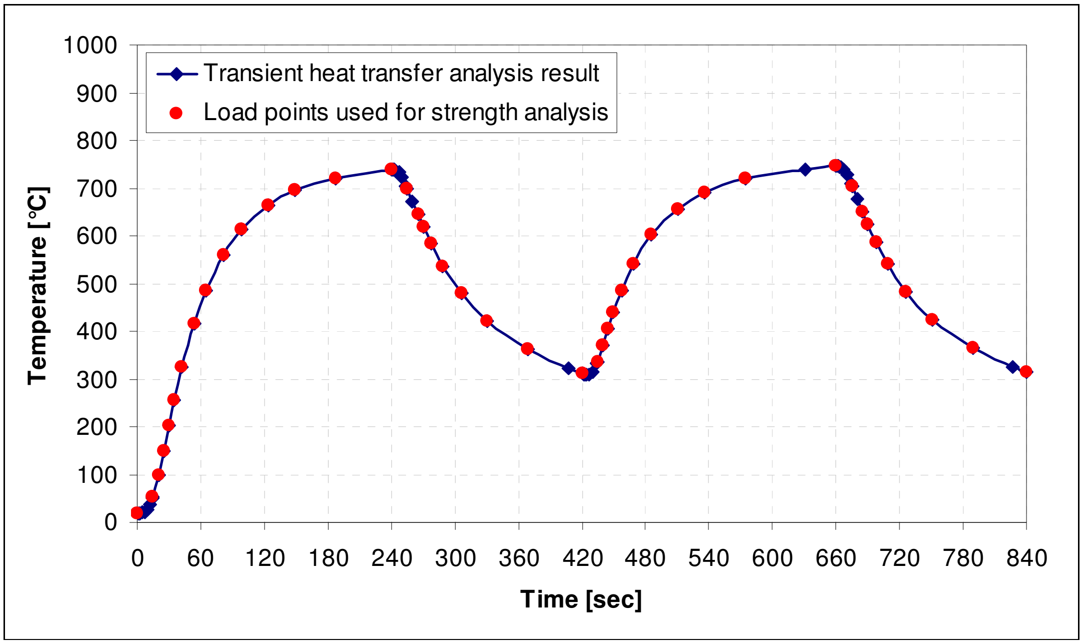

Figure 60: Load points for strength analysis

The points shown in red color were chosen according to the criterion that the temperature difference between two points should be approximately $50\ °C$. This guarantees that the thermal behavior of the exhaust manifold is represented sufficiently in the strength analysis. As only the third cycle is regarded as fully stabilized in terms of stress condition and viscoeleastic effects the second cycle from Figure 60 is duplicated for the strength analysis.

Table 10 gives an overview of the load combinations used for the strength analysis.

Table 10: Load combinations

Load history	Ass	1st cycle		2nd cycle		3rd cycle	
Basic Load	LC0	LC1	LC2	LC4	LC5	LC7	LC8
Assembly load	+	+	+	+	+	+	+
Thermal load - full load		+		+		+	
Thermal load - motored			+		+		+
Gas load - full load		+		+		+	
Gas load - motored			+		+		+

4.1.3 Notes on weld modeling

As the usage of weld joints in air gap insulated exhaust manifolds is inevitable the recommended finite element modeling technique will be described briefly in the following.

The red colored element sets in Figure 61 show the recommended finite element modeling technique for weld joints.

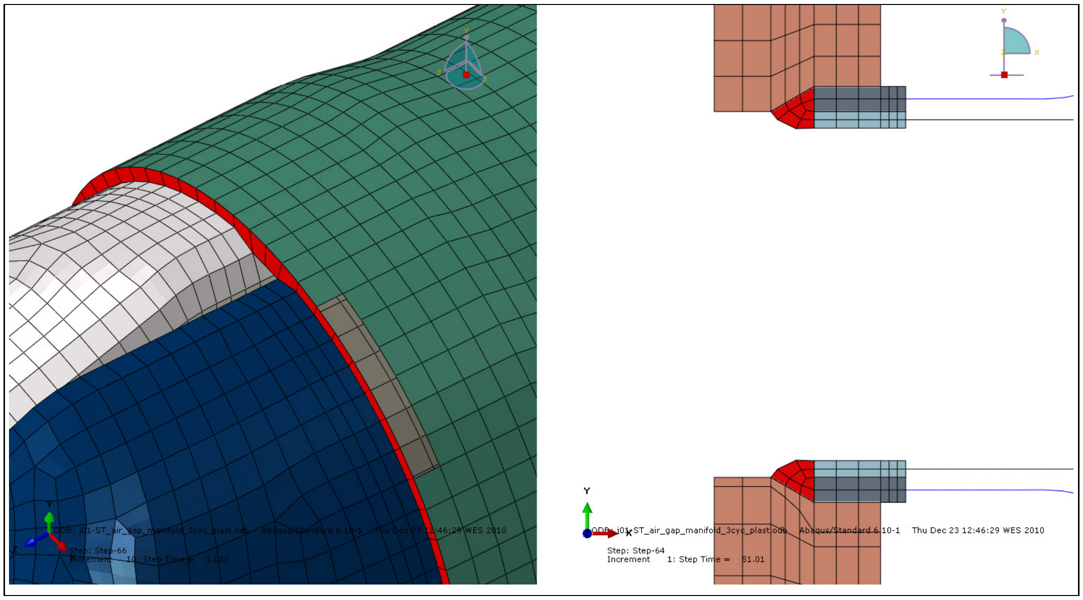

Figure 61: Finite element weld joint modeling – left: shell elements; right: continuum elements

The left hand side describes the recommendation for modeling with shell elements. It can be seen that one circumferential row of shell elements in normal direction to the adjacent elements represents the weld joint. The shell has to be as thick as the parts that it will be connected to by the weld joint. In case of different wall thicknesses the value of the major material thickness has to be used. Thereby the middle plane of the shell element has to be selected for the definition of the property of the material. Finally the element set representing the weld joint has to be merged with the neighboring parts.

On the right hand side of Figure 61 the modeling recommendation for continuum element weld joints is presented. The joint has to be modeled in imitation to the real joint. Note that the mesh has to be fine enough for further evaluation. Therefore at least three elements have to be defined on the edges of the contact surface. The connection to all adjacent parts is represented by tie constraints.

4.2 Simulation results

In the following chapters the results of the strength analysis will be presented. Thereby a special focus is set on global exhaust manifold displacements, plastic deformation and the discussion of modeling problems.

4.2.1 Global exhaust manifold deformation

Due to the exposure of the exhaust manifold to high temperature differences that occur during the cycles described in Chapter 4.1.2 a fairly large deformation can be observed. Figure 62 shows the global deformation of the exhaust manifold under peak temperature load. It can be seen that Pipe-1 and Pipe-2 move back and forth at the sliding fit area at Pipe-3, see red arrows. Thereby the largest displacement occurs at point A located on Pipe-1.

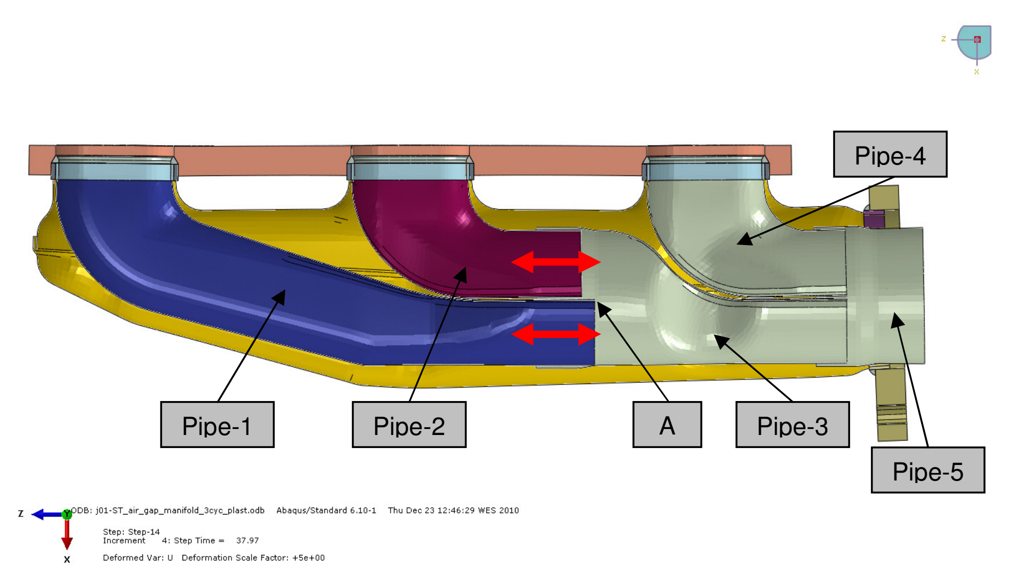

Figure 62: Global deformation of the exhaust manifold – horizontal cut (scale factor 5)

To provide with a better idea on the quantity of the displacement Figure 63 shows the displacement magnitude and its specific components $(U1, U2, U3)$ at this point. The algebraic prefix is determined by the orientation of the coordinate system and therefore has no specific meaning.

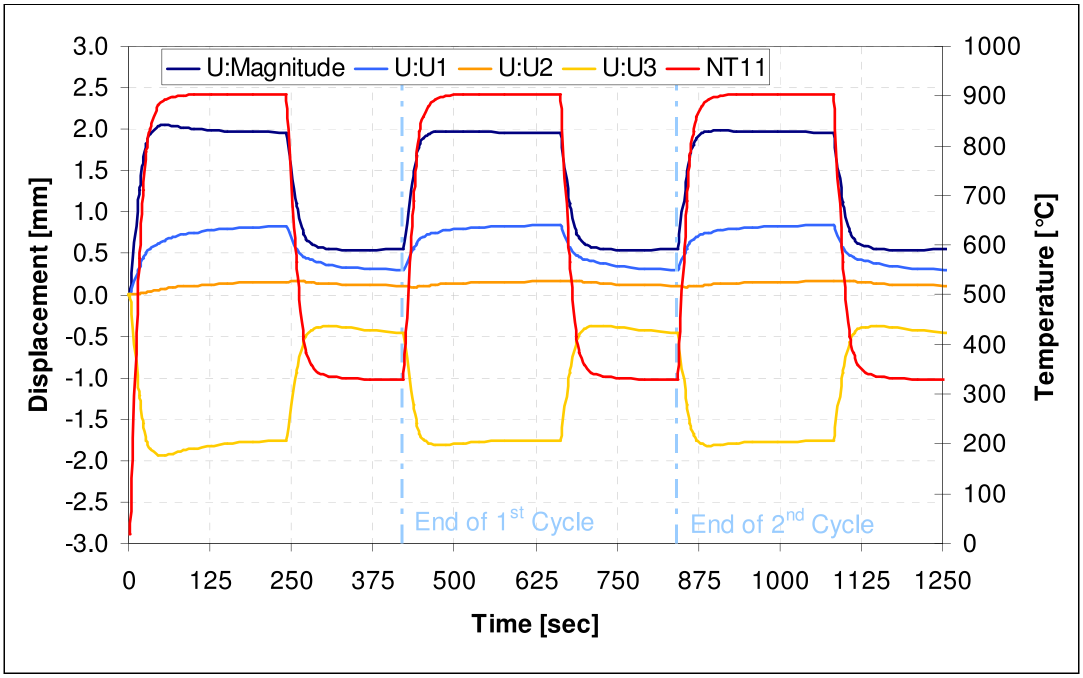

Figure 63: Displacement at point A over analysis cycle

The highest deformation magnitude occurs during the first heating-up phase and is $2.04\ mm$. It is particularly noticeable that the highest deformation does not correspond with the point of maximum temperature. At this point in time the displacement already decreases. To avoid the formation of thermal stresses the sliding fit in Pipe-3 has to provide sufficient space for the elongation of Pipe-1.

For better visualization of the overall deformation Figure 64 shows a contour plot of the exhaust manifold cut in the horizontal middle plane at the time of maximum displacement of point A. The blue contours display the undeformed plot state and the red ones the deformed with a scale factor of two.

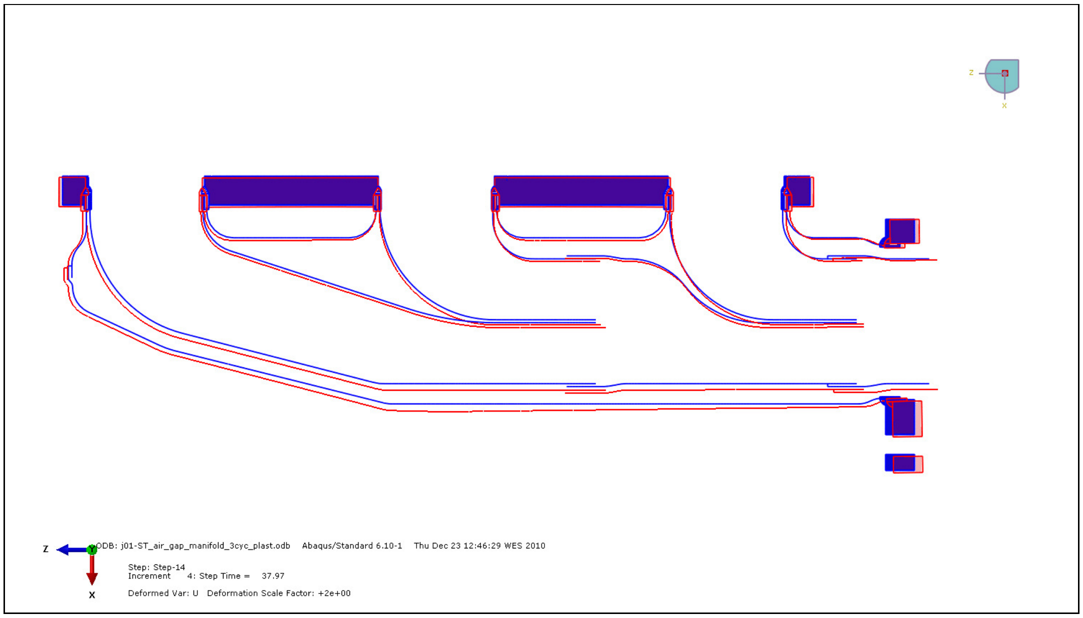

Figure 64: Exhaust manifold deformation under peak thermal load – horizontal cut (blue: undeformed plot state; red: deformed plot state (scale factor 2))

4.2.2 Deformation after disassembly

The critical issues in terms of the deformation on the exhaust manifold are remaining stresses after the disassembling of the manifold. These can lead to permanent deformations of the manifold, hence a reassembly can become impossible. In order to detect such deformations a simulation was performed where the exhaust manifold after thermal cycling was first cooled down to room temperature ($T = 20\ °C$) and secondly the mounting bolts were released.

Table 11 lists the relative flange displacements in $U1$ direction that can be seen in Figure 65. It can be said that permanent deformations in this range can be considered as negligible and do not cause problems during reassembly as they can be easily compensated by the bolt tightening force.

Table 11: Relative flange displacement in $U1$

Position	Relative displacement from port B $[mm]$
A	0.126
C	0.094

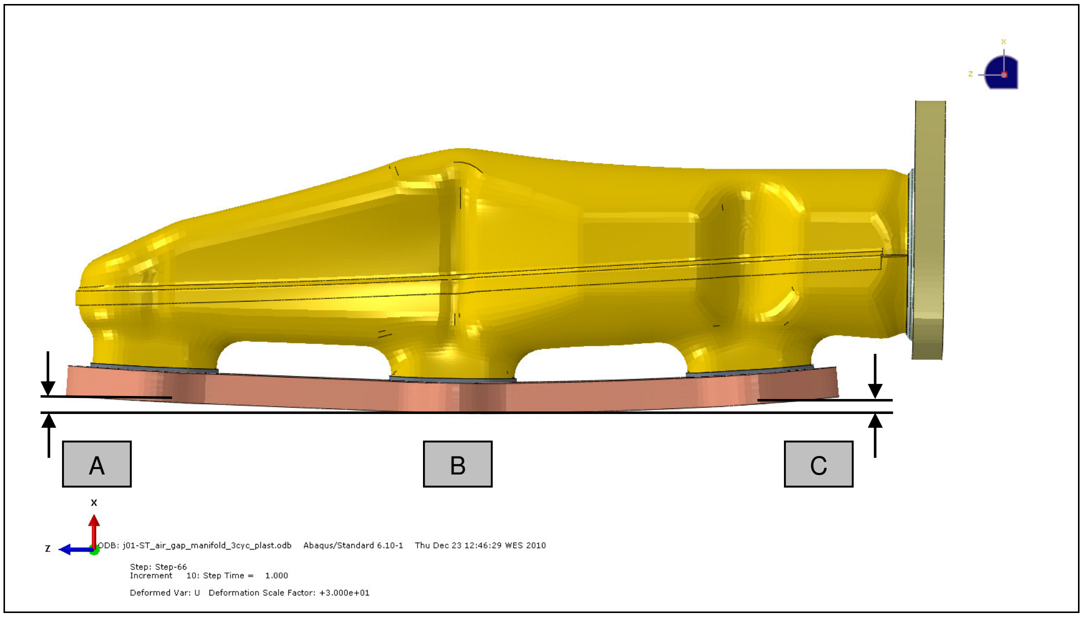

Figure 65: Relative flange displacement in $U1$ after cooling to room temperature and disassembly (scale factor 30)

The same applies for the relative flange displacement in $U3$ direction. These are listed in Table 12 and can be seen in Figure 66.

Table 12: Relative flange displacement $U3$

Position	Before assembly $[mm]$	After disassembly $[mm]$	Difference $[mm]$
D	100.000	100.004	0.004
E	100.000	100.009	0.009

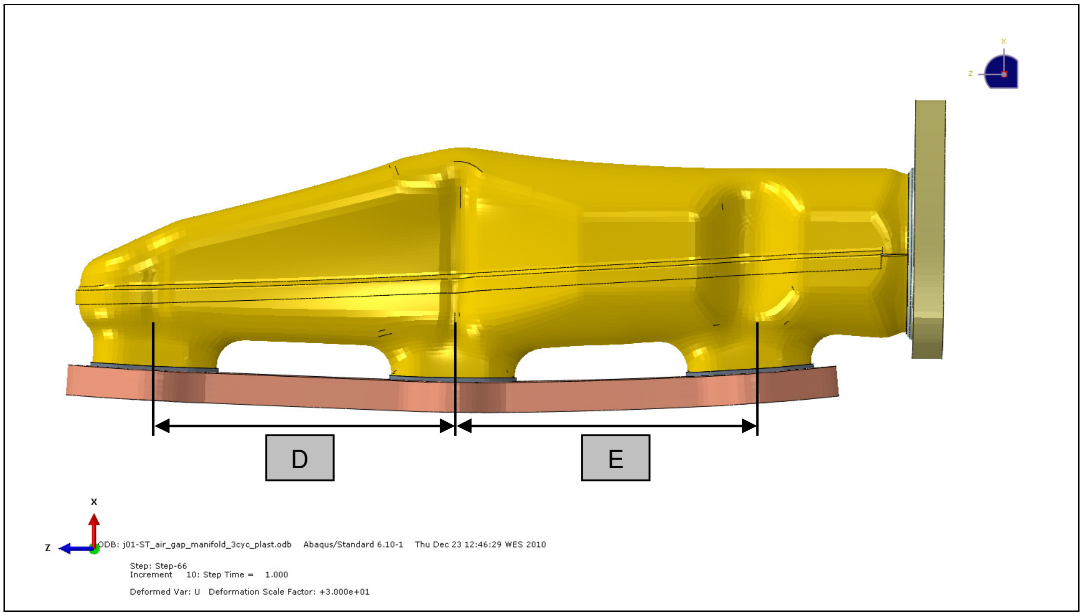

Figure 66: Relative flange displacement in $U3$ after cooling to room temperature and disassembly (scale factor 30)

4.2.3 Stresses and plastic deformation

Stresses depend on exhaust manifold geometry, applied materials, loads due to assembly and thermo-mechanical loads. They are a measure for the operational demands and for the ability of the material to cope with these, hence they play a vital role in fatigue analysis and are therefore determinant for the durability of the manifold.

The stresses that result from the loading described in Chapter 4.1.2 are displayed in Figure 67 and Figure 68. It can be seen that the von Mises stresses are mainly in the range up to $250\ MPa$ which can be regarded as uncritical. These occur mainly on the outer piping of the exhaust manifold and are caused by the restraining of the part at the exhaust ports. The inner piping which comes with a sliding fit mainly shows a stress level that is under $50\ MPa$. This is because of the ability of the sliding fit to avoid the formation of thermal stresses.

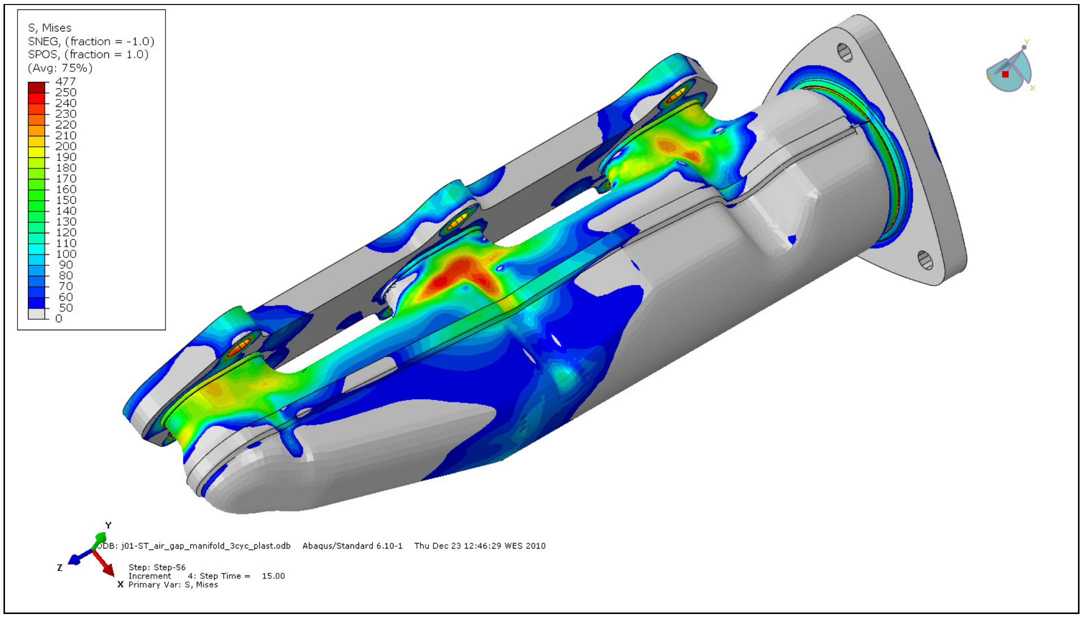

Figure 67: von Mises stresses on exhaust manifold

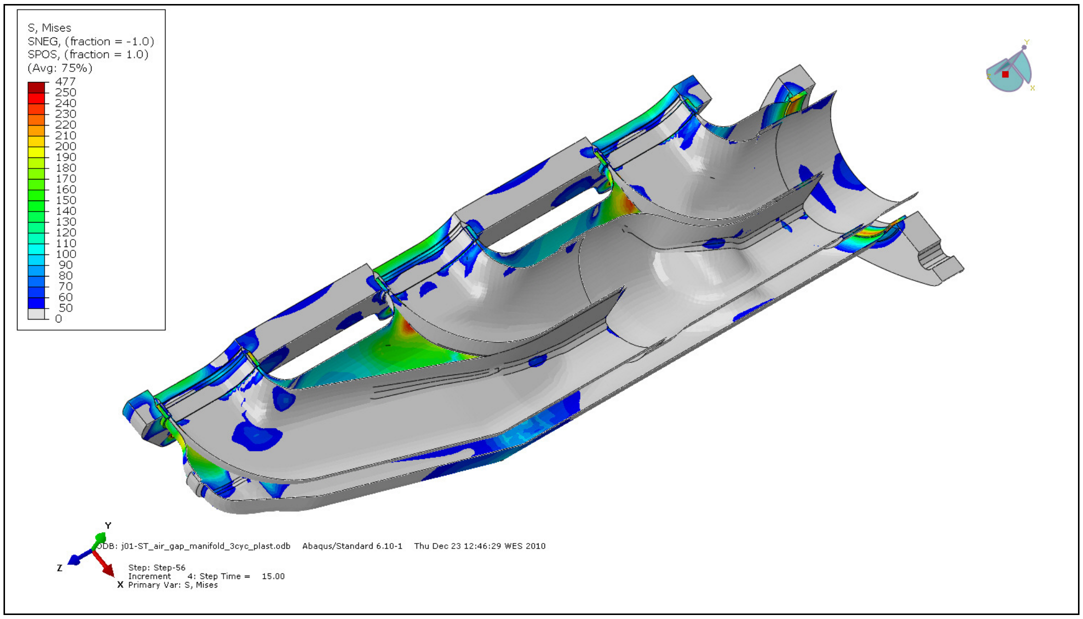

Figure 68: von Mises stresses exhaust manifold – horizontal cut

However von Mises stresses up to $477\ MPa$ can be observed in the areas where so called “shell to solid” couplings are applied. These serve as connector between continuum and shell elements. Because these stress peaks are considered to be physically incorrect a detailed inquiry of these areas was performed using a suitable FE submodel, see Chapter 4.2.5.

Another criterion for evaluating damage due to thermo-mechanical loading is the equivalent plastic strain (PEEQ). PEEQ is the equivalent plastic strain in uniaxial compression, similar to what von Mises is to stresses. It is a scalar measure of all the equivalent plastic strain components and is defined as

$$\int \dot{\bar{\varepsilon}}_C^{pl} dt \tag{4.1}$$

where $\dot{\bar{\varepsilon}}^{pl}$ is the equivalent plastic strain rate which can be calculated after several models depending on the materials used and on the loads applied [Simulia Inc. 2010].

Figure 69 and Figure 70 show the PEEQ on the inner and outer piping of the exhaust manifold after the last analysis step which is the disassembly. It can be seen that an equivalent plastic strain of $1.27\ \%$ at point A and $4.48\ \%$ at point B is reached after the thermo-mechanical cycling and the disassembly. Because of the lack of advanced material data no exact material limit can be specified for the materials used. However the PEEQ limit of similar materials is around $2\ \%$ [AVL iCAE 2010] which was exceeded during this analysis, hence crack formation occurs at some points and leads to malfunction of the exhaust manifold. Therefore in case of a customer project a design modification is compulsory to guarantee adequate life time.

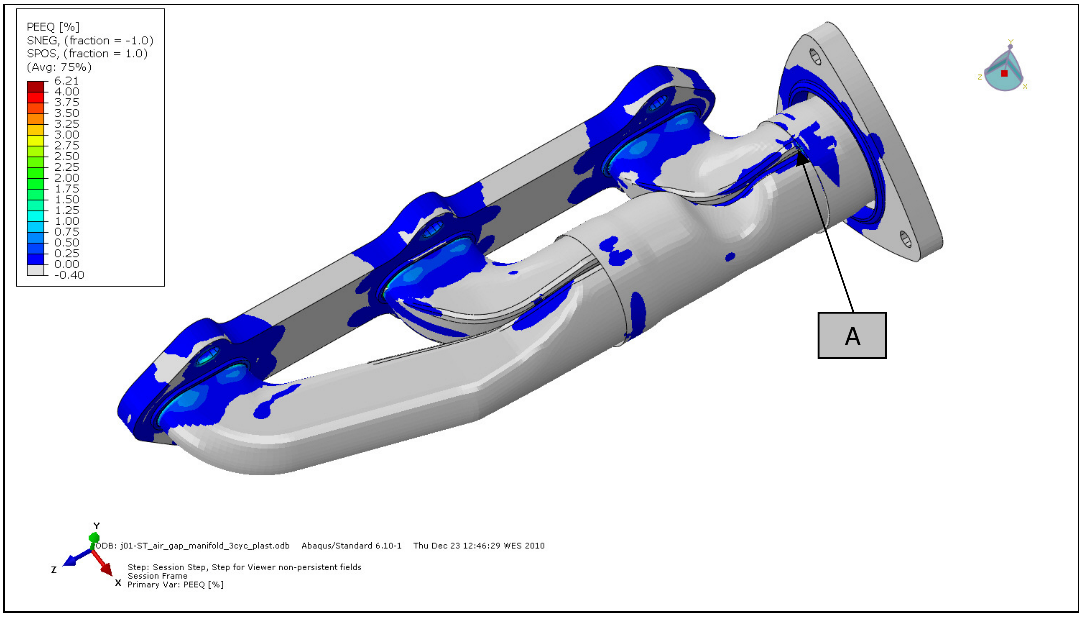

Figure 69: Equivalent plastic strain (PEEQ) on exhaust manifold inner piping

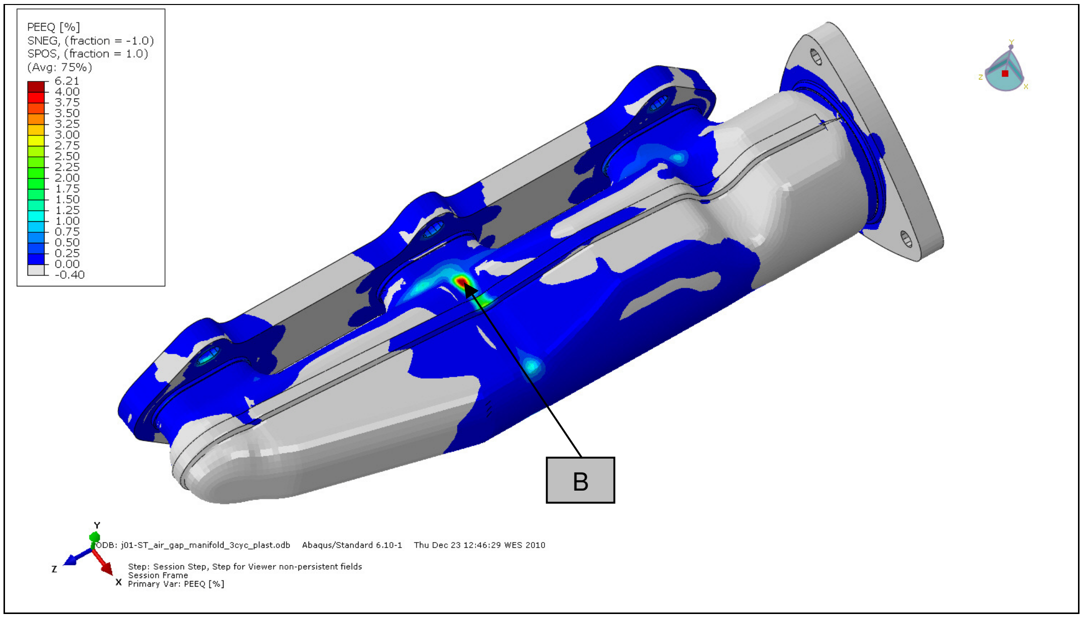

Figure 70: Equivalent plastic strain (PEEQ) on exhaust manifold outer piping

To give a better understanding about the formation of stresses and plastic deformation a detailed evaluation was performed for point A on the exhaust manifold. The point was chosen because of its PEEQ level which is more a concern in terms of durability than stresses that are above all very low.

4.2.4 Detailed stress evaluation for point A on the inner piping

Figure 71 shows the stress and temperature history for point A. The principal stresses $S11$ and $S22$ are displayed over the analysis time for two integration points – $SP:1$ and $SP:5$ – of the respective shell node. These correspond with the top and bottom side of the shell element. From the temperature history ($NT11$) which is also presented in this figure the mechanism of stress formation can be derived.

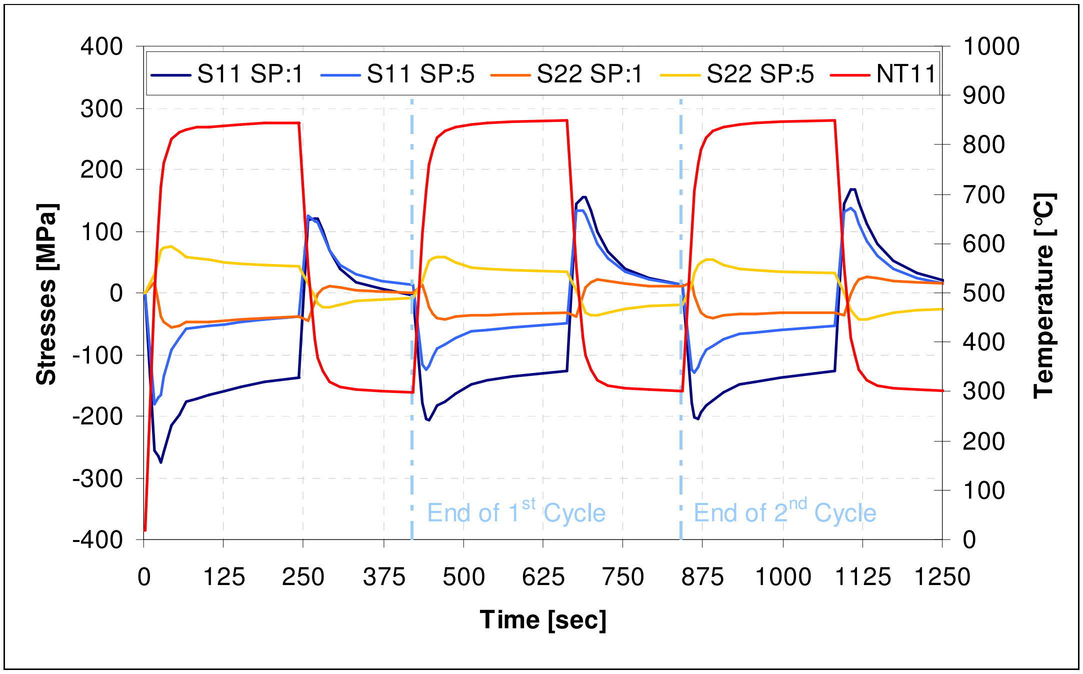

Figure 71: Stress and temperature history for point A on inner piping

The time history shows that with increasing temperature compressive stresses occur. As temperature decreases the compressive stress magnitude decreases and even changes sign and therefore become tensile. The opposite effect where tensile stresses occur at increasing temperature can be also observed at one integration point.

Another very important thing is that the highest stresses occur during the period of heating-up and cooling-down and not at the end of the respective phase. This means that the highest stresses are caused by transient temperature loading, which is also the experience from cast iron exhaust manifolds.

Figure 72 shows the principal stresses $S11$ and $S22$ over temperature. It again points out the previously explained correlation between compressive and tensile stresses and exhaust manifold temperature.

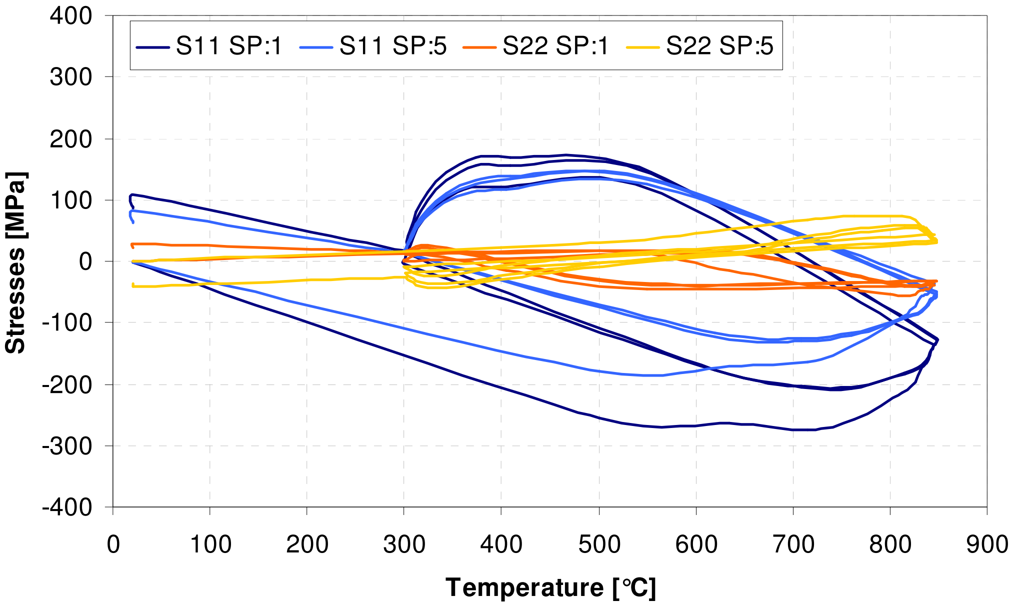

Figure 72: Stress vs. temperature for point A on inner piping

Figure 73 shows the principal stresses $S11$ and $S22$ over plastic strain. The hysteresis loops represent the three thermo-mechanical cycles calculated. Thereby a good stabilization of the stress/strain level after the third cycle can be observed.

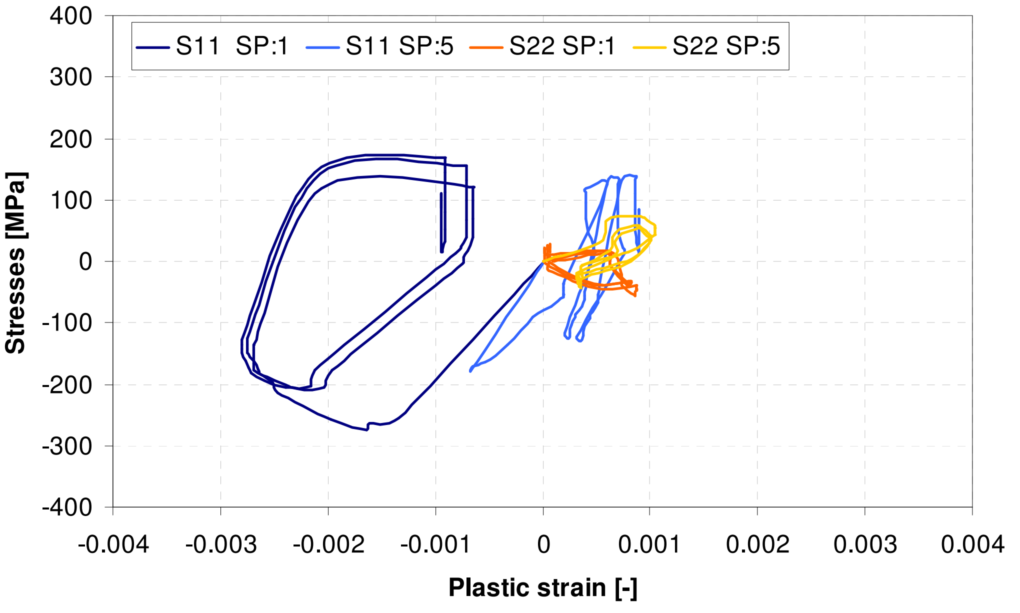

Figure 73: Stress vs. Plastic strain for point A on inner piping

Figure 74 shows the time history of the equivalent plastic strain. The increase of PEEQ can be observed over the thermal loading cycles whereby a gradual behavior can be seen. If the curve progression of PEEQ is compared to the temperature history it can be seen that the phases where the temperature of the parts increases strongly and high temperature gradients occur are responsible for the gradual increase whereas phases of small temperature changes have no significant influence on the PEEQ characteristics.

From Table 13 it can be seen that the highest accumulation of PEEQ happens during the first cycle. The increase of PEEQ over the second and third cycle is only slightly different which again shows the stabilized state of the analysis model.

As ΔPEEQ in cycles two and three differs by $0.02\ \%$ a fourth cycle would have to be calculated for obtaining absolute assurance about the state of stabilization as the criterion for customer projects at AVL is that ΔPEEQ has to be equal over two cycles. However, for the present work the results presented have sufficient significance and the calculation of a fourth cycle is therefore not necessary.

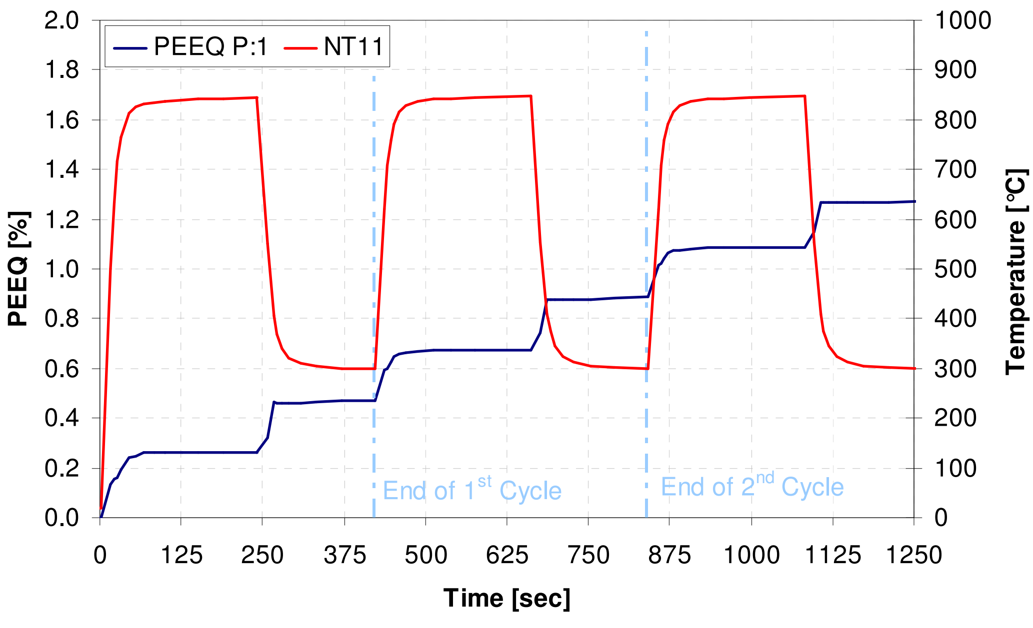

Figure 74: Equivalent plastic strain (PEEQ) for point A on inner piping

Table 13: Equivalent plastic strain increase during cycles at point A

	ΔPEEQ [$\%$]
During cycle 1	0.47
During cycle 2	0.41
During cycle 3	0.39

The total PEEQ after the third cycle is $1.27\ \%$ which is uncritical as already discussed in Chapter 4.2.3.

4.2.5 Detailed investigation on “shell-to-solid coupling” constraint definition

From the stress and plastic strain results discussed in Chapter 4.2.3 it can be assumed that the transition region where the shell elements are connected to the continuum elements by the ABAQUS/Standard “shell-to-solid coupling” constraint is not represented correctly in the global strength analysis. For the verification of this observation a submodel analysis of the transition region was performed. Thereby quadratic, tetrahedral elements of type C3D10M were used for all parts of the submodel.

From the comparison of the analysis result that is presented in Figure 75 with the global model on the left and the submodel on the right it can be learned that the suspicion about the malfunction of the “shell-to-solid coupling” proved itself to be true. In the constraint region the global model delivers discontinuities and values that can be regarded as physically impossible. However these effects can not be seen on the submodel results.

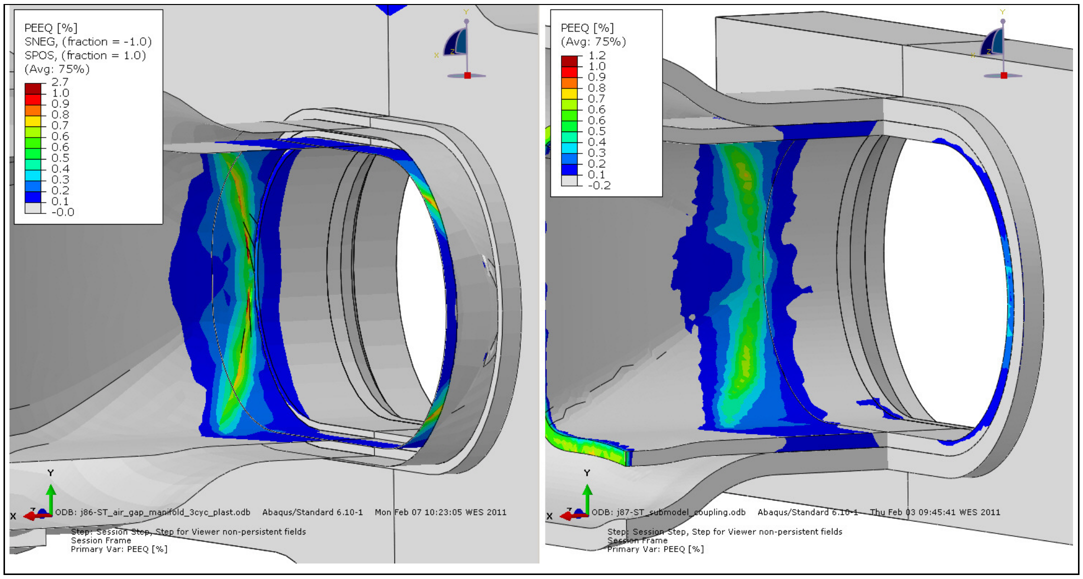

Figure 75: Comparison of global model (left) and submodel (right)

Summing up it can be said that the “shell-to-solid coupling” constraint in ABAQUS/Standard may represent the connection between shell and continuum elements sufficiently but it does not deliver physically correct results, hence it should not be used in regions where a detailed evaluation of a problem is necessary and critical results are expected. In order to save analysis time either the usage of this constraint has to be avoided or it has to be applied in a region that can be regarded as uncritical. If none of these is possible a submodel analysis of the respective region has to be necessarily performed.

4.3 Conclusions about strength analysis

From the strength analysis results the following observations were made.

The realistic modeling of weld joints has significant importance for the overall behavior of the analysis mode. Therefore it is important to use the recommended modeling techniques. This is necessary also for further evaluation of weld joints.

Furthermore it can be said that the usage of sliding fits is inevitable in air gap insulated exhaust manifolds as they enable relative movement between the inner pipes and therefore contribute significantly to the prevention of thermal stresses. This results in almost stress-free pipes, which allows the usage of minimal wall thicknesses.

As the exhaust manifold flange and the outer piping are functionally constructed similarly as cast iron manifolds their deformation behavior is also comparable.

The similarities between air gap insulated and cast iron exhaust manifolds were depicted also by the exemplary evaluation of a high loaded area.

With the means of submodel analysis the physical incorrectness of stresses and plastic strains in the region of “shell-to-solid coupling” constraints was verified. Therefore a submodel analysis is obligatory for critical areas to obtain proper results.

Due to the lack of advanced material models no damage evaluation of the exhaust manifold was performed.

5 Design criterions

During the development of the simulation method some influencing factors have been identified as particularly important in terms of their impact on the endurance of air gap insulated exhaust manifolds. The following chapter highlights these influencing factors. Furthermore approximate limits are named for the construction of dual-walled exhaust manifolds.

5.1 Temperature

The maximum exhaust gas temperature is one of the determining factors for the selection of the materials used. As exhaust gas temperatures up to $1000\,°C$ can be observed in modern Otto engines the choice of materials for the inner gas guiding pipes is limited as the material has to be stable even under this high temperature load.

Generally the temperature level of the outer skin is lower than the one of the inner piping so materials with lower temperature tolerance can be used. Nevertheless the occurrence of hot-spots has to be considered as they are responsible for the peak loading of the outer piping. Hot-spots are usually a result of constructional faults, hence special focus should be kept on this issue during the development process.

A recommendation for material usage in air gap insulated exhaust manifold projects is presented in Table 14.

Table 14: Recommended materials for air gap insulated exhaust manifolds

Mat. Nr.	Common name	Iron phase	Stable up to [$°C$]
Inner piping			
1.4828	X15CrNiSI20-12	Austenitic	1000
1.4841	X15CrNiSi25-21	Austenitic	1000
Outer piping			
1.4301	X5CrNi18-10	Austenitic	600
1.4509	X2CrTiNb18	Ferritic	950
1.4512	X2CrTi12	Ferritic	800

5.2 Deformation

As shown in Chapter 4.2.1 the deformation of the inner gas guiding pipes is very high because of the high temperature load. Since the deformation is heterogeneous for all parts due to temperature differences in the system relative movement occurs between the pipes. To avoid the creation of thermal stresses sliding fits have to be used to enable relative movement between the inner pipes. Thereby it is important to provide sufficient space for the relative movement of the parts. A first assumption for the elongation and the required cross-section can be made with

$$\Delta L = L_0\, \alpha\, T_{\max} \qquad (5.1)$$

where α is the linear thermal expansion coefficient [$1/K$] and $T_{\max}$ [$°C$] is the expected maximum wall temperature.

5.3 Strain

In the introduction the relevance of the thermal expansion property of the material was discussed, see Chapter 1.1.4. As the thermal expansion of ferritic materials is lower than the austenitic ones the usage of the first mentioned is recommended.

As can be seen from Hook’s law

$$\sigma = E\varepsilon \tag{5.2}$$

where

$$\varepsilon = \frac{\Delta L}{L} \tag{5.3}$$

stresses depend on the Young’s modulus E and the strain ε which again depends on the elongation of the part under thermal loading as can be seen from equation (5.1). Therefore it can be said that (thermal) stresses depend on the thermal expansion property of the material. In order to minimize the outer skirts overall stress level the usage of ferritic steel is recommended.

Note that the deformation and stress level of exhaust manifolds is mainly driven by the deformation behavior of the adjacent cylinder head which again is influenced by the properties of the material used and the predominant temperatures. As the cylinder head is water-cooled its temperature level is considerably lower than that of the exhaust manifold. Due to the bolt connection between the exhaust manifold and the cylinder head the global deformation of the cylinder head is transferred to the exhaust manifold. This phenomenon in comparison with the temperature inhomogeneity of the two parts can be regarded as the main influencing factor for exhaust manifold stresses and therefore has to be considered in the design process.

6 Summary

A finite element simulation methodology for dual-walled air gap insulated exhaust manifolds was developed with the aim to understand and predict physical phenomena within the air gap. As air gap insulated exhaust manifolds play a vital role for the reduction of engine cold start emissions the methodology itself can be understood as a contribution to the reduction of air pollutants in general.

Chapter 3 deals with the prediction of heat transfer phenomena within the air gap, where the influence of heat transfer mechanisms such as conduction, convection and radiation was analyzed. Finite element simulations were performed to understand the functionalities for modeling radiation heat transfer provided by ABAQUS/Standard. Based on the CAD geometry of an air gap insulated exhaust manifold three finite element heat transfer models differing only in the radiation method used were compared with each other in order to determine the one for the usage in further customer projects. The comparison was performed in terms of physical correctness, accuracy and computational costs. The result of this process was a recommendation for the usage of the surface normal radiation method to represent radiation heat transfer within the air gap as its accuracy in comparison to the physically exact fully implicit radiation method was sufficient and wall temperatures are only locally different. The overall comparability of the models is given due to the equality of their energy balances.

A simplified transient heat transfer analysis based on AVL methodology was performed in order to determine time dependent thermal effects. Thereby a special focus was set on the characteristic time dependent behavior of the dual-walled exhaust manifold as the effects of air gap insulation have a significant impact on heat transfer between the inner and outer piping.

Based on the transient heat transfer analysis a time dependent strength analysis methodology was presented in Chapter 4. The modeling approach was based on AVL standard procedures as the aim of the analysis was not to create a new strength analysis methodology but to inquire into the characteristic behavior of an air gap insulated exhaust manifold under thermo-mechanical loading. Thereby a special focus was set on the global deformation, stresses and plasticity effects. It was proven that due to constructional arrangements the inner pipes are in large part free of stresses as the outer skirt holds the carrying function. For a better understanding of stress and plastic strain formation an exemplary evaluation of a high loaded area was presented.

In order to represent the weld joints that are commonly used for the assembly of air gap insulated exhaust manifolds a modeling approach was presented for both shell and continuum element based weld joints. The evaluation of these joints demands further research and was recommended for further research topics.

As the strength analysis was performed with a model containing both shell and continuum elements the usage of the “shell-to-solid coupling” constraint was inevitable and demanded special attention. With the means of submodeling it was shown that the functionality of the coupling in terms of limiting degrees of freedom of shell elements itself was given but the results delivered were not physically correct.

Chapter 5 is concerned with design criterions in order to set boundaries and standards for the design process of further projects. The suggestions are dealing with material selection and constructional arrangements in order to avoid high stress levels.

6.1 Comparison with state of the technology

In comparison to the simulation methodology by Kyu-Hyun et al. [2000] which is based on an analytic approach, see Chapter 1.4 the present thesis chooses a numerical process.

An analytic two dimensional heat transfer analysis may deliver appropriate results for simple geometries but shows significant deviations in accuracy for complex parts such as an air gap insulated exhaust manifold that can not be compared to an idealized view that is assumed as two long concentric cylinders with an annular gap in between.

The numerical solution of a finite element problem in contrast allows the investigation of three dimensional heat transfer phenomena for highly complex geometries.

With the presented methodology physically correct results can be achieved within a short period of time even for complex part shapes. The modeling effort thereby may be higher than the one required for an analytic solution but the accuracy and physical correctness are superior. Furthermore the compatibility and handling of the results is easier as a temporal resolution of temperatures is available for every node of the finite element model, hence data can be directly used in further process steps such as strength and fatigue analysis.

Overall it can be said that an analytic approach may be sufficient for first interpretations of a problem and may deliver fair results for the constructional basic layout of an air gap insulated exhaust manifold but for durability and fatigue issues on the other hand such an approach has not enough significance. The state of the art component development process in automobile industry requires a methodology that delivers highly accurate results and enables reliable lifetime prediction. These can be achieved with the presented three dimensional finite element analysis methodology.

6.2 Outlook

During the methodology development process some topics arose that could not be covered within this thesis. As they could improve the accuracy of the presented methodology further investigations should be carried out dealing with the following topics.

6.2.1 Radiation heat transfer to ambient and underhood flow

As the mechanism of radiation heat transfer plays a vital role in the energy transfer between engine components the influence of the energy exchange between the hot outer skin of the exhaust manifold and the neighboring motor components should be further investigated. The same applies for the convective heat transfer due to underhood flow.

The aim of these inquiries should be to improve heat transfer analysis accuracy by adjusting the boundary conditions on the exhaust manifolds outer skin.

6.2.2 Advanced surface normal radiation modeling

In the presented methodology radiation heat transfer is assumed to happen only in normal direction to the respective facet. This approach was proven to be sufficiently accurate.

In order to improve the accuracy of the method the influence of the mechanism of radiation heat transfer should be investigated in more detail. Further investigations should deal with the energy exchange assuming that it happens not only in normal direction to the facet over a single straight line but rather over multiple diffuse rays in a certain differentiated neighboring region around the respective facet.

6.2.3 Validation of weld joints

As weld joints are indispensable for the assembly of dual-walled exhaust manifolds their validation is highly important. Further investigations should focus on modeling and validation of weld joints in order to develop an accurate finite element simulation methodology and therefore enable good durability and reliable lifetime prediction.

6.2.4 Noise, vibration, harshness (NVH) investigation

The abbreviation NVH is typically used to refer to the study of acoustic and mechanical oscillations in vehicles and their subjective perception by humans

[B. Heißing, M. Ersoy 2011, p. 421]. As dual-walled exhaust manifolds are exposed to permanently shifting pressure loads they show a high potential in terms of noise emission that can be perceived as disturbing by the passengers. This potential is even enforced as sheet metal which is used for dual-walled exhaust manifolds has low damping abilities. To achieve optimal comfort for the passengers the NVH behavior of air gap insulated exhaust manifolds should be investigated in detail. A finite element modal analysis is an effective way to identify weak points of the construction and can be used effectively to improve the NVH performance of exhaust manifolds.

Bibliography

AVL List GmbH. *DAC skill team*. Graz, 2010.

AVL List GmbH. *iCAE*. Graz, 2010.

AVL List GmbH. *Material database*. Graz, 2010.

H.D. Baehr, K. Stephan. *Wärme- und Stoffübertragung*. Springer-Verlag, Berlin/Heidelberg, 2008.

R. van Basshuysen, F. Schäfer (ed). *Handbuch Verbrennungsmotor*. Vieweg, Braunschweig/Wiesbaden, 2nd edition, 2002.

M.W. Bekkering, G.L. Wells. 1998. “Exhaust air rail manifold.” US Patent, US 5,768,890.

P. Bonny, T. Hülsberg, T. Sternal. 1996. “Abgaskrümmer für eine Brennkraftmaschine sowie Verfahren zur Herstellung desselben.” Germany, DE 19628797 C1.

Y.A. Çengel. *Heat Transfer: a practical approach*. McGraw-Hill, New York, NY, USA, 2nd edition, 2003.

R. Diez. 2005. “Luftspaltkrümmer.” Germany, DE 10346552 A1.

R. Diez, R. Sahan, M. Ramusch. 2008. “Abgaskrümmer.” Germany, DE 202006015883 U1.

B. Heißing, M. Ersoy. *Chassis Handbook*. Vieweg+Teubner Verlag, Wiesbaden, 1st edition, 2011.

D. Hiemesch, D. Niederhauser. 2002. “Abgaskrümmer zur Abgasführung aus einem Verbrennungsmotor.” Germany, DE 10102637 A1.

J.P. Holman. *Heat Transfer*. McGraw-Hill, New York, NY, USA, 1990.

J.P. Holman. *Heat Transfer*. McGraw-Hill, New York, NY, USA, 2010.

F.P. Incropera, D.P. DeWitt. *Fundamentals of Heat and Mass Transfer*. John Wiley & Sons, Hoboken, NJ, 2002.

E. Jean. “Exhaust system thermal management for Diesel passenger car EURO 5 applications.” In *Proc. of Diesel Engine 2006*. Société des Ingénieurs de l'Automobile, Lyon, 2006.

O. Kovar, T. Nording. 2001. “Air gap insulated exhaust manifold.” US Patent, US 6,247,552 B1.

L. Kyu-Hyun, S. Chang-Yeul, K. Wan-Bum. “Development of Dual Wall Air Gap Exhaust System.” Presented at SAE world congress, 2000-01-0205, 2000.

R.K. MacGregor, A.P. Emery. “Free Convection through Vertical Plane Layers: Moderate and High Prandtl Number Fluids.” *Journal of Heat Transfer*, **92**, pp. 391, 1969.

R.M. Naubert, J. Nutz. 2000. “Luftspaltisolierter Schalenkrümmer.” Germany, DE 19952648 A1.

T. Nording. „Neuartiges Konzept für isolierte Abgaskrümmer, Vorrohre und Katalysatoren.“ *MTZ*, **1991**(4), p. 206-210.

T. Nording, T. Beck. 2005. “Luftspaltisolierter Abgaskrümmer.” Germany, DE 102004021196 A1.

T. Nording, F. Müller, M. Bott. “Air gap Insulated Exhaust Manifold for a Six-cylinder Turbocharged Engine.” *MTZ Worldwide*, **2009**(12), p. 20-24.

H. Petutschnig, P. Klinner, A. Kobor, E. Schutting. „Numerical Computation of the Temperature Field.” *MTZ Worldwide*, **2002**(12), p. 6-8; 20.

G.D. Raithby, K.G.T. Hollands. “A General Method of Obtaining Approximate Solutions to Laminar and Turbulent Free Convection Problems.” In Advances in Heat Transfer, **11**, p. 265-315, Academic Press, New York, 1975.

W.M. Rohsenow, P.J. Hartnett. *Handbook of Heat Transfer*. McGraw-Hill, New York, NY, USA, 1973.

C. Santanam, D. Priebe, T. Scofield, K. Grable. “Design of a Dual Wall Air Gap Exhaust Manifold.” Presented at SAE world congress, 980045, 1998.

G. Schmelzer. 2009. “Air gap insulated exhaust manifold.“ US Patent, US 2009/0139220 A1.

R. Siegel, J.R. Howell. *Thermal Radiation Heat Transfer*. McGraw-Hill, New York, NY, USA, 1980.

Simulia Inc. *ABAQUS/Standard Manual*. Providence, RI, USA, v6.10 edition, 2010.

VDI. *VDI-Wärmeatlas*. Springer-Verlag, Berlin and Heidelberg, 10th edition, 2002.

G. Wirth, M. Bott, F. Müller. 2009. “Luftspaltisolierter Abgaskrümmer.” Germany, DE 102008019999 A1.

Appendix A

Table A.1: Thermophysical properties of air at atmospheric pressure [Incropera and DeWitt 2002, p. 917]

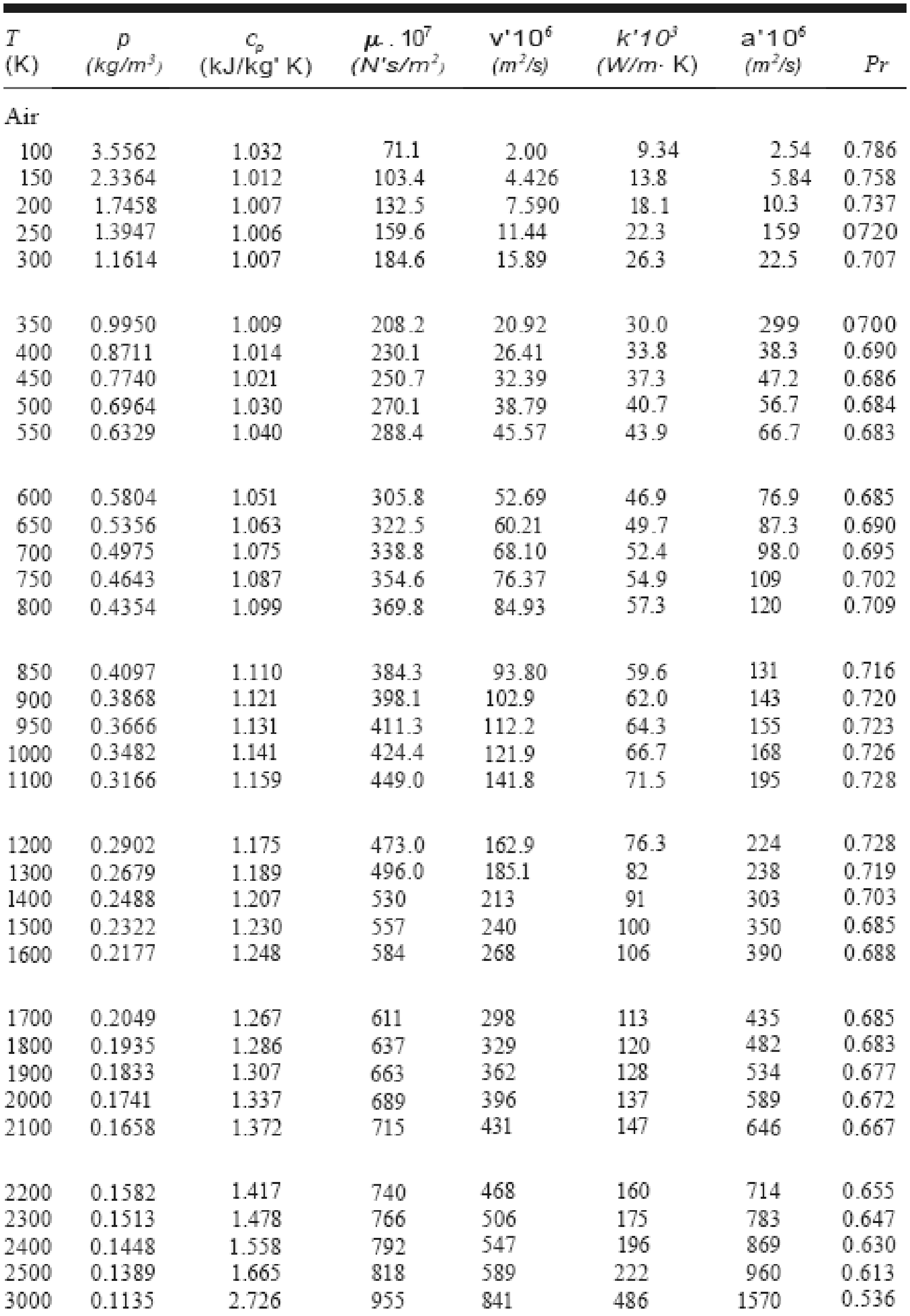

T (K)	p (kg/m^3)	c_p (kJ/kg' K)	μ . 10^7 (N's/m^2)	v'10^6 (m^2/s)	k'10^3 (W/m· K)	a'10^6 (m^2/s)	Pr
Air							
100	3.5562	1.032	71.1	2.00	9.34	2.54	0.786
150	2.3364	1.012	103.4	4.426	13.8	5.84	0.758
200	1.7458	1.007	132.5	7.590	18.1	10.3	0.737
250	1.3947	1.006	159.6	11.44	22.3	159	0720
300	1.1614	1.007	184.6	15.89	26.3	22.5	0.707
350	0.9950	1.009	208.2	20.92	30.0	299	0700
400	0.8711	1.014	230.1	26.41	33.8	38.3	0.690
450	0.7740	1.021	250.7	32.39	37.3	47.2	0.686
500	0.6964	1.030	270.1	38.79	40.7	56.7	0.684
550	0.6329	1.040	288.4	45.57	43.9	66.7	0.683
600	0.5804	1.051	305.8	52.69	46.9	76.9	0.685
650	0.5356	1.063	322.5	60.21	49.7	87.3	0.690
700	0.4975	1.075	338.8	68.10	52.4	98.0	0.695
750	0.4643	1.087	354.6	76.37	54.9	109	0.702
800	0.4354	1.099	369.8	84.93	57.3	120	0.709
850	0.4097	1.110	384.3	93.80	59.6	131	0.716
900	0.3868	1.121	398.1	102.9	62.0	143	0.720
950	0.3666	1.131	411.3	112.2	64.3	155	0.723
1000	0.3482	1.141	424.4	121.9	66.7	168	0.726
1100	0.3166	1.159	449.0	141.8	71.5	195	0.728
1200	0.2902	1.175	473.0	162.9	76.3	224	0.728
1300	0.2679	1.189	496.0	185.1	82	238	0.719
1400	0.2488	1.207	530	213	91	303	0.703
1500	0.2322	1.230	557	240	100	350	0.685
1600	0.2177	1.248	584	268	106	390	0.688
1700	0.2049	1.267	611	298	113	435	0.685
1800	0.1935	1.286	637	329	120	482	0.683
1900	0.1833	1.307	663	362	128	534	0.677
2000	0.1741	1.337	689	396	137	589	0.672
2100	0.1658	1.372	715	431	147	646	0.667
2200	0.1582	1.417	740	468	160	714	0.655
2300	0.1513	1.478	766	506	175	783	0.647
2400	0.1448	1.558	792	547	196	869	0.630
2500	0.1389	1.665	818	589	222	960	0.613
3000	0.1135	2.726	955	841	486	1570	0.536

Table A.2: Thermophysical properties of air at atmospheric pressure [Baehr and Stephan 2008, p. 723]

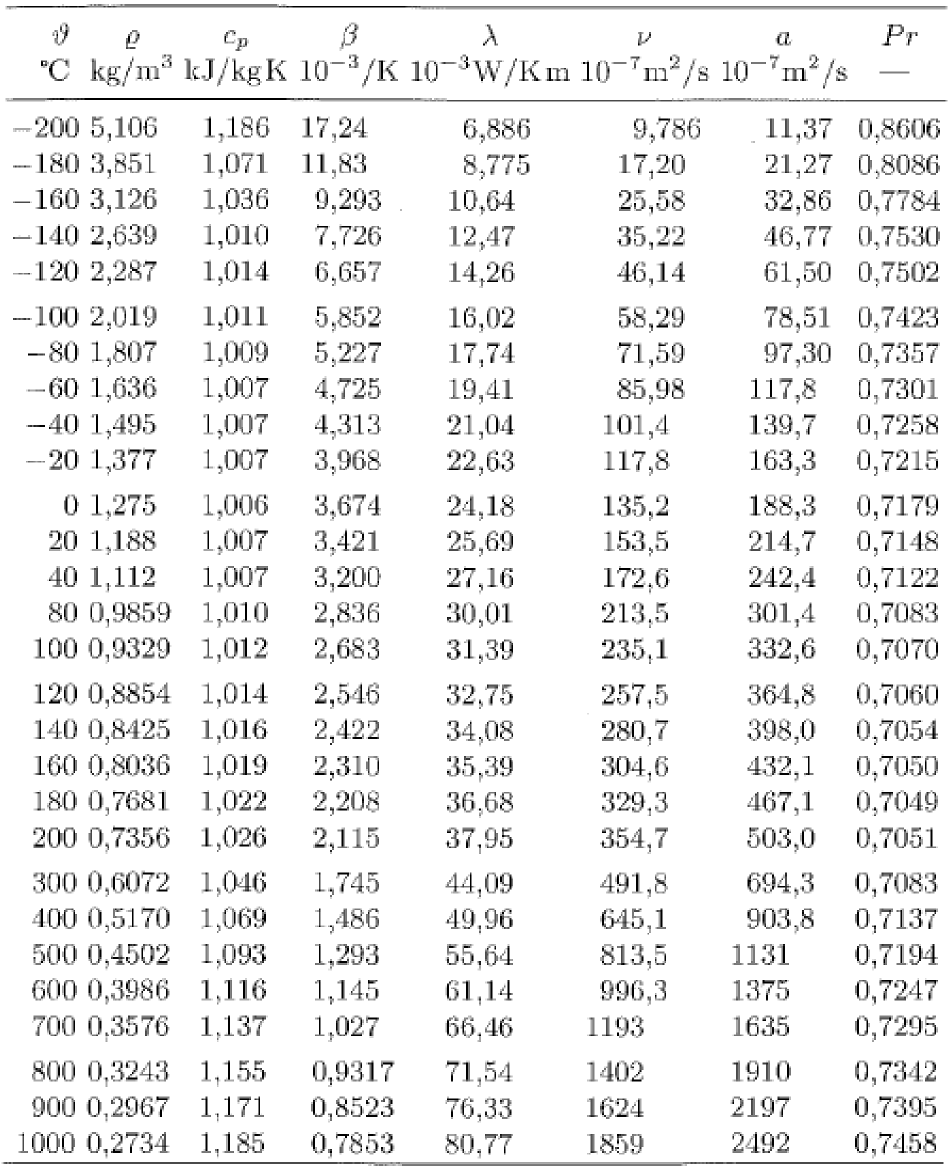

ϑ °C	ϱ kg/m^3	c_p kJ/kgK	β 10^{-3}/K	λ 10^{-3}W/Km	ν 10^{-7}m^2/s	a 10^{-7}m^2/s	Pr —
−200	5,106	1,186	17,24	6,886	9,786	11,37	0,8606
−180	3,851	1,071	11,83	8,775	17,20	21,27	0,8086
−160	3,126	1,036	9,293	10,64	25,58	32,86	0,7784
−140	2,639	1,010	7,726	12,47	35,22	46,77	0,7530
−120	2,287	1,014	6,657	14,26	46,14	61,50	0,7502
−100	2,019	1,011	5,852	16,02	58,29	78,51	0,7423
−80	1,807	1,009	5,227	17,74	71,59	97,30	0,7357
−60	1,636	1,007	4,725	19,41	85,98	117,8	0,7301
−40	1,495	1,007	4,313	21,04	101,4	139,7	0,7258
−20	1,377	1,007	3,968	22,63	117,8	163,3	0,7215
0	1,275	1,006	3,674	24,18	135,2	188,3	0,7179
20	1,188	1,007	3,421	25,69	153,5	214,7	0,7148
40	1,112	1,007	3,200	27,16	172,6	242,4	0,7122
80	0,9859	1,010	2,836	30,01	213,5	301,4	0,7083
100	0,9329	1,012	2,683	31,39	235,1	332,6	0,7070
120	0,8854	1,014	2,546	32,75	257,5	364,8	0,7060
140	0,8425	1,016	2,422	34,08	280,7	398,0	0,7054
160	0,8036	1,019	2,310	35,39	304,6	432,1	0,7050
180	0,7681	1,022	2,208	36,68	329,3	467,1	0,7049
200	0,7356	1,026	2,115	37,95	354,7	503,0	0,7051
300	0,6072	1,046	1,745	44,09	491,8	694,3	0,7083
400	0,5170	1,069	1,486	49,96	645,1	903,8	0,7137
500	0,4502	1,093	1,293	55,64	813,5	1131	0,7194
600	0,3986	1,116	1,145	61,14	996,3	1375	0,7247
700	0,3576	1,137	1,027	66,46	1193	1635	0,7295
800	0,3243	1,155	0,9317	71,54	1402	1910	0,7342
900	0,2967	1,171	0,8523	76,33	1624	2197	0,7395
1000	0,2734	1,185	0,7853	80,77	1859	2492	0,7458

Table A.3: Gap conductance properties $h_\delta\,[W/m\cdot K]$

Gap size [mm]	20 $°C$	100 $°C$	200 $°C$	300 $°C$	400 $°C$	500 $°C$	600 $°C$	700 $°C$	800 $°C$	900 $°C$	1000 $°C$
0	2.57E-05	3.14E-05	4.49E-05	4.41E-05	5.00E-05	5.56E-05	6.11E-05	6.65E-05	7.15E-05	7.63E-05	8.08E-05
5	5.14E-06	6.28E-06	8.98E-06	8.82E-06	9.99E-06	1.11E-05	1.22E-05	1.33E-05	1.43E-05	1.53E-05	1.62E-05
10	2.57E-06	3.14E-06	4.49E-06	4.41E-06	5.00E-06	5.56E-06	6.11E-06	6.65E-06	7.15E-06	7.63E-06	8.08E-06
15	1.71E-06	2.09E-06	2.99E-06	2.94E-06	3.33E-06	3.71E-06	4.08E-06	4.43E-06	4.77E-06	5.09E-06	5.38E-06
20	1.28E-06	1.57E-06	2.25E-06	2.20E-06	2.50E-06	2.78E-06	3.06E-06	3.32E-06	3.58E-06	3.82E-06	4.04E-06
25	1.03E-06	1.26E-06	1.80E-06	1.76E-06	2.00E-06	2.23E-06	2.45E-06	2.66E-06	2.86E-06	3.05E-06	3.23E-06
30	8.56E-07	1.05E-06	1.50E-06	1.47E-06	1.67E-06	1.85E-06	2.04E-06	2.22E-06	2.38E-06	2.54E-06	2.69E-06
35	7.34E-07	8.97E-07	1.28E-06	1.26E-06	1.43E-06	1.59E-06	1.75E-06	1.90E-06	2.04E-06	2.18E-06	2.31E-06
40	0.00E+00	0.00E+00	0.00E+00	0.00E+00	0.00E+00	0.00E+00	0.00E+00	0.00E+00	0.00E+00	0.00E+00	0.00E+00

Table A.4: Gap radiation properties for ABAQUS/Standard interaction definition

Emissivity of master surface	0.8
Emissivity of slave surface	0.8
Viewfactor [-]	Clearance [mm]
1	0
1	100
0	105

Statutory declaration

I declare that I have authored this thesis independently, that I have not used other than the declared sources / resources, and that I have explicitly marked all material which has been quoted either literally or by content from the used sources.

Date

Signature